Understanding the origin of $^{35/37}$Cl and $^{16/18}$O isotope effects on ^{195}Pt and ^{103}Rh NMR nuclear shielding in selected Pt(IV) and Rh(III) complexes. A DFT study

by
John Christopher Davis

Dissertation presented jointly for the degree of *Doctor of Philosophy in*

the Faculty of Science at
Stellenbosch University

and the University of St Andrews

Supervisor: Prof Klaus R. Koch
Co-supervisor: Prof Michael Bühl

December 2013

Declaration

By submitting this thesis/dissertation electronically, I declare that the entirety of the work contained therein is my own, original work, that I am the sole author thereof (save to the extent explicitly otherwise stated), that reproduction and publication thereof by Stellenbosch University will not infringe any third party rights and that I have not previously in its entirety or in part submitted it for obtaining any qualification.

Date: December 2013

Abstract

Distinctive fine-structure due to $^{35}Cl/^{37}Cl$ isotopologue and isotopomer effects is resolved at high magnetic fields for ^{195}Pt and ^{103}Rh NMR signals, resulting in a unique NMR "finger-print", with which it is possible to uniquely identify all chlorido containing Pt(IV) and Rh(III) complexes. In this study, these isotope shifts are computed from first principles in order to provide a solid theoretical framework for the empirical observations.

Use is made of DFT to calculate the $^{35/37}Cl$ and $^{16/18}O$ induced isotope shifts in the ^{195}Pt NMR spectra of $[Pt^{35}Cl_6]^{2-}$ and $[Pt^{37}Cl_6]^{2-}$, for the $[Pt^{35}Cl_n{}^{37}Cl_{5-n}(H_2O)]^{-}$ (n=0-5), *cis*-$Pt^{35}Cl_n{}^{37}Cl_{(4-n)}(H_2O)_2$ (n=0-4), and *fac*-$[Pt^{35}Cl_n{}^{37}Cl_{(3-n)}(H_2O)_3]^{+}$ (n=0-3) series. The computational protocol is extended to calculate the $^{35/37}Cl$ and $^{16/18}O$ induced isotope shifts in $[Pt^{35}Cl_n{}^{37}Cl_{5-n}(OH)]^{2-}$ (n=0-5), *cis*-$[Pt^{35}Cl_n{}^{37}Cl_{(4-n)}(OH)_2]^{2-}$ (n=0-4), *fac*-$[Pt^{35}Cl_n{}^{37}Cl_{(3-n)}(OH)_3]^{2-}$ (n=0-3), *cis*-$[Pt^{35}Cl_n{}^{37}Cl_{2-n}(OH)_4]^{2-}$ (n=0-2) and $[Pt^{35}Cl_n{}^{37}Cl_{1-n}(OH)_5]^{2-}$ (n=0-1). For Rh(III), the $^{35}Cl/^{37}Cl$ isotope shifts in the ^{103}Rh NMR spectra of $[Rh^{35}Cl_n{}^{37}Cl_{5-n}(H_2O)]^{2-}$ (n=0-5), *cis*-$[Rh^{35}Cl_n{}^{37}Cl_{(4-n)}(H_2O)_2]^{-}$ (n=0-4), and *fac*-$Rh^{35}Cl_n{}^{37}Cl_{(3-n)}(H_2O)_3$ (n=0-3) were calculated.

The ^{195}Pt and ^{103}Rh NMR chemical shifts computed for these species reproduce the order of magnitude of the observed effect reasonably well, up to *ca.* 1 ppm. In most cases, general trends are also captured qualitatively, thus providing the first theoretical basis for the origin of subtle isotope shifts in ^{195}Pt NMR spectra. Neither simple polarizable continuum models nor small, microsolvated complexes lead to improved isotope shifts for the series investigated, however, valuable insight into the degree of solvent interaction was gained. Using the polarized continuum model to calculate shielding/bond-length derivatives together with gas-phase zero-point corrections to estimate shieldings, it was shown that the contraction of the coordination sphere in the hydroxide complexes cause the Pt-Cl bonds to become magnetically equivalent, justifying why their isotopomers aren't resolved.
In this study, theoretical modeling of structural effects on NMR parameters extends to the smallest scale, distance changes of a few femtometers upon isotopic substitution.

Opsomming

Kenmerkende fyn struktuur as gevolg van $^{35}Cl/^{37}Cl$ isotopoloog en isotopomeer effekte word waargeneem onder hoë velde in ^{195}Pt en ^{103}Rh KMR-seine, wat lei tot 'n unieke KMR "vinger-afdruk", waarmee dit moontlik is om Pt(IV) en Rh(III) komplekse te kan identifiseer. In hierdie studie word isotoop verskuiwings bereken vanaf eerste beginsels met die doel om 'n soliede teoretiese raamwerk vir die empiriese waarnemings te bou.

Gebruik word gemaak van Elektrondigtheidsteorie om $^{35/37}Cl$ en $^{16/18}O$ geïnduseerde isotoop verskuiwngs in die ^{195}Pt KMR spektra van $[Pt^{35}Cl_6]^{2-}$ en $[Pt^{37}Cl_6]^{2-}$ te bereken, asook die $[Pt^{35}Cl_n{}^{37}Cl_{5-n}(H_2O)]^-$ (n = 0 - 5), *cis*-$Pt^{35}Cl_n{}^{37}Cl_{(4-n)}(H_2O)_2$ (n = 0-4) en die *fac*-$[Pt^{35}Cl_n{}^{37}Cl_{(3-n)}(H_2O)_3]^+$ (*n*=0-3) reeks. Die ontwikkelde berekeningsproses protokol word toegepas op die geïnduseerde $^{16/18}O$ en $^{35/37}Cl$ isotoop verskuiwings van $[Pt^{35}Cl_n{}^{37}Cl_{5-n}(OH)]^{2-}$ (*n*=0-5), *cis*-$[Pt^{35}Cl_n{}^{37}Cl_{(4-n)}(OH)_2]^{2-}$ (*n*=0-4), *fac*-$[Pt^{35}Cl_n{}^{37}Cl_{(3-n)}(OH)_3]^{2-}$ (*n*=0-3), *cis*-$[Pt^{35}Cl_n{}^{37}Cl_{2-n}(OH)_4]^{2-}$ (*n*=0-2) en $[Pt^{35}Cl_n{}^{37}Cl_{1-n}(OH)_5]^{2-}$ (*n*=0-1). Die $^{35}Cl/^{37}Cl$ isotoop verskuiwings van Rh(III) komplekse, $[Rh^{35}Cl_n{}^{37}Cl_{5-n}(H_2O)]^{2-}$ (*n*=0-5), *cis*-$[Rh^{35}Cl_n{}^{37}Cl_{(4-n)}(H_2O)_2]^-$ (*n*=0-4), en *fac*-$Rh^{35}Cl_n{}^{37}Cl_{(3-n)}(H_2O)_3$ (*n*=0-3) is ook bereken.

Die berekende ^{195}Pt en ^{103}Rh KMR chemiese verskuiwings vir hierdie spesies, weerspieël die ordegrootte van die eksperimentele effek redelik goed, tot ongeveer 1 dpm. In die meeste gevalle, word algemene tendense kwalitatief weerspeel, dit verskaf dus die eerste teoretiese basis vir die oorsprong van die subtiele isotoop verskuiwings in ^{195}Pt KMR-spektra. Wedersyds die in agneming van “mikro-opgelosde” komplekse, óf ‘n eenvoudige gepolariseerde kontinuum model, lei tot ‘n verbetering in die akkuraatheid van die berekende isotoop verskuiwings vir die reeks komplekse wat ondersoek is, maar waardevolle insig tot oplossings-interaksies is verkry. Deur gebruik te maak van ‘n gepolariseerde kontinuum model is verskuiwing/bindingslengtes afgeleides bepaal, en saam met gas-fase nul-punt korreksies gebruik om isotoop verksuiwings te skat. Dit bewys dat die sametrekking van die koördinerings-sfeer in die hidroksied komplekse veroorsaak dat die Pt-Cl bindings magneties ekwivalente word, en dit verklaar tot ‘n mate waarom moontlike isotopomere nie onderskei kan word nie. In hierdie studie, word teoretiese modelle van strukturele effekte op KMR verskuiwings gestrek tot op die kleinste skaal: afstand verandering van 'n paar femtometers op isotopiese substitusie is belangrik.

Publications and conference contributions resulting from this thesis

$^{35/37}$Cl and $^{18/16}$O Isotope Effects on ^{195}Pt and ^{103}Rh NMR Chemical Shifts. A Density Functional Study.
J. C. Davis, M. Bühl, K. R. Koch, *manuscript in preparation.*

On the Origin of $^{35/37}$Cl Isotope Effects on ^{195}Pt NMR Chemical Shifts. A Density Functional Study.
J. C. Davis, M. Bühl, K. R. Koch, *J. Chem. Theor. Comput.* **2012**, *8*, 1344-1350.

Understanding subtle isotope effects on ^{195}Pt NMR chemical shifts. A DFT study.
J. C. Davis, M. Bühl, K. R. Koch (2012, May), Oral presentation at the Royal Society of Chemistry Theoretical Group Conference, London, UK.

What is the Origin of Isotope Effects on ^{195}Pt Chemical Shifts?
J. C. Davis, M. Bühl, K. R. Koch (2011, June), Poster presentation at the Royal Society of Chemistry Theoretical Group Conference, Nottingham, UK.

Probing isotope shifts in ^{195}Pt NMR spectra with DFT.
J. C. Davis, M. Bühl, K. R. Koch (2012, June), Poster presentation at the ScotChem 2012 Conference, Glasgow, UK.

Acknowledgements

This thesis has become possible due to the generous and ongoing support of many people; it is impossible to name all of you here.

I would like to thank my supervisors, Professors Klaus Koch and Michael Bühl, for their support, guidance and passion concerning this project.
I wish to thank Dr. H. Früchtl for technical support and maintaining the local Opteron PC cluster at the EaStChem Research Computing facility in St Andrews.

I wish to thank my fiancée, Zoé. We shared all the ups and downs of life during our PhD studies and you definitely had the harder part of it.

I should like to express my gratitude to the members of the PGM research group: Shani, Theo, Hugo, James, Eugene; especially Dr. Willem J. Gerber for his invaluable guidance during the early years. I wish to thank my lab co-workers in room 208 and 150 of the Purdie Building: Ragnar, Nicolas, Luke, James, Jie, Neetika, Rosie, Leo and Lazaros for the many pleasant trips to the pub.

This is the place to mention my parents Maureen and John for their encouragement and support. Some family members who played a vital role throughout this journey include; Carol, Donovan, Cole and Adam; Keith, Rochelle, Robyn and Kayrian; Craig, René, Christopher and Caitlin. I would also like to thank the Lloyd's: Michael, Mary, Rowan and Robin for their kind support.

I gratefully acknowledge financial support from Stellenbosch University in terms of an exchange agreement between St. Andrews and Stellenbosch University as well as Angloplatinum Ltd.

To Zoé & Ben

Table of Contents

List of Figures

List of Tables

Table A.2: Vibrationally averaged bond-lengths at 0K for the $^{35/37}$Cl isotopologues and isotopomers of $[PtCl_5(H_2{}^{18}O)]^-$.

Table A.3: Vibrationally averaged bond-lengths at 0K for the $^{35/37}$Cl isotopologues and isotopomers of *cis*-$PtCl_4(H_2{}^{16}O)_2$

Table A.4: Vibrationally averaged bond-lengths at 0K for the $^{35/37}$Cl isotopologues and isotopomers of *cis*-$PtCl_4(H_2{}^{18}O)_2$.

Table A.5: Vibrationally averaged bond-lengths at 0K for the $^{35/37}$Cl isotopologues and isotopomers of *cis*-$PtCl_4(H_2{}^{18}O)$ $(H_2{}^{16}O)$.

Table A.6: Vibrationally averaged bond-lengths at 0K for the $^{35/37}$Cl isotopologues[b] and isotopomers of *fac*-$[PtCl_3(H_2{}^{16}O)_3]^+$ and *fac*-$[PtCl_3(H_2{}^{16}O)_2(H_2{}^{18}O)]^+$.

Table A.7: Vibrationally averaged bond-lengths at 0K for the $^{35/37}$Cl isotopologues of *fac*-$[PtCl_3(H_2{}^{18}O)_2(H_2{}^{16}O)]^+$.

Table A.8: Vibrationally averaged bond-lengths at 0K for the $^{35/37}$Cl isotopologues of *fac*-$[PtCl_3(H_2{}^{18}O)_3]^+$.

Table A.9: Vibrationally averaged bond-lengths at 0K for the $^{35/37}$Cl isotopologues and isotopomers of $[PtCl_5(^{16}OH)]^{2-}$.

Table A.10: Vibrationally averaged bond-lengths at 0K for the $^{35/37}$Cl isotopologues and isotopomers of $[PtCl_5(^{18}OH)]^{2-}$.

Table A.11: Vibrationally averaged bond-lengths at 0K for the $^{35/37}$Cl isotopologues and isotopomers of *cis*-$[PtCl_4(^{16}OH)_2]^{2-}$.

Table A.12: Vibrationally averaged bond-lengths at 0K for the $^{35/37}$Cl isotopologues and isotopomers of *cis*-$[PtCl_4(^{18}OH)_2]^{2-}$.

Table A.13: Vibrationally averaged bond-lengths at 0K for the $^{35/37}$Cl isotopologues[b] and isotopomers of *fac*-$[PtCl_3(^{16}OH)_3]^{2-}$ and *fac*-$[PtCl_3(^{18}OH)_3]^{2-}$.

Table A.14: Vibrationally averaged bond-lengths at 0K for the $^{35/37}$Cl isotopologues[b] and isotopomers of *cis*-$[PtCl_2(^{16}OH)_4]^{2-}$ and *cis*-$[PtCl_2(^{18}OH)_4]^{2-}$.

Table A.15: Vibrationally averaged bond-lengths at 0K for the $^{35/37}$Cl isotopologues[b] and isotopomers of $[PtCl(^{16}OH)_5]^{2-}$ and $[PtCl(^{18}OH)_5]^{2-}$.

Table A.16: Vibrationally averaged bond-lengths at 0K for the $^{35/37}$Cl isotopologues and isotopomers of $[RhCl_5(H_2{}^{16}O)]^{2-}$.

Table A.17: Vibrationally averaged bond-lengths at 0K for the $^{35/37}$Cl isotopologues and isotopomers of *cis*-$[RhCl_4(H_2{}^{16}O)_2]^{-}$.

Table A.18: Vibrationally averaged bond-lengths at 0K for the $^{35/37}$Cl isotopologues and isotopomers of *fac*-$[RhCl_3(H_2{}^{16}O)_3]^{2-}$

List of Abbreviations

NMR	Nuclear Magnetic Resonance
DFT	Density Functional Theory
ZORA	Zeroth-Order Regular Approximation
ECP	Effective Core Potential
MD	Molecular Dynamics
LR-ESC	Linear Response Elimination Of Small Component
RPA	Random Phase Approximation
SO	Spin-Orbit
BOA	Born-Oppenheimer Approximation
PES	Potential Energy Surface
WFT	Wavefunction Theory
LDA	Local Density Approximation
GGA	Generalized Gradient Approximation
HF	Hartree-Fock
STO	Slater-Type Orbital
GTO	Gaussian-Type Orbital
QED	Quantum Electrodynamics
MC	Monte Carlo
SCF	Self-Consistent Field
GIAO	Gauge-Including Atomic Orbitals
CPKS	Coupled Perturbed Kohn-Sham
PCM	Polarized Continuum Model
COSMO	Conductor –Like Screening Model

All symbols and other abbreviations have their usual meaning.

If I have seen further, it is by standing on the shoulders of giants.

— Sir Isaac Newton

Chapter 1

Introduction

1.1 ^{195}Pt NMR Spectroscopy

High-resolution ^{195}Pt NMR spectroscopy has proven to be an indispensable spectroscopic tool for the structure elucidation and characterization of numerous platinum containing compounds in the last four decades, the topic having been extensively reviewed.[1] The ^{195}Pt nucleus has been shown to be a useful NMR probe, with a range of values for chemical shifts that span 13 000 ppm and a change of 100 ppm or more is observed when varying ligand substituents[1c] as shown in Fig. 1.1.

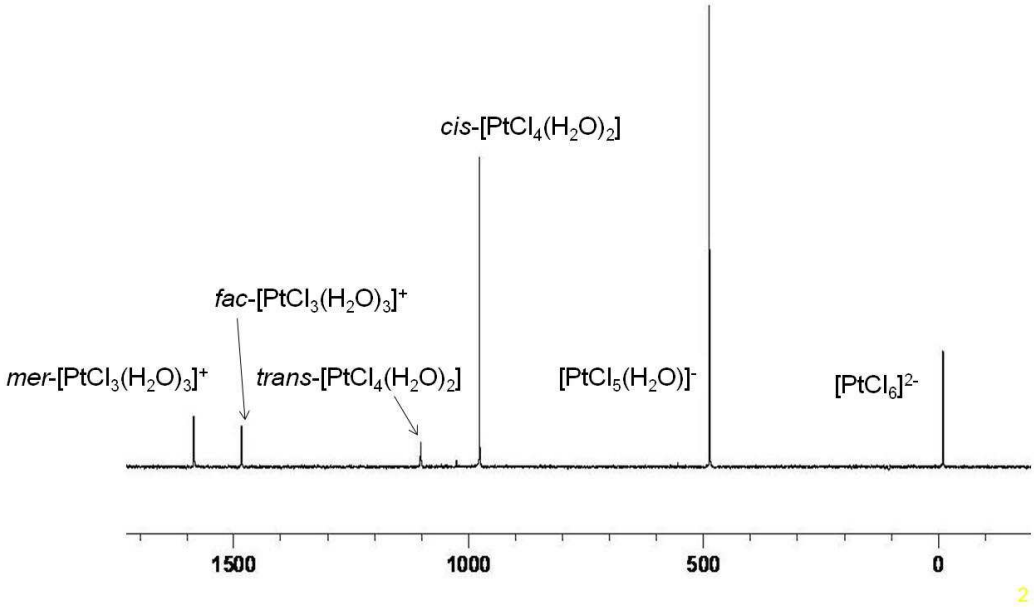

Figure 1.1: ^{195}Pt NMR spectrum showing Pt(IV) aquo/chloride species present in sample prepared from by oxidizing $[PtCl_4]^{2-}$ in $HClO_4$ with $NaClO_3$.[2]

In a magnetic field, any system with a net (electronic or nuclear) spin magnetic moment will experience a splitting of its energy levels. This splitting is associated with the different possible orientations of the spin. It is called the nuclear or electronic Zeeman effect.[3] The magnitude of the splitting is directly proportional to the applied magnetic field. In a molecule, the externally applied field will induce

currents within the electronic system. Such currents result in induced magnetic fields that modify the external field at the position of the spin magnetic moment. The resulting change of the local field (as the near degeneracy of energy levels is lifted) is the focus of nuclear magnetic resonance (NMR). The ^{195}Pt nucleus is affected by factors such as platinum complex concentration, changes in bond-lengths[4] (as shown in Fig. 1.2), ion-pairing effects[5], temperature and the composition of the solvent.[1c]

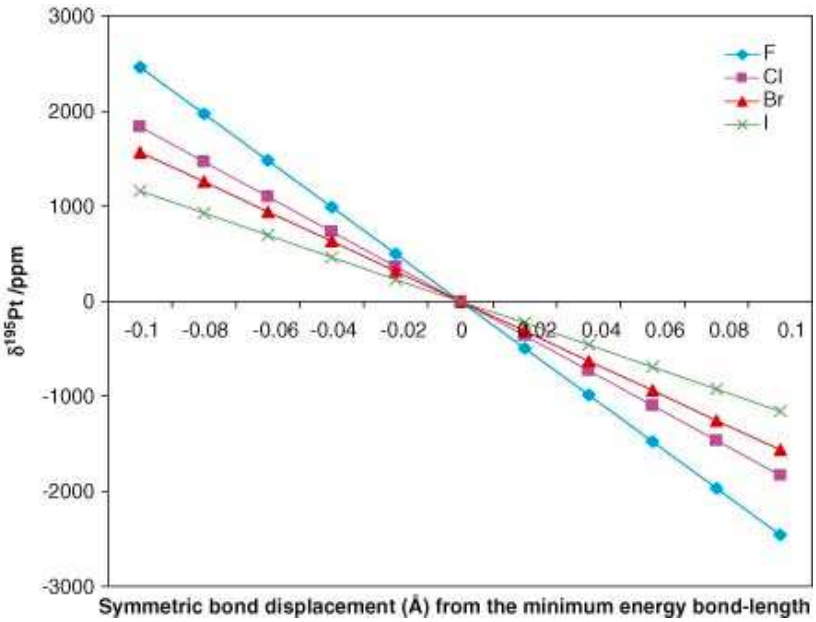

Figure 1.2: Summary of the sensitivity $\partial(\delta^{195}\text{Pt})/\partial(\Delta\text{Pt—X})$ of the total shielding tensor of the platinum nucleus for the $[PtX_6]^{2-}$ complexes, where X = F, Cl, Br and I, as a function of symmetrical bond displacements relative to the minimum energy value of the optimized octahedral complex in the gas phase. The minimum-energy bond lengths from DFT calculations were Pt—F: 1.996 Å, Pt—Cl: 2.400 Å, Pt—Br: 2.555 Å and Pt—I: 2.770 Å. Reprinted with permission from [4], © John Wiley and Sons.

Computational studies on platinum–thallium (Pt–Tl) based transition metal complexes have shown that it is necessary to include solvation effects when calculating δ^{195}Pt since solvent molecules bind to the metal centre and affect the coordination sphere.[6] DFT based methods have led to reliable predictions of δ^{195}Pt values and show that the effects of the solvent on the NMR chemical shift turn out to be remarkably significant.[7] Pregosin noted the relatively large temperature dependence of the ^{195}Pt chemical shift, even broad-band ^{1}H-decoupling was shown to cause significant temperature variations, leading to chemical shift fluctuations ranging between 0.1-1 ppm/K.[1a] The order of increased shielding of ^{195}Pt nucleus for related amine

complexes is OSO_3^{2-} < OH_2 < H_2O < Cl_2 < NO_2 < Br_2 < NH_3 < SCN^- < I^- < thiourea < Me_2SO–S. For example: the complexes, *cis*-[Pt($^{15}NH_3$)$_2$(H_2O)$_2$], *cis*-[Pt($^{15}NH_3$)$_2$(^{15}NO)$_2$] and *cis*-[Pt($^{15}NH_3$)$_2$(SCN)$_2$]$^{2-}$ appear at -1593, -2214 and -3016 ppm, respectively.[8] The chemical shifts for Pt(IV) complexes often appear at higher frequency compared to Pt(II) and Pt(0) complexes. For example, using $[PtCl_6]^{2-}$ as our reference, $[PtCl_4]^{2-}$ = -1620; $[PtBr_6]^{2-}$ = -1860 and $[PtBr_4]^{2-}$ = -2690; $[Pt(CN)_6]^{2-}$ = -3866 and $[Pt(CN)_4]^{2-}$ = -4746 ppm. Further, it is known that the Pt(IV) halides alone span some 12500 ppm. For example, δ^{195}Pt $[PtF_6]^{2-}$ = 7326, δ^{195}Pt $[PtBr_6]^{2-}$ = -1860 and δ^{195}Pt $[PtI_6]^{2-}$ = -5120 ppm.[1c] ^{195}Pt NMR properties of simple Pt(IV) halide complexes have been studied by for example von Zelewsky,[9] Mason,[10] and Sadler[11] where the utility of ^{195}Pt NMR for their characterization is well illustrated. Notably, the work of Goodfellow *et al.* showed that the ten possible complexes $[PtCl_{6-n}(OH)_n]^{2-}$ could be identified in alkaline solution, based on their ^{195}Pt NMR chemical shifts, in addition to reporting the identification and ^{195}Pt NMR assignment of some of the hydrolysis products of $[PtCl_6]^{2-}$ in weakly acidic solutions (pH 1–3).[12]

1.2 Isotope Effects in Transition-Metal NMR

The isotope effects on chemical shifts of transition metal nuclei in diamagnetic complexes have been reported long before the age of high-resolution NMR experiments.[13] These effects are very large compared to those for other nuclei, when comparing the ranges of chemical shifts encountered.[14]

McFarlane *et al.*[13a] illustrated the remarkable sensitivity of δ(^{183}W) towards $^{13/12}$C isotopic substitution using ^{1}H-(^{183}W), ^{1}H-(^{31}P), and ^{1}H-(^{183}W,^{31}P) nuclear magnetic double- and triple-resonance experiments when determining tungsten-183 chemical shifts and other parameters in tungsten(0) complexes with tertiaryphosphine, q-cyclopentadienyl ligands. Bendall *et al.* [13b]reported a study on $^{1/2}$H isotope shifts in ^{59}Co NMR spectra. An isotope shift of 5 ppm per deuterium atom has been observed for the ^{59}Co resonance of tris(ethylenediamine)cobalt(III) chloride ($[Co(en)_3]Cl_3$) and hexaamminecobalt(III) chloride($[Co(NH_3)_6]Cl_3$) after exchange of hydrogen for deuterium. Naumann *et al.* [13c]reported similar isotope effects (^{1}H, ^{2}H) on the ^{93}Nb shielding of $[Et_4N][CpNb(X)(CO)_3]$ (X = H, D). An isotope shift of 6 ppm per deuterium was observed. The work on ^{51}V NMR by Rehder[13d] revealed the effect of

$C^{18}O$, ^{13}CO, $C^{18}O$, $^{1}H^{-}$ and $^{2}H^{-}$ substitution on the ^{51}V NMR chemical shift of $CpV(CO)_4$. A sizable isotope effect of 4.7 ppm is observed on going from $[CpV(CO)_3{}^{1}H]^{-}$ to $[CpV(CO)_3{}^{2}H]^{-}$. The mean isotope shift per ^{13}CO amounts to 0.46 ppm. The isotope shift per $C^{18}O$ substitution was found to be 0.10 ppm. In a study of water exchange rates in tetraaquaplatinum(II) and trans-di-chloridobis-aquaplatinum(II) using $H_2{}^{18}O$, Elding reported $^{16}O/^{18}O$ isotope effects induced in the ^{195}Pt NMR of several Pt(II) complexes,[15] as well as in $[PtCl(H_2O)_5]^{3+}$ ranging up to 1.0 ppm. Sadler *et al.*[16] demonstrated that at relatively high magnetic fields, the ^{195}Pt NMR resonance of the hexachloroplatinate(IV) anion could be resolved into a set of seven peaks ascribed to the $[Pt^{35/37}Cl_6]^{2-}$ species as a result of the natural $^{35}Cl/^{37}Cl$ isotope distribution.

More Recently, Murray *et al.* demonstrated that in a 14.7 Tesla magnetic field, the highly-resolved 128.8 MHz ^{195}Pt NMR resonances of $[PtCl_5(H_2O)]^{-}$ and *cis*-$[PtCl_4(H_2O)_2]$ show well resolved isotope effects, which serve as unique spectroscopic 'fingerprints' for the unambiguous identification of some of the aquated species derived from the hydrolysis of the $[PtCl_6]^{2-}$ anion in acidic solution, independent of the average chemical shift of these complexes.[17] It was also shown that the ^{195}Pt NMR peaks of $[PtCl_5(H_2O)]^{-}$ and *cis*-$[PtCl_4(H_2O)_2]$ complexes (see Fig. 1.3) under carefully controlled spectroscopic conditions are resolved not only according to the statistically expected isotopologues, but also in some cases due to the isotopomers possible for these species, depending on whether a ^{35}Cl or ^{37}Cl ion is *trans* to the coordinated water molecule for each isotopologue in a given complex. Isotopomers or isotopic isomers are isomers with isotopic atoms, having the same number of each isotope of each element but differing in their positions. Isotopologues are molecules that differ only in their isotopic composition. Simply, the isotopologue of a chemical species has at least one atom with a different number of neutrons than the parent.

These remarkable isotope effects demonstrate the high sensitivity of ^{195}Pt shielding to very small differences in the average $^{195}Pt–^{35}Cl$ compared to $^{195}Pt–^{37}Cl$ bond displacements in the various isotopologues and/or isotopomers possible for specific platinum complexes of a particular geometric structure. Recently, these isotope effects have been resolved for the hydroxide-chlorido complexes of Pt(IV) as shown in Figure 1.4. A key feature of hydroxide-chlorido complexes is the absence of isotopomers in the experimental spectra and will be addressed in this thesis.

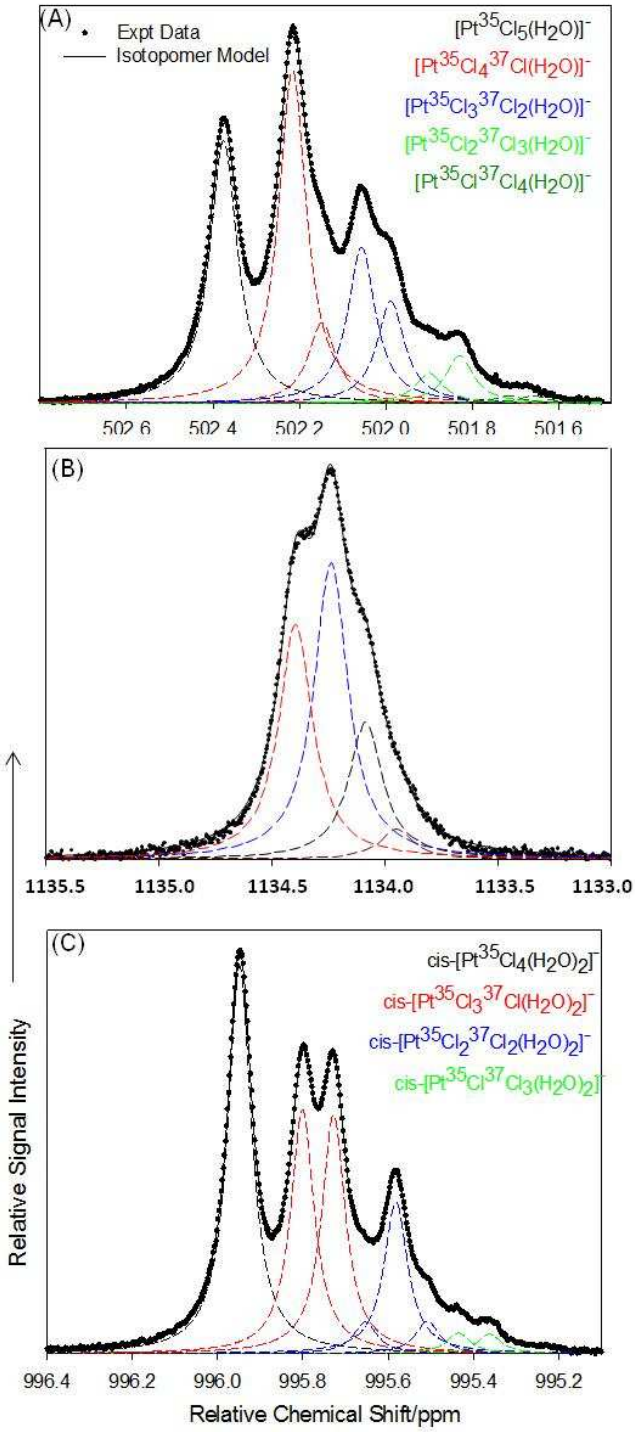

Figure 1.3: Expanded ^{195}Pt NMR spectra (●), showing the $^{35/37}$Cl isotope induced fine-structure for several species C–H from the $[Pt^{35/37}Cl_n(H_2O)_{6-n}]^{4-n}$ (n = 2–4) series; solid lines correspond to the non-linear least-squares fits of the isotopic model calculated from the statistically expected isotopologues, and where appropriate isotopomers, for each platinum complex.[2]

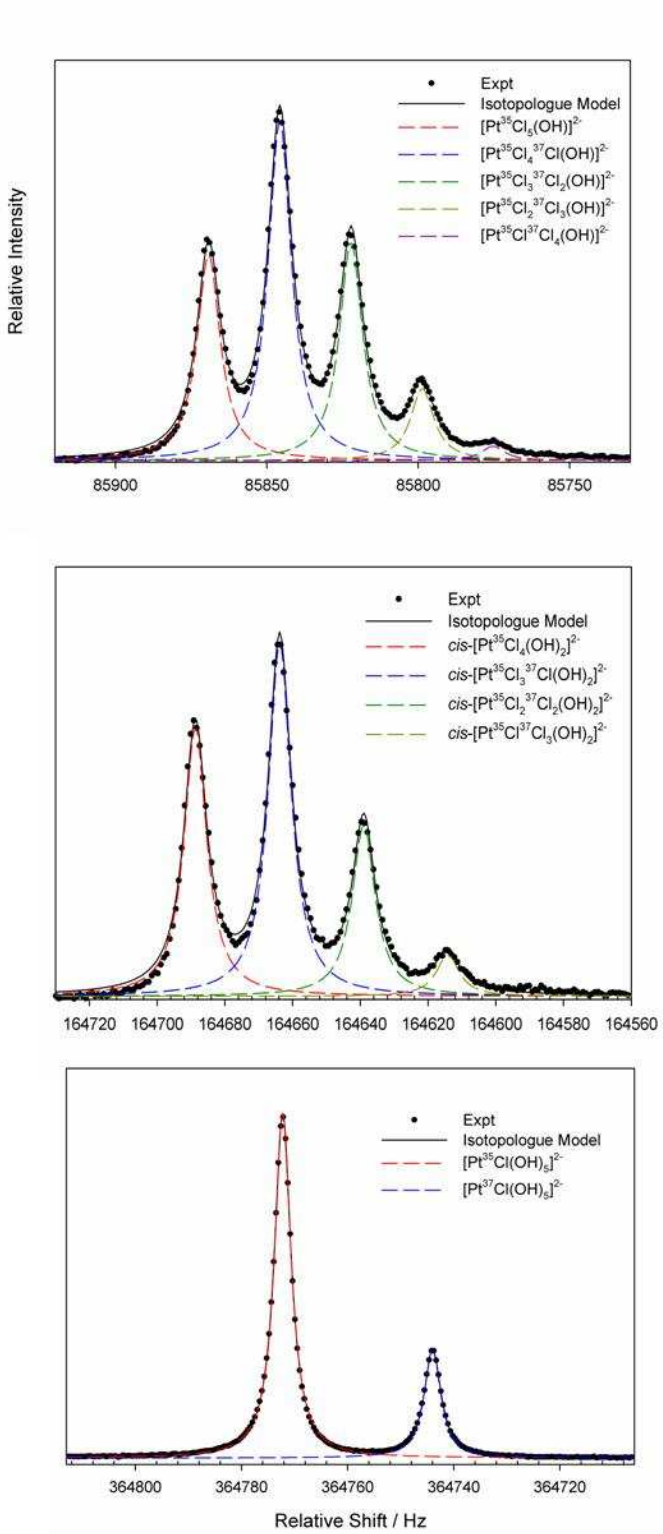

Figure 1.4: Expanded ^{195}Pt NMR spectra (●), showing the $^{35/37}$Cl isotope induced fine-structure for species from the $[Pt^{35/37}Cl_n(OH)_{6-n}]^{2-}$ (n = 2–5) series; solid lines correspond to the non-linear least-squares fits of the isotopic model calculated from the statistically expected isotopologues, and where appropriate isotopomers, for each platinum complex.[18]

Expansion of the ^{195}Pt NMR resonances is particularly interesting, since these all show well-resolved and remarkable fine-structure. Particularly interesting are the ^{195}Pt NMR peaks of the *cis*/*trans* isomer pairs B&C in Fig. 1.2. Under these conditions intermolecular ligand exchange and/or intramolecular scrambling of $[PtCl_n(H_2O)_{6-n}]^{4-n}$ (n = 2–6) complexes at 293 K is slow on the NMR time scale, resulting in each individual ^{195}Pt resonance displaying well resolved peaks as a result of the $^{35/37}$Cl isotopic distribution for the $[Pt^{35/37}Cl_n(H_2O)_{6-n}]^{4-n}$ (n = 2–6) isotopologues and isotopomers, as reported by Murray *et al.*[17] The statistical isotopologue distribution associated with each of the $[Pt^{35/37}Cl_n(H_2O)_{6-n}]^{4-n}$ (n = 2–6) species can be calculated using the equation[17],

$$P(n) = \sum_{n=0}^{n=((n+r)!)/(n!r!)} (\alpha^{n}_{^{35}Cl}\alpha^{r}_{^{37}Cl}) \qquad \ldots(1.1)$$

where P(n) is the statistical probability for an isotopologue at the fractional natural abundance (α) of 35Cl (0.7553) and 37Cl (0.2447), with n and r being the number of coordinated ^{35}Cl and ^{37}Cl ions respectively. Additionally, isotope effects were seen in solutions enriched in $H_2{}^{18}O$, where due to rapid exchange between metal-coordinated and solvent water ^{16}O/^{18}O splittings could be resolved.[2]

The distinctive fine-structure due to ^{35}Cl/^{37}Cl isotopologue and isotopomer effects is resolved at high magnetic fields for ^{103}Rh NMR signals of the series of $[RhCl_n(H_2O)_{6-n}]^{3-n}$ (n = 3–6) complexes (see Fig. 1.5) in equilibrated hydrochloric acid solutions, resulting in a unique NMR 'finger-print', with which it is possible to uniquely identify all chlorido containing Rh(III) complexes[19]. By this method the identity of the Rh(III) complex can readily be obtained from the fine-structure of the ^{103}Rh peaks, without reference to accurate ^{103}Rh NMR chemical shifts. This is potentially a considerable advantage, given the absence of a convenient and universal reference compound for ^{103}Rh NMR[20], resulting in considerable experimental error in measuring $\delta(^{103}Rh)$ chemical shifts, which can vary by as much as ±129 ppm for even the 'simple' $[RhCl_6]^{3-}$ species[21]. Moreover, the relatively small $\delta(^{103}Rh)$ difference of 66 ppm between two Rh(III) complex isomers such the *trans*-$[RhCl_2(H_2O)_4]^+$ and *cis*-$[RhCl_2(H_2O)_4]^+$ cations, makes it virtually impossible to reliably distinguish between such and other isomers in solution, on the basis of $\delta(^{103}Rh)$ chemical shifts alone. ^{103}Rh NMR is a rapid means of unambiguously characterizing $[RhCl_n(H_2O)_{6-n}]^{3-n}$ including possible *cis/trans* and *fac/mer* isomers.

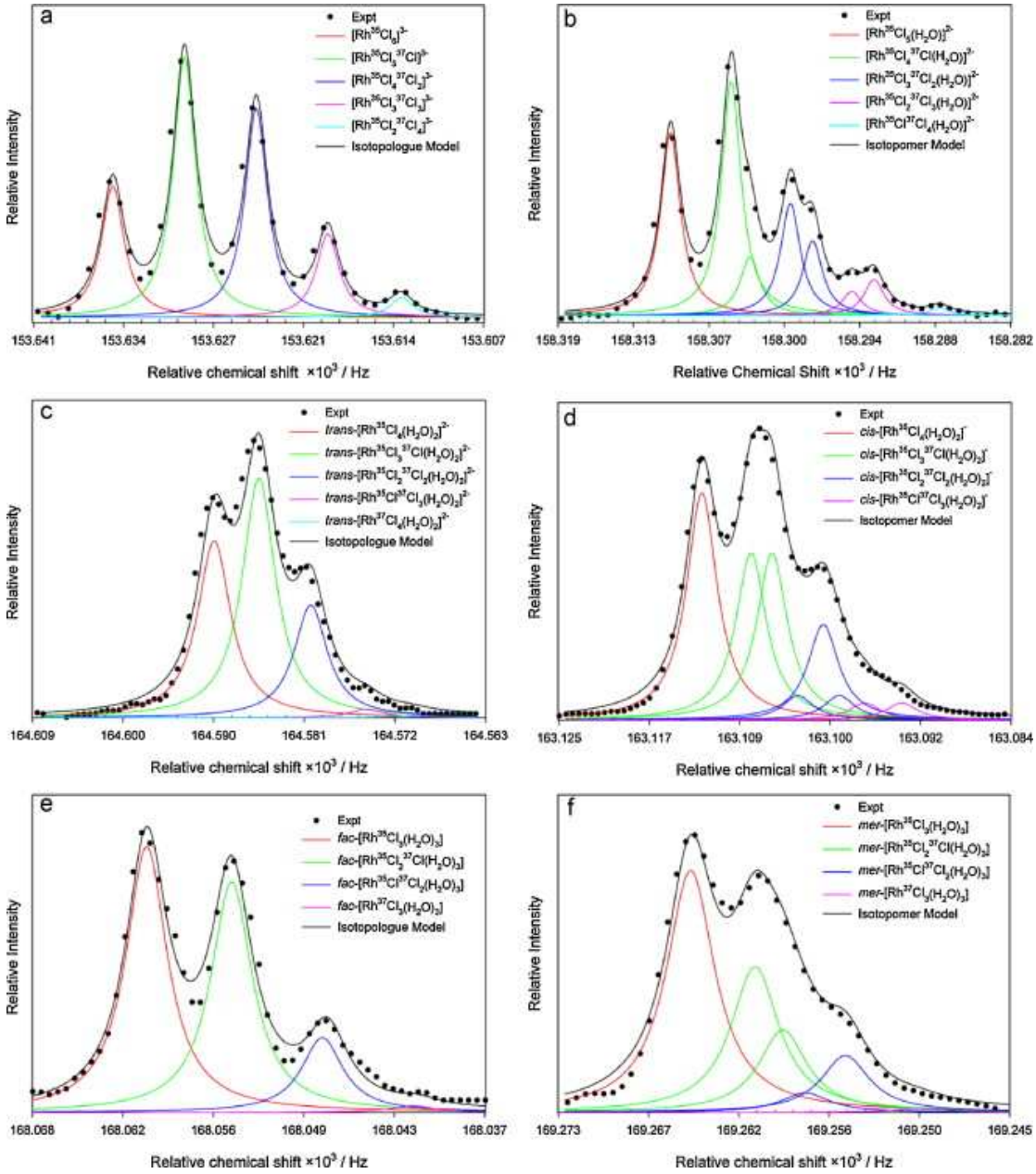

Figure 1.5: Experimental ^{103}Rh spectra of $[RhCl_n(H_2O)_{6-n}]^{3-n}$ (n = 3–6) species recorded at 292.1 K (symbols). The least-squares fits (solid lines) between experimental spectra of $[RhCl_6]^{3-}$ (a), *trans*-$[RhCl_4(H_2O)_2]^-$ (c) and *fac*-$[RhCl_3(H_2O)_3]$ (e) and the isotopologue model; the least-squares fits between the experimental spectra and the isotopologue model that includes isotopomers for the $[RhCl_5(H_2O)]^{2-}$, *cis*-$[RhCl_4(H_2O)_2]^-$ and *mer*-$[RhCl_3(H_2O)_3]$ species are denoted by (b), (d) and (f), respectively. Reprinted with permission from [19], © Elsevier.

Interpretation of the origin of these isotope effects in the ^{195}Pt NMR signals is achieved in the context of the elegant work of Jameson et al.[22] whose calculation of the mean M–X bond displacements for octahedral MX_6 molecules including $[PtCl_6]^{2-}$ and $[PtBr_6]^{2-}$ using L-tensor and Bartell methods with anharmonic force fields

showed that the expected nuclear shielding changes in M (and where appropriate X) as a result of isotope replacement (and/or temperature effects) should be directly correlated to the mean M–L bond displacement. Consequently a direct proportionality between the isotope induced shielding of, in this case, ^{195}Pt and the mass factor (m′-m)/m′ may be expected on ^{37}Cl for ^{35}Cl substitution. In general, as a heavier $^{37}Cl^-$ replaces a $^{35}Cl^-$ ion in the coordination sphere, increased shielding of the ^{195}Pt is observed for a given isotopologue of a given species, as a result of some slight Pt–Cl bond contraction; the extent of this effect measured by $\Delta\delta^{195}$Pt depends on the overall number of coordinated Cl^- ions and the structure of the complex, but there appears to be no obvious/simple correlation between the magnitude of the $\Delta\delta^{195}$Pt value and *n* in $[PtCl_n(H_2O)_{6-n}]^{4-n}$ (n = 2–5). It is noteworthy that the average chemical shift difference per ^{37}Cl i.e. between the individually resolved isotopologue resonances is only $\Delta\delta^{195}$Pt = 0.2 ppm ~ 29 Hz.

1.3 Calculation of Nuclear Shielding of Transition-Metals

Quantum-chemical computation of transition-metal chemical shifts is a stronghold of density-functional theory (DFT),[23] and the advent of relativistic methods such as the zero-order regular approximation (ZORA) have made ^{195}Pt NMR parameters amenable to computational study. [6, 24]

Non-relativistic metal shift calculations are only sensible for the 3d series. Relativistic effects on absolute shieldings can be noticeable for the 4d and 5d series. In many cases, the influence of the exchange-correlation functional on the δ values exceeds that of other sources, including relativity.

Hybrid functionals very often give results superior to those obtained with pure GGAs[25], and the reasons for the different performance of the different families of functionals have been investigated by Schreckenbach[26].

Computed metal chemical shifts are being used to assess newly developed density functionals [27]. A sizeable set of transition metal shifts has now been computed at a very uniform level of theory (i.e. B3LYP for GGA geometries), with the more recent extensions of this set encompassing ^{99}Ru[28], ^{55}Mn[29], and ^{49}Ti[30].

Except for $\delta(^{95}$Mo) [31], substituent effects on the metal shifts are captured very well, with an accuracy for each metal of typically a few percent of the respective chemical

shift range. The reasons for the deviations for $\delta(^{95}Mo)$ have not been analyzed yet; in this case, pure GGA functionals perform much better [31].

$\delta(^{59}Co)$ is well described for porphyrin and crown ether complexes with the B3LYP functional[32]. There have been attempts to compute metal chemical shifts using an ECP(see Section 2.3) on the metal in the NMR calculation; despite the lack of theoretical justification for such a procedure, reasonably good correlations between calculated and experimental $\delta(^{183}W)$ and $\delta(^{99}Ru)$ values have been obtained[33]. However, scaling factors on the order of 10-20 were necessary.

A combination of experimental and theoretical ^{103}Rh chemical shifts have been used to discriminate between two coordination modes of a hemilabile ligand[34]. Model calculations have shown that in Rh complexes with bidentate ligands, $\delta(^{103}Rh)$ is governed by the Rh–ligand bond distance and not by the bite angle, as previously reported in the literature[35]. Plausible structures for vanadate–peptide complexes have been supported by reasonably good accord between computed and reported $\delta(^{51}V)$ data[36]. DFT-derived ^{57}Fe chemical shifts have been used in the assessment of binding modes of CO, NO, and O_2 ligands in iron–porphyrin complexes, which serve as heme model compounds[37]. Following empirical precedence, theoretical metal shifts have been correlated with stabilities (i.e., computed reaction energies for ligand displacements)[38] or with reactivities approximated by computed activation barriers for the key step in a catalytic cycle[39]. Even though limited to specific families of compounds, such NMR reactivity correlations could be useful in optimizing and designing new homogeneous catalytic systems. More recently, a computational protocol based on molecular dynamics simulations has been applied to model thermal and solvent effects (as discussed under Section 1.1) on transition metal chemical shifts[40]. Variations on the order of a few dozen ppm, that is, small effects for a transition metal nucleus, have been noted for aqueous inorganic vanadate complexes[41] and for permanganate ion[42]. For $\delta(^{57}Fe)$ of the highly charged $[Fe(CN)_6]^{4-}$, however, much larger effects are found, exceeding 1000 ppm, due to the exceptional sensitivity of the iron shielding toward the metal–ligand bond distance, which is strongly affected by thermal averaging and by the interaction with the solvent[43].

The MD-derived, averaged shifts in water are in good agreement with experiment, suggesting that such simulations mimicking the actual conditions of the NMR experiment could be used to improve the accuracy of theoretical transition metal shifts in general.

From the 5d series onwards, a proper treatment of relativistic effects (see Section 2.3) is also mandatory for the metal chemical shifts. When the leading terms, including spin–orbit coupling, are included, general trends in the shielding values can be described at the Hartree–Fock level[44].

Methods and application of relativistic approaches to calculating nuclear shielding has been reviewed extensively.[40, 45] Arcisauskaite *et al.*[46] investigated the importance of relativistic effects on NMR shielding tensors and chemical shifts of linear HgX_2 (X=Cl, Br, I,CH_3) compounds using three different relativistic methods: the fully relativistic four-component approach and the two-component approximations, linear response elimination of small component (LR-ESC), and ZORA. LR-ESC reproduces successfully the four-component results for the ^{13}C isotropic shielding value in $Hg(CH_3)_2$ within 6 ppm but fails to reproduce the ^{199}Hg shielding tensors and chemical shifts. The latter is mainly due to an underestimation of the change in SO contribution. Even though ZORA underestimates the absolute (relative to the bare nucleus) Hg NMR shielding values by ~2100 ppm, the differences between ^{199}Hg chemical shift values obtained using ZORA and the four-component approach without spin–density contribution to exchange-correlation are less than 60 ppm for all compounds using three different functionals, BP86, B3LYP, and PBE0. However, larger deviations (up to 366 ppm) occur for ^{199}Hg chemical shifts in $HgBr_2$ and HgI_2 when ZORA results are compared with four-component calculations.[46] Despite the new developments in four-component relativistic calculations of shielding described above, most relativistic shielding calculations are carried out with various two-component methods, DFT/ZORA being the most commonly used method. Nuclear magnetic shieldings on the heavy atom for the systems $SnXH_3$ (X=H, F, Cl, Br, I), $SnXYH_2$ (X, Y=F, Cl, Br, I), and $PbXH_3$ (X=H, F, Br, I) were calculated using linear response elimination of small component method(LR-ESC) and compared to random phase approximation(RPA) calculations and then analyzed in order to determine the main trends and discuss the electronic origin of the shielding of two kinds of atoms involved in such systems: central and substituent atoms.[47] DFT/ZORA calculations have been carried out with or without SO in a large number of systems, for example: ^{195}Pt shieldings in halide, amino, and amidate complexes,[24b, 48] ^{207}Pb in cluster models of lead(II) halides,[49] ^{183}W in the polyoxometalates of W and Au[50] ^{77}Se shielding in 40 species.[51]

Heavy atom effects on light atoms have also been demonstrated theoretically for ^{17}O in $[UO_2(OH)_4]^{2-}$,[52] ^{13}C in monohalo (F, Cl, Br, I) organic compounds,[53] ^{13}C and ^{14}N shielding in 6-halo(Cl, Br, I) purines,[54] ^{29}Si with Pd and Pt,[55] ^{13}C in methyl hydride complexes of Rh and Ir,[56] and ^{19}F in uranium chlorofluorides.[57]

Temperature dependence and isotope shifts arise mainly from the change in the rovibrationally averaged geometry of the complex. Various approaches are available to account for the effect of rovibrational averaging. In general one needs a means of generating configurations over which the averages are taken and a means of generating the shielding for a given configuration.

Using zero-point vibrationally averaged structures, isotope effects on ^{59}Co chemical shifts have been reproduced and rationalized computationally.[58] In a cobaloxime[58a] and the hexamine cobalt(III) complex,[58b] the observed $^{1}H/^{2}H$ shifts on the order of ca. 50 ppm - 100 ppm could be traced back to small changes in the Co-N bonds, on the order of 0.001 Å- 0.006 Å, upon isotopic substitution. Because of their much smaller magnitude, typically 1 ppm or less,[59] the abovementioned isotope effects on ^{195}Pt or ^{103}Rh shifts pose a much bigger challenge to theory.

1.4 Aims and Objectives

This study aims to probe the origin of isotope effects on ^{195}Pt and ^{103}Rh NMR spectra, using zero-point corrections as a first step towards accurate modelling of these effects computationally.

This thesis is organized as follows: Chapter 2 discusses the fundamental principles and methods that are employed in this thesis. These include the chosen quantum-mechanical method, density functional theory (DFT) and its implementation in calculating NMR nuclear shielding. In addition, relativistic approximations are also discussed as it becomes important for heavier nuclei such as ^{195}Pt and ^{103}Rh.

Chapter 3 describes the particular computational protocol used in this study. In Chapter 4, a DFT study of the $^{35/37}Cl$ and $^{16/18}O$ induced isotope shifts in the ^{195}Pt NMR spectra of some prototypical Pt(IV) chlorido/aqua complexes, $[PtCl_{6-n}(H_2O)_n]^{n-2}$ (n=0-3) is presented. This is followed by Chapter 5 where the computational protocol is extended to $[Pt^{35/37}Cl_5(OH)]^{2-}$, *cis*-$[Pt^{35/37}Cl_4(OH)_2]^{2-}$, *fac*-$[Pt^{35/37}Cl_3(OH)_3]^{2}$, *cis*-$[Pt^{35/37}Cl_2(OH)_4]^{2-}$ and $[Pt^{35/37}Cl(OH)_5]^{2-}$, as well as their

$^{16/18}$OH isotopologues. In Chapter 6, the ^{35}Cl/^{37}Cl isotope shifts of Rh(III) aquo/chloride complexes $Rh^{35}Cl_n{}^{37}Cl_{5-n}(H_2O)]^{2-}$ (n=0-5), *cis*-$[Rh^{35}Cl_n{}^{37}Cl_{(4-n)}(H_2O)_2]^-$ (n=0-4), and *fac*-$Rh^{35}Cl_n{}^{37}Cl_{(3-n)}(H_2O)_3$ (n=0-3) are calculated using our computational protocol. Chapter 7 draws general conclusion from this study and finally, the Appendix contains the calculated zero-point corrected bond-lengths in individual isotopologues and isotopomers in this study.

Chapter 2

Theoretical Background

2.1 Many-particle quantum mechanics

The non-relativistic time-dependant Schrödinger equation describes how the wavefunction, Ψ, of a quantum particle changes with respect to time, t:

$$i\hbar \frac{\partial \Psi(\mathbf{r},t)}{\partial t} = H\Psi(\mathbf{r},t) \qquad \ldots(2.1)$$

where the Hamiltonian operator is[a]:

$$H = -\frac{\partial}{2\partial \mathbf{r}} + V(\mathbf{r},t) \qquad \ldots(2.2)$$

and V(**r**,*t*) is the potential both dependant on spatial coordinates, **r** and time *t*. The wavefunction describes the motion and distribution of quantum particles and contains everything that can be known about the system. The wavefunction by itself has no physical significance, instead the square of the modulus of the wavefunction, i.e. the probability density, yields the probability that the particle will be at **r** when multiplied with the volume element d**r.**

$$\left|\Psi(\mathbf{r})\right|^2 d\mathbf{r} \qquad \ldots(2.3)$$

When the time-independent potential operator, V(**r**), is used, the time-independent Schrödinger equation can be written as:

$$H\psi(\mathbf{r}) = E\psi(\mathbf{r}) \qquad \ldots(2.4)$$

where E is the energy eigenvalue of the eigenfunction, ψ. This equation can in principle be solved to produce the ground and excited state wavefunctions for any quantum system with a time-independent potential.

[a] Atomic units (a.u.) have been used throughout this chapter.

For many-particle systems like an atom, however, the Schrödinger equation becomes more complex due to the interdepency of nuclear and atomic motion and becomes analytically insolvable as can be seen from the Hamiltonian of a system containing nuclei and electrons:

$$H = -\sum_i \frac{1}{2}\nabla_i^2 - \sum_k \frac{1}{2m_k}\nabla_k^2 - \sum_i \sum_k \frac{Z_k}{r_{ik}} + \sum_{i<j} \frac{1}{r_{ij}} + \sum_{k<l} \frac{Z_k Z_l}{r_{kl}} \qquad \ldots(2.5)$$

where *i* and *j* are the indices of the electrons and *k* and *l* are the indices of the nuclei. The first and second terms of Eq. 2.5 describe the kinetic energy of the electrons and nuclei, the third term describes the potential energy between the electrons and nuclei, and the fourth and fifth terms describe the potential energy of electron-electron and nuclei-nuclei interactions. The Born-Oppenheimer approximation separates nuclear and electronic motion, which is partially feasible due to the fact that nuclei and electrons move on different timescales due to their large mass differences. Hence, the kinetic energy due to nuclear motion can be ignored and the electronic Schrödinger equation can be solved by only including the potential energy (for each set of nuclear positions):[60]

$$(H_{elec} + V_{NN})\Psi_{elec} = E_{elec}\Psi_{elec} \qquad \ldots(2.6)$$

$$H_{elec} = -\sum_i \frac{1}{2}\nabla_i^2 - \sum_i \sum_k \frac{Z_k}{r_{kl}} + \sum_{i<j} \frac{1}{r_{ik}} \qquad \ldots(2.7)$$

$$V_{NN} = \sum_{k<l} \frac{Z_k Z_l}{r_{kl}} \qquad \ldots(2.8)$$

The electronic Schrödinger equation (Eq. 2.6) is solved for one set of nuclear coordinates that enter into the second term of Eq. 2.7 and into Eq. 2.8. Solving the Schrödinger equation for different sets of nuclear coordinates yields the Born-Oppenheimer potential energy surface (PES). Applying the Born-Oppenheimer approximation result in a simple point-charge model for the atomic nuclei, which are stationary at 0 K.

The nuclear kinetic energy which is ignored in the electronic Schrödinger equation can later be recovered by solving a nuclear Schrödinger equation:

$$\left(-\sum_k \frac{1}{2m_k}\nabla_k^2 + V(r_N)\right)\psi_{nuc} = E\psi_{nuc} \qquad \ldots(2.9)$$

where the electronic interaction enters as a potential $V(\mathbf{r}_\mathbf{N})$ dependent on nuclear coordinates. The electronic potential has to be approximated, usually as a harmonic potential based on the electronic solution. This enables one to recover the zero-point energy as well as temperature-dependent vibrational motion that can be used to calculate energies, entropies and free energies at any temperature using the equations of statistical mechanics. A more detailed description of the consequences of the Born-Oppenheimer approximation and the quantum mechanical remedy thereof is discussed in Section 2.4.

2.2 Solving the Schrödinger equation

2.2.1 The Variational Principle

Any many-body problem containing three or more interdependent particles is analytically insolvable, hence, more approximations are made in order to perform these computations.

The variational principle is most commonly used, stating that if a system with Hamiltonian **H** is described by an allowed trial wavefunction ψ_{trial} then the following equation holds:

$$\frac{\int \psi^*_{trial}\, H\psi_{trial}\, d\mathbf{r}}{\int \psi^*_{trial}\, \psi_{trial}\, d\mathbf{r}} = E_{trial} \geq E_0 \qquad \ldots(2.10)$$

where ψ^* is the complex conjugate of ψ, E_{trial} is the energy of the trial wavefunction and the exact groundstate energy, E_0. The inequality thus guarantees

that the energy of the trial wavefunction will always be higher or equal to the real energy of the real wavefunction. The exact wavefunction can thus be approached either by trying all possible wavefunctions allowed by the number of particles or to systematically improve the trial wavefunction until its energy cannot get lower.

2.2.2 Hartree-Fock theory

Even though the Born-Oppenheimer approximation and the variational principle together provide a route towards finding the electronic wavefunction we cannot search through all possible trial wavefunctions having the correct number of electrons as there are simply too many possibilities and in fact we need a form for the wavefunction on which the Hamiltonian can operate. However, approximating the *N*-electron wavefunction as a linear combination of 1-electron wavefunctions provides a convenient starting point. Such an allowed wavefunction is the Slater determinant which is an antisymmetric product of 1-electron wavefunctions(i.e. that $\psi_{SD} = -\psi_{SD}^{T}$) which consequently obeys the Pauli exclusion principle i.e. that electrons are indistinguishable and cannot be in the same quantum state:

$$\psi_{SD} = \frac{1}{\sqrt{N!}} \begin{vmatrix} \phi_1(\mathbf{x}_1) & \phi_2(\mathbf{x}_1) & \cdots & \phi_N(\mathbf{x}_1) \\ \phi_1(\mathbf{x}_2) & \phi_2(\mathbf{x}_2) & \cdots & \phi_N(\mathbf{x}_2) \\ \vdots & \vdots & \ddots & \vdots \\ \phi_1(\mathbf{x}_N) & \phi_2(\mathbf{x}_N) & \cdots & \phi_N(\mathbf{x}_N) \end{vmatrix} \qquad \ldots(2.11)$$

The $\phi_i(\mathbf{x})$ are the 1-electron wavefunctions, called spin orbitals i.e. products of both a spatial orbital and a spin function. The spin orbitals are functions of both spatial and spin degrees of freedom, together denoted $(\mathbf{x})$.

Now we can use the Born-Oppenheimer Hamiltonian and the variational principle to minimise the wavefunction(Slater determinant) to yield the ground state wavefunction and the ground state energy. When using atomic units the mass and charge of the electron and Planck's constant turn out to be unity.

This leads to the Hartree-Fock energy equation:

$$E_{HF} = \langle \psi_{SD} | H_{elec} + V_{NN} | \psi_{SD} \rangle = \sum_i \langle \phi_i | h | \phi_i \rangle + \frac{1}{2} \sum_i \sum_j \langle \phi_i \phi_i | \phi_j \phi_j \rangle - \langle \phi_i \phi_j | \phi_j \phi_i \rangle + V_{NN} \quad \ldots(2.12)$$

where we have introduced the Dirac short hand notation. The individual terms of eq. 2.12 are:

$$\langle \phi_i | h | \phi_i \rangle = \int \phi_i^*(\mathbf{x}) \left(-\frac{1}{2} \nabla^2 - \sum_k \frac{Z_k}{r_{ik}} \right) \phi_i(\mathbf{x}) d\mathbf{x} \quad \ldots(2.13)$$

$$\langle \phi_i \phi_i | \phi_j \phi_j \rangle - \langle \phi_i \phi_j | \phi_j \phi_i \rangle =$$
$$\iint |\phi_i(\mathbf{x}_1)|^2 \frac{1}{r_{12}} |\phi_j(\mathbf{x}_2)|^2 d\mathbf{x}_1 d\mathbf{x}_2 - \iint \phi_i(\mathbf{x}_1) \phi_j^*(\mathbf{x}_1) \frac{1}{r_{12}} \phi_j(\mathbf{x}_2) \phi_i^*(\mathbf{x}_2) d\mathbf{x}_1 d\mathbf{x}_2 \quad \ldots(2.14)$$

Eq. 2.13 is an integral that describes the kinetic energy and the nucleus-electron interaction and is a 1-electron equation. Eq. 2.14 shows two double integrals that describe the electron-electron repulsion. The first term is the Coulomb integral (often denoted J_{ij}) that represents the electrostatic repulsion of two smeared out charge clouds while the second term is the exchange integral (often denoted K_{ij}) that is hard to interpret classically, but arises due to the antisymmetry of the Slater determinant that was enforced.

As we have built up the many-electron wavefunction from 1-electron wavefunctions (orbitals), our variational freedom now comes from varying the orbitals (with the constraint that the orbitals must remain orthonormal) and thus we can minimise the whole energy expression by choosing the best orbitals. This is achieved by solving the Hartree-Fock equations[61]:

$$f\phi_i = \epsilon_i \phi_i \quad \ldots(2.15)$$

for each electron where ϵ_i are the eigenvalues to the Fock operator f which is defined as:

$$f = -\frac{1}{2} \nabla_i^2 - \sum_k \frac{Z_k}{r_{ik}} + V_{HF} \quad \ldots(2.16)$$

where V_{HF} is the Hartree-Fock potential which is an average repulsive potential (defined by Coulomb and exchange operators, not shown) due to all the electrons except for the one which is being solved. As the Fock operator both operates on the orbitals and depends on the orbitals through the Hartree-Fock potential, the Hartree-Fock equations have to be solved self-consistently by first guessing the initial orbitals and then iterating until the orbitals stop changing. Once self-consistent orbitals are available, the Hartree-Fock energy equation (Eq. 2.12) gives the Hartree-Fock total energy while the orbital energies can be interpreted as approximate ionisation energies of electrons from the orbitals that they occupy.

2.2.3 Density functional theory

Density functional theory solves the Schrödinger equation by establishing the total electron density as the quantity to derive the ground state energy from, instead of the many-electron wavefunction.

The Born-Oppenheimer Hamiltonian (Eqs. 2.7 and 2.8) for any molecule is fully determined by the number of electrons *N* and the electron-nucleus potential *V* (which is specified by nuclear positions and nuclear charges) and leads to a unique ground state Born-Oppenheimer energy and associated wavefunction of a molecule. DFT is a method to circumvent calculating the complicated wavefunction. The electron density, $\rho(\mathbf{r})$, can be defined as a multiple integral of the square of the wavefunction over the spin coordinates of all electrons and over all but one spatial coordinate.[61]

$$\rho(\mathbf{r}) = N\int ...\int |\psi(\mathbf{r})|^2 dsdx_2...dx_{\mathbf{N}} \qquad ...(2.17)$$

It gives the probability that any of the N electrons of the system of any spin is found within the volume element and is a simple function of the spatial coordinates. The electron density is experimentally observable, from X-ray diffraction for instance.

This simple quantity turns out to contain all the necessary information: the number of electrons, N, can be determined by integrating over $\rho(\mathbf{r})$, and the nuclear positions and charges show up as cusps of $\rho(\mathbf{r})$.[62] That the nuclear positions and charges i.e.

the electron-nucleus potential v can be uniquely deduced from $\rho(\mathbf{r})$ is the subject of the first Hohenberg-Kohn theorem.[63]

It should thus be possible to come up with an energy functional (a functional is a special type of function whose argument is another function) whose argument is the electron density and determines the ground state energy. The energy functional would have to account for the electronic kinetic energy, the nucleus-electron interaction energy and the electron-electron interaction energy (the trivial nucleus-nucleus repulsion term is ignored in all following equations) in some way:

$$E[\rho(\mathbf{r})] = T[\rho(\mathbf{r})] + E_{Ne}[\rho(\mathbf{r})] + E_{ee}[\rho(\mathbf{r})] \qquad \ldots(2.18)$$

where $T[\rho(\mathbf{r})]$ is the kinetic energy term, $E_{Ne}[\rho(\mathbf{r})]$is the electron-nucleus term and $E_{ee}[\rho(\mathbf{r})]$ is the electron-electron interaction term, all expressed in terms of $\rho(\mathbf{r})$. The $E_{Ne}[\rho(\mathbf{r})]$ term is easy to express as a functional of the density, but it is far from obvious how to express $T[\rho(\mathbf{r})]$ and $E_{ee}[\rho(\mathbf{r})]$ in terms of $\rho(\mathbf{r})$

Another problem concerns finding the ground state density with such an expression instead of just any density. Luckily, the second Hohenberg-Kohn theorem[63] provides density functional theory with its own variational principle which states that any trial density $\rho_{trial}(\mathbf{r})$ will always be higher in energy (or equal) than the real $\rho_{exact}(\mathbf{r})$and thus Eq. 2.18 can simply be tried for a number of trial densities or somehow minimised by systematically improving the trial density.

A simple expression of the $T[\rho(\mathbf{r})]$ kinetic energy term has been the subject of various attempts, some dating back to the early days of quantum mechanics, e.g. the Thomas-Fermi model.[64] In order to circumvent this problem some arguments from Hartree-Fock theory can be borrowed. By considering a fictitious system of non-interacting particles described by a Slater determinant of 1 electron orbitals, a non-interacting trial density $\rho_{KS}(\mathbf{r})$ can be constructed, as suggested by Kohn and Sham:[65]

$$\rho_{KS}(\mathbf{r}) = \sum_i \int |\phi_i(\mathbf{x})|^2 ds \qquad \ldots(2.19)$$

By requiring $\rho_{KS}(\mathbf{r})$ to be equal to $\rho(\mathbf{r})$ one can still work with the exact equations of DFT and Eq. 2.17 can be rewritten as:

$$E[\rho(\mathbf{r})] = T_{KS}[\rho(\mathbf{r})] + E_{Ne}[\rho(\mathbf{r})] + J[\rho(\mathbf{r})] + E_{XC}[\rho(\mathbf{r})] \quad \ldots(2.20)$$

where the kinetic energy term is defined as:

$$T_{KS}[\rho(\mathbf{r})] = -\frac{1}{2}\sum_i \langle \phi_i | \nabla^2 | \phi_i \rangle \quad \ldots(2.21)$$

The electron-nucleus term is:

$$E_{Ne}[\rho(\mathbf{r})] = -\sum_k Z_k \int \rho(\mathbf{r}) r_{ik}^{-1} d\mathbf{r} \quad \ldots(2.22)$$

and the Coulomb term is:

$$J[\rho(\mathbf{r})] = \frac{1}{2}\iint \rho(\mathbf{r_1})\rho(\mathbf{r_2}) r_{ik}^{-1} d\mathbf{r_1} d\mathbf{r_2} \quad \ldots(2.23)$$

where we have split the previous $E_{ee}[\rho(\mathbf{r})]$ term into a trivial Coulomb interaction term $J[\rho(\mathbf{r})]$ (calculated as in Hartree-Fock theory) and a new $E_{XC}[\rho(\mathbf{r})]$ term. While it may not be obvious, no approximation has been made. The $E_{XC}[\rho(\mathbf{r})]$ term, however, has become a rather complicated term, which must now account for a correction to the kinetic energy [not accounted for by the $T_{KS}[\rho(\mathbf{r})]$ term) as well as electron- electron repulsion not accounted for by the smeared charge cloud term $J[\rho(\mathbf{r})]$. Assuming an expression for $E_{XC}[\rho(\mathbf{r})]$ can be given, we can next use the Hohenberg-Kohn variational principle to solve the Kohn-Sham single particle equations to minimise the density as it is now expressed in orbitals:

$$\left(-1\frac{1}{2}\nabla^2 + \nu_{eff}(\mathbf{r})\right)\phi_i(\mathbf{x}) = \epsilon_i \phi_i(\mathbf{x}) \quad \ldots(2.24)$$

where the effective potential, $\nu_{eff}(\mathbf{r})$ contains the nucleus-electron, Coulomb and exchange-correlation potentials.

The Kohn-Sham DFT equations are very similar to the Hartree-Fock equations and are also solved self-consistently and by the same type of computational techniques. The main difference is the absence of a *K* exchange term (which we will come back to) and the occurrence of an exchange-correlation term. The exchange-correlation energy can be thought of as the mutual avoidance of electrons due to the "personal space" (exchange-correlation hole) of each electron.

If an exact expression of the exchange-correlation term, $E_{XC}[\rho(\mathbf{r})]$, would be given, then solving the Kohn-Sham equations would lead to the exact solution to the Born-Oppenheimer Schrödinger equation. There is, however, no way of knowing this exact expression and educated guesses of its form must be used instead, which means that in practice DFT is always an approximate theory that suffers from the fact that its approximations are not easily systematically improvable unlike approximations based on wavefunction theory (WFT).

Theoretical developments of density functional theory for the last decades have thus been focused on "guessing" the exchange-correlation term, utilising various clues about its nature. This involves finding forms for the exchange and correlation energy that correctly describe the energy or density of model systems whose properties are well or exactly known. One of these model systems is the uniform electron gas, jellium, whose properties are well known from almost exact quantum Monte Carlo calculations. The local density approximation (LDA) is a constituent of almost all exchange-correlation functionals in common use, and it is partly based on deriving a functional form (involving $\rho(\mathbf{r})$) that describes the properties of jellium well. Different exchange and correlation functionals based on the LDA approximation have been derived.[66] It turns out that the LDA approximation results in very inaccurate DFT energies when applied to molecules. In order to go beyond the LDA approximation, one strategy is to use the gradient of $\rho(\mathbf{r})$as an ingredient in increasingly complex formulas for exchange and correlation respectively. The generalized gradient approximation (GGA) is the most successful gradient corrected approximation to LDA which comes in numerous different varieties nowadays. A common gradient corrected exchange functional is the one by Becke (B88 or B)[67]. It is often combined with various different correlation functionals such as LYP[68] and P86[69] Many different strategies have been employed in deriving other exchange-

correlation functionals including better LDA approximations, density-gradient expansion, constraint satisfaction, modelling of the exchange-correlation hole, empirical fits and mixing in Hartree-Fock exchange.[70]

The mixing in of Hartree-Fock exchange (from Eq. 2.14) as first suggested by Becke [71] has been a particularly successful strategy, resulting in the very popular hybrid functionals that include both an expression of DFT exchange (usually one of the GGA exchange functionals) and Hartree-Fock exchange from Hartree-Fock theory, the two terms scaled empirically to avoid double counting. The inclusion of Hartree-Fock exchange introduces an explicit orbital-dependent term that is more expensive to compute than the other exchange-correlation terms, making hybrid functionals more expensive than LDA and GGA functionals. The very popular hybrid functional B3LYP is a 20 % Hartree-Fock exchange hybrid and is defined as follows:[72]

$$E^{B3LYP} = E_{XC}^{LDA} + 0.2\left(E_X^{HF} - E_X^{LDA}\right) + 0.72\left(E_X^{B88} - E_X^{LDA}\right) + 0.81\left(E_C^{LYP} - E_C^{LDA}\right) \quad \ldots(2.25)$$

where E_X^{LDA} and E_C^{LDA} are the VWN local-density approximation[66b] to the exchange and correlation functionals respectively. E_X^{B88} and E_C^{LYP} are the Becke 88[67] exchange functional and the correlation functional of Lee, Yang and Parr[68]. Other hybrid functionals are defined in a similar way, with different exchange and correlation functionals used and a different amount of Hartree-Fock exchange. Hybrid functionals have been found to be the most successful functionals for general maingroup thermochemistry.

The reason for the success of the hybrid-DFT approach seems to partly stem from the self-interaction problem that plagues many LDA and GGA functionals and which particularly affects the accuracy of reaction barrier heights. The self-interaction problem comes from the Coulomb term $J[\rho(\mathbf{r})]$ of the DFT energy expression where an interaction of the electron with itself is calculated like in Hartree-Fock theory. However, in Hartree-Fock theory, the calculated Coulomb and exchange terms cancel exactly, removing this self-interaction, while in DFT there is no such full cancellation term. Mixing in a fraction of Hartree-Fock exchange seems to reduce the self-interaction problem of DFT.

The most successful density functionals for maingroup chemistry at the moment seem to be the double hybrid functionals which can be regarded as a mixture of hybrid DFT and the wavefunction theory method MP2 where the unoccupied DFT orbitals are used to calculate an additional correlation term by second order perturbation theory. [73]Their applicability for transition metal chemistry is less clear, however.[74]

2.2.4 Basis sets

Hartree-Fock and DFT methods depend on the use of 1-electron wavefunctions or orbitals to build up the many-electron wavefunction or the electron density.
In a molecule, the self-consistent HF/DFT orbitals can end up having a complicated shape and in order to give the greatest flexibility, it is useful to take linear combinations of many different functions:

$$\phi_i(\mathrm{x}) = \sum_{\mu} c_{\mu i}\varphi_{\mu}(\mathrm{x}) \qquad \ldots(2.26)$$

where φ_{μ} are called basis functions and $c_{\mu i}$ basis set or expansion coefficients. In molecular quantum chemistry, atom-centered basis functions are mostly used while in the solid state quantum chemistry/physics community, delocalised planewave basis functions are a better approximation.

The exact wavefunctions of the l-electron hydrogen atom have served as inspiration for the form of these atom-centered basis functions. The hydrogen atom wavefunctions can be described by products of spherical harmonics and exponential functions, $e^{-\alpha r}$. Slater-Type Orbitals (STO's) use Slater basis functions, i.e.

$$f(\boldsymbol{r}) = Y_{lm} r^n e^{-\zeta r} \qquad \ldots(2.27)$$

The center of the function is at a nucleus, the Y_{lm} are spherical harmonics, and the exponential factor ζ (zeta) determines the long-range decay of the function. Slaters resemble the true atomic orbitals more closely than Gaussian ($e^{-\alpha r^2}$) basis functions. Slaters can display the correct nuclear cusp and asymptotic decay. This leads to a

more accurate and more intuitive description of the molecular orbitals at the same size of basis set.

Traditionally, however, Gaussians ($e^{-\alpha r^2}$) have been used in quantum chemical calculations, because they are in many ways more suitable to evaluate the integrals of Hartree-Fock and density functional theory. A Gaussian-type orbital (GTO) is usually calculated as:[60]

$$X^{GTO}(x,y,z;\alpha,i,j,k)=\left(\frac{2\alpha}{\pi}\right)^{3/4}\left[\frac{(8\alpha)^{i+j+k}\,i!\,j!\,k!}{(2i)!(2j)!(2k)!}\right]^{1/2}x^i y^j z^k e^{-\alpha\left(x^2+y^2+z^2\right)} \quad \ldots(2.28)$$

using Cartesian coordinates (instead of spherical coordinates), where the integers i, j and k determine the shape of the orbital and α is the exponent. For example: when $i = j = k = 0$ a spherically symmetric s orbital is defined, analogous to the ground state wavefunction of the hydrogen atom.

Gaussian-type orbitals, however, do not resemble the hydrogen wavefunctions as well as their exponential counterparts, Slater-type orbitals (STOs) where the latter have the correct cusp behaviour at the nucleus and the correct radial decay which the GTOs lack. In order to mimic the behaviour of STOs using GTOs, a strategy has been to make linear combinations of a few GTOs (with different exponents of each GTO):

$$\varphi_\tau(\mathrm{x})=\sum_a d_{a\tau}x_a^{GTO}(\mathrm{x}) \quad \ldots(2.29)$$

where φ_r is called a contracted Gaussian basis function and $d_{a\tau}$ is the contraction coefficient. Usually, only a few GTOs are used in each contracted basis function and importantly the contraction coefficients are fixed and not values to be variationally optimised.

Basis functions intended for a molecular calculation together form a basis set and the convergence behaviour of basis sets have been much studied over the years. Appropriate exponents, contractions and types of the basis functions are usually pre-optimised for each element and are remarkably transferable. Typically, the lowest energy (core) orbitals change very little from one molecule to the next and remain atom-like. This means that they can be described very efficiently by a low number of basis functions and often a greater degree of contraction than the valence orbitals. This observation lead to the development of the popular split-valence basis set family.

A popular split-valence basis set is 6-31G[75] which is available for many elements. If the orbital structure of a carbon atom is described by this basis set then that means that the 1s core orbital is described by a single contracted basis function which is a linear combination of 6 GTOs. Each valence orbital on the other hand $(2s,2p_x,2p_y,2p_z)$ is described by a linear combination of two contracted basis functions, one of which is described by 3 GTOs and the other by 1 GTOs. In total this adds up to 9 contracted basis functions and 22 GTOs that adequately describes a carbon atom in molecular calculations. The 6-31G basis set is called a double-zeta basis set as the valence orbitals are described by double the amount of contracted basis functions than a minimal description (a minimal basis set uses only 1 basis function for each orbital) for even more flexibility. It turns out that for very accurate calculations, a few contracted basis functions (4-6) for each valence orbital are necessary for accurate post-HF calculations, while triple-zeta basis sets are often sufficient for Hartree-Fock and DFT calculations. However, even a great number of basis functions is not always enough. For an accurate description of the carbon atom, especially when part of a molecule, one cannot rely solely on basis functions of the s and p type. For additional flexibility of the valence orbitals, polarisation functions are typically added (usually of the next higher angular momentum type). For a carbon atom, a set of d polarisation functions (single GTOs) would be added to each p basis function of the 6-31G basis set, resulting in the 6-31G(d) or 6-31G* basis set.[76] Polarisation functions turn out to be crucial to describe molecules well and are almost always included in basis sets. Additionally, diffuse functions are sometimes added to basis sets for a better description of diffuse orbitals, which is usually necessary when calculating anions for example. Low-exponent basis functions (single GTOs) of various types are then added to the basis set. A 6-31G(d) basis set augmented with diffuse functions is named 6-31+G(d).[77]

Using a pseudo-potential function, some of the relativistic effects discussed in Section 2.3 will be recovered. It is based on the assumption that only valence electrons are dominant in bonding interactions and so, we can safely model the combined nuclear and electronic core of an atom by a pseudo-potential function of effective core potential(ECP)[78].

2.3 Relativistic quantum chemistry

Initially, quantum mechanics was developed without considering the effect of relativity. As per convention, relativistic effects are those discrepencies between values calculated by models considering and not considering relativity. It is by now well accepted that relativistic effects play an important role in our understanding of molecular properties of the heavy elements.[79]

One of the consequences of the constant speed of light is that the mass of a particle, which moves at a substantial fraction of *c*, increases over the rest mass m_0. The energy of a 1s-electron in a hydrogen-like system(i.e. one nucleus and one electron) is $Z^2/2$, and classically this is equal to minus the kinetic energy, $1/2mv^2$, owing to the virial theorem ($E = -T = \frac{1}{2}V$). In atomic units, m = 1 the classical velocity of a 1 s electron is thus *Z*. The speed of light in atomic units is 137.036, and it is clear that relativistic effects cannot be neglected for the core electrons in heavy nuclei.[80] For atoms with large *Z*, the 1s-electrons are relativistic and thus heavier, which has the effect that the 1s-orbital shrinks in size by the same factor as the mass increases as shown in Eq. 2.30 and Eq. 2.31, where a is the radius of the 1s orbital and m is the mass of an electron.

$$m = m_0\left(\sqrt{1-\frac{v^2}{c^2}}\right)^{-1} \qquad \ldots(2.30)$$

$$a = a_0\left(\sqrt{1-\frac{v^2}{c^2}}\right) \qquad \ldots(2.31)$$

The central theme in relativity is that the speed of light, *c*, is constant in all inertial frames. Augmented with the requirement that physical laws should be identical in such frames, this has as a consequence that time and space coordinates become inseparable or “equivalent”. A relativistic description of a particle thus requires four coordinates, three space and one time coordinate. The latter is usually multiplied by *c* to have units identical to the space variables. A change between different coordinate systems can be described by a *Lorentz transformation*,[81] which may mix space and time co-ordinates:

$$\begin{aligned} t' &= \frac{t - \frac{v}{c^2}x}{\sqrt{1 - \frac{v^2}{c^2}}} \\ x' &= \frac{x - vt}{\sqrt{1 - \frac{v^2}{c^2}}} \\ y' &= y \\ z' &= z \end{aligned} \qquad \ldots(2.32)$$

The postulate that physical laws should be identical in all coordinate systems is equivalent to the requirement that equations describing the physics must be invariant to a Lorentz transformation. Considering the time-dependent Schrödinger equation it is clear that it is not Lorentz invariant since the derivative with respect to space coordinates is of second order, but the time derivative is only first order. Eq. 2.33 is a more explicit formulation of Eq. 2.1. The fundamental structure of the Schrödinger equation is therefore not relativistically correct.

$$\left[-\frac{1}{2m}\left(\frac{\partial^2}{\partial x^2}+\frac{\partial^2}{\partial y^2}+\frac{\partial^2}{\partial z^2}\right)+\mathbf{V}\right]\Psi = i\frac{\partial \Psi}{\partial t} \qquad \ldots(2.33)$$

For a free electron, Dirac proposed that the (time-dependent) Schrödinger equation should be replaced by Eq. 2.34.[80] Here α and β are 4 × 4 matrices, α is written in terms of the three Pauli 2 × 2 spin matrices σ and β in terms of a 2 × 2 unit matrix **I.** The momentum operator $p = -i\nabla$ involves a first-order differentiation with respect to the space variables.

$$[c\boldsymbol{\alpha}\cdot\mathbf{p}+\beta mc^2]\Psi = i\frac{\partial \Psi}{\partial t} \qquad \ldots(2.34)$$

$$\boldsymbol{\alpha}_{x,y,z} = \begin{pmatrix} 0 & \boldsymbol{\sigma}_{x,y,z} \\ \boldsymbol{\sigma}_{x,y,z} & 0 \end{pmatrix} \qquad \beta = \begin{pmatrix} \mathbf{I} & 0 \\ 0 & \mathbf{I} \end{pmatrix}$$

$$\boldsymbol{\sigma}_x = \begin{pmatrix} 0 & 1 \\ 1 & 0 \end{pmatrix} \quad \boldsymbol{\sigma}_y = \begin{pmatrix} 0 & -i \\ i & 0 \end{pmatrix} \quad \boldsymbol{\sigma}_z = \begin{pmatrix} 1 & 0 \\ 0 & -1 \end{pmatrix} \quad \mathbf{I} = \begin{pmatrix} 1 & 0 \\ 0 & 1 \end{pmatrix}$$

$$p = -i\nabla$$

It should be noted that the free electron rest energy in Eq. 2.34 is mc^2, equal to 0.511MeV, while this situation is defined as zero in the non-relativistic case. The zero point of the energy scale is therefore shifted by 5.11×10^5eV, a large amount

compared with the binding energy of 13.6 eV for a hydrogen atom. The two (relativistic and non-relativistic) energy scales may be aligned by subtracting the electron rest energy, which corresponds to replacing the β matrix in Eq. 2.34 by β'.

$$\beta' = \begin{pmatrix} 0 & 0 \\ 0 & 2\mathbf{I} \end{pmatrix}$$

$$[c\boldsymbol{\alpha}\cdot\mathbf{p} + \beta' mc^2 + \mathbf{V}]\Psi = E\Psi \qquad \ldots(2.35)$$

The Dirac equation[80] Eq. 2.35, is four-dimensional, and the relativistic wave function consequently contains four components. Two of the degrees of freedom are accounted for by assigning an intrinsic magnetic moment (spin), while the other two are interpreted as two different particles, electron and positron. The positronic solutions show up as a continuum of "negative" energy states, having energies below $-2mc^2$. It is conventional to write the relativistic wave function as in Eq. 2.36. Here Ψ_L and Ψ_S are the large and small components of the wave function, and α and β indicate the usual spin functions.

$$\Psi = \begin{pmatrix} \Psi_{L\alpha} \\ \Psi_{L\beta} \\ \Psi_{S\alpha} \\ \Psi_{S\beta} \end{pmatrix} \qquad \ldots(2.36)$$

It can be shown[80] that in the non-relativistic limit $c \rightarrow \infty$ and the equation for the large component reduces to the Schrödinger equation (Eq. 2.36) from Eq. 2.37:

$$\left[\frac{1}{2m}(\boldsymbol{\sigma}\cdot\mathbf{p})\mathbf{K}(\boldsymbol{\sigma}\cdot\mathbf{p}) + (\mathbf{V} - E)\right]\Psi_L = 0 \qquad \ldots(2.37)$$

where $$\mathbf{K} = \left(1 + \frac{E - \mathbf{V}}{2mc^2}\right)^{-1}$$

$$\left[\frac{\mathbf{p}^2}{2m} + \mathbf{V}\right]\Psi_L = E\Psi_L \qquad \ldots(2.38)$$

We may obtain relativistic corrections by expanding the K factor in Eq. 2.39, yielding the *Pauli* equation (Eq. 2.41). The first two terms are the usual non-relativistic kinetic

and potential energy operators, the p^2 term is called the mass–velocity correction, and is due to the dependence of the electron mass on the velocity. The next is the spin–orbit term which corresponds to an interaction of the electron spin with the magnetic field generated by the movement of the electron. The last term involving the δ function is the Darwin correction, which corresponds to a correction that can be interpreted as the electron making a high-frequency oscillation around its mean position. The mass–velocity and Darwin corrections are often collectively called the scalar relativistic corrections.

$$\left[\frac{1}{2m}(\boldsymbol{\sigma}\cdot\mathbf{p})\mathbf{K}(\boldsymbol{\sigma}\cdot\mathbf{p})+(\mathbf{V}-E)\right]\Psi_{\mathrm{L}}=0 \qquad \ldots(2.39)$$

$$\mathbf{K}=\left(1+\frac{E-\mathbf{V}}{2mc^2}\right)^{-1}\approx 1-\frac{E-\mathbf{V}}{2mc^2}+\ldots \qquad \ldots(2.40)$$

$$\left[\frac{\mathbf{p}^2}{2m}+\mathbf{V}-\frac{\mathbf{p}^4}{8m^3c^2}+\frac{Z\mathbf{s}\cdot\mathbf{I}}{2m^2c^2r^3}+\frac{Z\pi\delta(\mathbf{r})}{2m^2c^2}\right]\Psi_{\mathrm{L}}=E\Psi_{\mathrm{L}} \qquad \ldots(2.41)$$

Owing to the divergence of the K expansion near the nuclei, the mass–velocity and Darwin corrections can only be used as first-order corrections. Inclusion of such operators in a variational sense will result in a collapse of the wave function. An alternative method is to partition Eq. 2.42 as in Eq. 2.43, which avoids the divergence near the nucleus. In contrast to Eq. 2.44, the factor $E/(2mc^2 - V)$ *is* always much smaller than 1, and *K'* may be expanded in powers of $E/(2mc^2 - V)$, analogously to Eq. 2.44. Keeping only the zeroth-order term (i.e. setting *K' = 1*) gives the Zeroth-Order Regular Approximation equation, Eq. 2.45.[82]

$$(E+2mc^2-\mathbf{V})^{-1}=(2mc^2)^{-1}\left(1+\frac{E-\mathbf{V}}{2mc^2}\right)^{-1}=(2mc^2)^{-1}\mathbf{K} \qquad \ldots(2.42)$$

$$\mathbf{K}=\left(1+\frac{E-\mathbf{V}}{2mc^2}\right)^{-1}$$

$$(E+2mc^2-\mathbf{V})^{-1}=(2mc^2-\mathbf{V})^{-1}\left(1+\frac{E}{2mc^2-\mathbf{V}}\right)^{-1}=(2mc^2-\mathbf{V})^{-1}\mathbf{K}' \qquad \ldots(2.43)$$

$$\mathbf{K}'=\left(1+\frac{E}{2mc^2-\mathbf{V}}\right)^{-1}$$

$$\mathbf{K} = \left(1 + \frac{E - \mathbf{V}}{2mc^2}\right)^{-1} \approx 1 - \frac{E - \mathbf{V}}{2mc^2} + \ldots \qquad \ldots(2.44)$$

$$\left[\frac{c^2\mathbf{p}^2}{2mc^2 - \mathbf{V}} + \frac{2c^2}{(2mc^2 - \mathbf{V})^2} - \frac{Z\mathbf{s}\cdot\mathbf{I}}{r^3} + \mathbf{V}\right]\Psi_L = E\Psi_L \qquad \ldots(2.45)$$

The presence of a magnetic field can be included in the so-called minimal coupling by addition of a vector potential **A** to the momentum operator **p**, forming a generalized momentum operator p, which for an electron is given by Eq. 2.46 The magnetic field is defined as the curl of the vector potential(Eq. 2.47). The **σ·B** term in Eq. 2.48 is called the Zeeman interaction, and represents the interaction of an (external) magnetic field with the intrinsic magnetic moment associated with the electron.

$$\boldsymbol{\pi} = \mathbf{p} + \mathbf{A} \qquad \ldots(2.46)$$

$$\mathbf{B} = \nabla \times \mathbf{A} \qquad \ldots(2.47)$$

$$\left[\frac{\pi^2}{2m} + \mathbf{V} + \frac{\boldsymbol{\sigma}\cdot\mathbf{B}}{2m}\right]\Psi_L = E\Psi_L \qquad \ldots(2.48)$$

For many particle systems it is assumed that each electron can be described by a Dirac operator and the many-electron operator is a sum of such terms, in analogy with the kinetic energy in non-relativistic theory. Furthermore, potential energy operators are added to form a total operator equivalent to the Hamiltonian operator in non-relativistic theory. The Dirac operator incorporates relativistic effects for the kinetic energy. In order to describe atomic and molecular systems, the potential energy operator must also be modified. In non-relativistic theory, the potential energy is given by the Coulomb operator, Eq. 2.49. According to this equation, the interaction between two charged particles depends only on the distance between them, but not on time. This cannot be correct when relativity is considered, as it implies that the attraction/repulsion between two particles occurs instantly over the distance $\boldsymbol{r_{12}}$, violating the fundamental relativistic principle that nothing can move faster than the speed of light. The relativistic interaction requires a description, Quantum ElectroDynamics (QED), which involves exchange of photons between charged particles. The photons travel at the speed of light and carry the information equivalent to the classical Coulomb interaction. The relativistic potential energy operator

becomes complicated and cannot be written in closed form. For actual calculations, it may be expanded in a Taylor series in 1/c and, for chemical purposes, it is normally only necessary to include terms up to $1/c^2$. In this approximation, the potential energy operator for the electron–electron repulsion is given by Eq. 2.50. The gaunt term is a magnetic effect and the Breit term represents a deceleration.

$$\mathbf{V}(\mathbf{r}_{12}) = \frac{q_1 q_2}{r_{12}} \qquad \ldots(2.49)$$

$$\mathbf{V}_{ee}^{\text{Coulomb–Breit}}(\mathbf{r}_{12}) = \frac{1}{r_{12}} - \frac{1}{2r_{12}}\left[\boldsymbol{\alpha}_1 \cdot \boldsymbol{\alpha}_2 + \frac{(\boldsymbol{\alpha}_1 \cdot \mathbf{r}_{12})(\boldsymbol{\alpha}_2 \cdot \mathbf{r}_{12})}{r_{12}^2}\right] \qquad \ldots(2.50)$$

The differences due to relativity can be summarized as:

- Differences in the dynamics due to the velocity-dependent mass of the electron. This alters the size of the orbitals: s- and p-orbitals contract while d- and f-orbitals expand.
- New (magnetic) interactions in the Hamiltonian operator due to electron spin. The spin–orbit coupling, for example, destroys the picture of an orbital having a definite spin.
- Introduction of “negative” energy (positron) states.The coupling between the electronic and positronic states introduces a “small” component in the electronic wavefunction. This leads to a change in the shape of the orbitals: relativistic orbitals, for example, do not have radial nodes(although individual components of the wavefunction have nodes).
- Modification of the potential operator due to the finite speed of light. In the lowest order approximation, this corresponds to addition of the Breit operator to the Coulomb interaction.

The ZORA[82] approach gives generally better results than the Pauli formalism. For all-electron calculations, and in fact also for calculations on very heavy elements (Actinides), the Pauli method is absolutely unreliable.

It should be noted that an approximate inclusion of the scalar relativistic effects, most notably the change in orbital size, can be modelled by replacing the inner electrons

with a relativistic Pseudo-potential or Effective core potential as discussed in Section 2.2.4.

2.4 Beyond static structures at 0 K

As discussed in Sections 2.1-2.2, quantum-chemical calculations are usually based on the Born-Oppenheimer approximation (BOA). The error introduced by the BOA is small in most cases and most often negligible compared to other sources of error. Significant errors are observed only when the BOA breaks down, usually due to the near degeneracy of several coupled electronic states as found for heavy nuclei.[83] In recent years the level of accuracy that can be achieved routinely in quantum-chemical calculations has been significantly improved.[84]

The effects of anharmonicity of vibration become evident in temperature dependant studies of electronic properties, such as NMR chemical shifts in the zero pressure limit. Anharmonicities also shift and split excited vibrational energy levels and cause resonances between them.

Nearly three decades ago, Jameson *et al.*[22a] calculated mean bond M-X displacements in MX_6 type complexes by the L tensor and Bartell methods using anharmonic force fields.

A current focal point is to go beyond the treatment of molecules as vibrationless entities at 0 K and to account for the effect of vibrational averaging of bond-lengths, by perturbational treatments[85] or improved approximations of the Schrödinger equation.[86] Highly accurate studies of ro-vibrational corrections to diatomic molecules have been presented by Sundholm, Gauss and Schafer [86-87]. They presented highly accurate CCSD(T) calculations for the nuclear shieldings of five diatomic molecules, calculating the ro-vibrational corrections numerically.

Various approaches are available to account for the effect of rovibrational averaging in more complex systems. In general one needs a means of generating configurations over which the averages are taken and a means of generating the shielding for a given configuration.

The means of generating configurations may be via a Monte Carlo (MC) process for canonical or grand canonical ensembles or via a MD trajectory. The methods of doing the averaging are (a) in general, to select a series of configurations from MD or MC simulations, do quantum calculations of shielding for those snapshots and take the equally weighted average or (b) to use pre-calculated shielding hypersurfaces and do the averaging during the process of generating the configurations in an MD or MC simulation. The former is a commonly applied method of averaging. In this method, the snapshots are first generated and then the shielding calculation is done for each snapshot. For example, when applied to Xe in benzene solution, the highly anisotropic nature of the interaction between Xe and the benzene molecule makes it difficult to precisely express the set of calculated shielding values for Xe at various positions relative to a benzene molecule into an analytic mathematical form of the Xe shielding hypersurface. Instead, Standara *et al.* [88] carried out classical MD simulations of one Xe atom in a periodic box of benzene molecules and selected snapshots from the classical MD trajectory.

Then the ^{129}Xe shielding was calculated for each snapshot and an arithmetical average is used. This is the most commonly used approach, with many different applications. For example, a supercell was used for liquid water,[89] the periodic simulation box was used in its entirety for Xe dissolved in benzene.[88] A cluster approach was used for ^{1}H shielding in an ionic liquid,[90] and for ^{1}H and ^{13}C shielding of a-D-glucose in water.[91] An embedded cluster approach (EIM) was used for Xe in crystalline clathrate hydrates.[92] An ONIOM approach with QM/MM shells was used for adenine in aqueous solution,[93] a hybrid QM/MM was used by Sebastiani *et al.* for liquid water.[94] Clusters containing various numbers of water molecules solvating anionic Pt complexes were used for ^{195}Pt shielding in tetrahaloplatinate(II) complex and hexahaloplatinate(IV) complexes.[95] For convergence, the number of configurations sampled from the ab initio MD trajectories was 128, and the number of solvating molecules needed in the cluster calculation (using ZORA DFT) for convergence of the average shielding was 12 for the smaller tetrachloroplatinate(II) complex, while 14 seem to be required for the larger corresponding bromo complex. Both octahedral hexachloroplatinate (IV) and hexabromoplatinate (IV) complexes required less (about 8 water molecules). The modelling of these effects by averaging chemical shifts over trajectories from classical molecular dynamics (MD) simulations is a common approach,[41, 96] partly because these simulations can readily be extended to explicitly

include the solvent, which is by far the most important effect when calculating subtle electronic properties of transition-metal complexes.

The generalized procedure for zero-point corrections devised by Ruud *et al.* and later implemented by Barone, consisted of two parts. First, effective geometries, r_g^0 at 0 K that were constructed in a perturbational approach from the equilibrium geometries r_e, the (mass-dependent) harmonic frequencies ω_e, and the cubic force field $V^{(3)}$[97]:

$$r_{e,j} + \Delta r_{g,j}^{0} = r_{e,j} - \frac{1}{4\omega_{e,j}^{2}} \sum_{m} \frac{V_{e,jmm}^{(3)}}{\omega_{e,m}} \qquad \ldots(2.51)$$

The term r_g^0 is the vibrationally averaged geometry at 0 K and is synonymous to r_{eff}. In principle, this is the observed geometry at 0 K, while at finite temperatures, the occupancy of vibrational energy levels above ground state will be governed by a Boltzmann distribution and r_g values would be observed instead.

Next, shieldings are calculated at this point, with a correction from the (numerically evaluated) shielding hypersurface around r_g^0. This procedure has been applied extensively in maingroup inorganic and organic chemistry. The first DFT calculations of rovibrationally averaged magnetic shielding constants of transition metal nuclei have been done by Bühl *et al.*[85b], where it was found that corrections from the shielding hypersurface were negligible and σ_{eff}, the shielding calculated at r_g^0, is sufficient. This perturbational approach was used in this study even though MD simulations would appear practical, it seems all but impossible at this time to converge the simulations to such a numerical precision that would allow extraction of classical thermal isotope effects of the small magnitude required for our purposes.

2.5 Calculating NMR nuclear shielding with DFT

Nuclei with half integral spin, I are NMR active and have 2I+1 nuclear energy levels. In the presence of an external magnetic field, the degeneracy of these energy levels is lifted, allowing spectroscopic techniques to be applied. The resonance frequency is defined as:

$$\upsilon = \frac{\gamma B_0}{2\pi}(1-\sigma) \qquad \ldots(2.52)$$

where υ is the resonance frequency, γ the gyromagnetic ratio of the nucleus, B_0 the applied magnetic field and σ the shielding. The shielding results in the effective magnetic field at the nucleus to be different than the applied field. In NMR experiments, the resonance frequency is thus dependent on both the applied field and the shielding. Since the interest lies in using the magnetic resonance as a probe to chemical properties, the shift in resonance frequency is reported relative to a reference compound resulting in field-independent chemical shifts, δ.

The experimental chemical shift, δ, is therefore directly related to the shielding:

$$\delta = \frac{\upsilon_{sample} - \upsilon_{ref}}{\upsilon_{ref}} \times 10^6 = \frac{\sigma_{ref} - \sigma_{sample}}{1 - \sigma_{ref}} \approx \sigma_{ref} - \sigma_{sample} \qquad \ldots(2.53)$$

The last approximation seen in the Eq. 2.53 can be made because σ_{ref} is usually very small compared to unity.

From a non-relativistic quantum mechanical perspective, the shielding, or the magnetic shielding tensor σ_{ij}^N of a nucleus *N*, is the mixed second derivative of the total molecular energy *E* with respect to the magnetic moment μ^N and the external magnetic field B:[40]

$$\sigma_{ij}^N = \left(\frac{\delta^2 \mathrm{E}}{\delta \mathrm{B}_i \delta \mu_j^N} \right)_{\mathbf{B}, \mu^N = 0} \qquad \ldots(2.54)$$

Computationally, the shielding is usually calculated as a sum of diamagnetic and paramagnetic contributions:[62]

$$\sigma_{ij} = \sigma_{ij}^{(d)} + \sigma_{ij}^{(p)}$$

$$\sigma_{ij}^{(d)} = \frac{\alpha^2}{2} \sum_{\mu\upsilon} \mathrm{P}_{\mu\upsilon} \left\langle \varphi_\mu \middle| r_A^{-3} \left[\boldsymbol{r}_A \boldsymbol{r} - \boldsymbol{r}_{Ak} \boldsymbol{r}_l \right] \middle| \varphi_\upsilon \right\rangle$$

$$\sigma_{ij}^{(p)} = \frac{\alpha^2}{2} \sum_{\mu\upsilon} \frac{\delta \mathrm{P}_{\mu\upsilon}}{\delta B_k} \left\langle \varphi_\mu \middle| \left(-i\nabla \times (\boldsymbol{r} - \boldsymbol{R}_A) \right)_l r_A^{-3} \middle| \varphi_\upsilon \right\rangle \qquad \ldots(2.55)$$

It is the paramagnetic part $\sigma_{ij}^{(p)}$ is slightly troublesome to compute as it involves the derivative of the density matrix. This necessitates the use of the coupled-perturbed

SCF equations making chemical shift calculations more expensive than most other properties.[62]

A further complication arises because the magnetic operators involved depend on the origin of the coordinate system leading to artificial origin-dependent results. This is called the gauge problem. If a complete basis set is used, the results will be independent of the chosen origin, which is of course never the case in practice. Different ways of dealing with this gauge-dependency have been proposed, the most satisfactory solution probably being the use of magnetic-field dependent basis sets, the so called gauge-including atomic orbitals method (GIAO). [98,99] With this method, the basis functions are made magnetic-field dependent by multiplying them by a phase factor referring to the position of the nucleus:[40]

$$\tilde{\varphi}_{\mu}(\chi, \mathbf{B}) = \varphi_{\mu}^{A} \exp\left(i\left(\frac{\alpha}{2}\right)(\mathbf{B} \times \mathbf{R}_{\mathbf{A}})\mathbf{r}\right) \qquad \ldots(2.56)$$

The shielding is, due to its mixed second derivative form, an unsymmetrical tensor with 3 x 3 different elements.

$$\sigma = \begin{vmatrix} \sigma_{xx} & \sigma_{xy} & \sigma_{xz} \\ \sigma_{yx} & \sigma_{yy} & \sigma_{yz} \\ \sigma_{zx} & \sigma_{zy} & \sigma_{zz} \end{vmatrix} \qquad \ldots(2.57)$$

The matrix can be split up into a symmetric part and an antisymmetric part. The antisymmetric part typically does not influence NMR spectra and is thus not of interest. The symmetric part of the tensor, $\sigma^{sym} = \frac{1}{2}(\sigma + \sigma^{t})$, where σ^{t} is the transpose of σ,can be diagonalised if expressed in the principal axis system, giving three orthogonal eigenvectors and three eigenvalues, σ_{11}, σ_{22} and σ_{33} that describe the position and shape of the NMR signal (ignoring ***J*** coupling quadrupole coupling and other effects). The eigenvectors describe the orientation of the tensor components in space.[100] The average of the eigenvalues is the isotropic shielding, $\sigma_{iso} = \frac{1}{3}(\sigma_{11} + \sigma_{22} + \sigma_{33})$. In isotropic media such as liquid solutions, only this average is observable.

The isotropic chemical shift, δ_{iso}, of a nucleus in a molecule is evaluated by taking the difference in the isotropic shielding between it and the nucleus in an accepted reference molecule (usually the one that defines the origin of the chemical shift scale).

$$\delta_{iso} = \sigma_{ref} - \sigma_{iso} \qquad \ldots(2.58)$$

Computational chemical shifts are hence evaluated in an analogous way to NMR experiments. By simulating thermal and solvent effects, the accuracy of theoretical transition-metal shifts can be improved. Further improvement can be achieved by including relativistic effects as discussed under Section 2.3.

Chapter 3

Computational Details

3.1 Geometries

Geometries were fully optimised using at the PBE0/ECP1 level, i.e. employing the hybrid variant of the PBE functional,[101] the Stuttgart-Dresden relativistic effective core potential (SDD ECP) along with its [6s5p3d] valence basis on Pt, [102]and 6-31G* basis[75b, 76] elsewhere. This combination of functional and basis sets has performed very well for the description of bond distances between third-row transition metals and their ligands.[103] Preliminary performance tests of selected other functional/ECP combinations are summarized in Table 3.1 and a graphical representation is shown in Figure 3.1. Unless otherwise noted, tight optimization criteria and a fine integration grid were employed (opt=tight, grid=finegrid options in Gaussian). Selected complexes were reoptimized using the same ECP and basis sets in conjunction with the LDA,[66b] B3LYP,[68, 71] B3PW91[66c, 71, 104] and M06 functionals, as well as (at the PBE0/ECP1 level) with the CPCM method,[105] the equivalent of the conductor-like screening model (COSMO), as implemented in Gaussian 09, together with the parameters of water.

Effective geometries, $r_g^{\,0}$ at 0 K, were constructed in a perturbational approach from the equilibrium geometries r_e, the (mass-dependent) harmonic frequencies ω_e, and the cubic force field $V^{(3)}$.[97]

$$r_{g,j}^{\;0} = r_{e,j} + \Delta r_{g,j}^{\;0} = r_{e,j} - \frac{1}{4\omega_{e,j}^2} \sum_m \frac{V^{(3)}_{e,jmm}}{\omega_{e,m}} \qquad \ldots(3.1)$$

These calculations were performed using the Gaussian09 suite of programs.[106]

Table 3.1*:* Vibrationally averaged bond lengths at 0K for $[PtCl_6]^{2-}$ calculated at various levels of theory[a] employing default grids and step sizes [in Å].

	$Pt^{35}Cl_6^{2-}$				$Pt^{37}Cl_6^{2-}$		
	r_e	r_g^0	$r_e - r_{exp}$[b]	$r_g^0 - r_e$	r_g^0	$r_g^0 - r_e$	$^{35}r_g^0 - ^{37}r_g^0$
LDA/SDD,6-31G*	2.344226	2.347903	0.025226	0.003677	2.347816	0.003590	0.000087
LDA/LANL2DZ, 6-31G*	2.362115	2.365614	0.043115	0.003499	2.365524	0.003409	0.000090
LDA/SDD,6-311+G**	2.348670	2.352426	0.029670	0.003756	2.352274	0.003604	0.000152
LDA/LANL2DZ, 6-311+G**	2.362575	2.366104	0.043575	0.003529	2.366068	0.003493	0.000036
B3LYP/SDD,6-31G*	2.408177	2.412191	0.089177	0.004014	2.412088	0.003911	0.000103
B3LYP/LANL2DZ, 6-31G*	2.425203	2.429132	0.106203	0.003929	2.429030	0.003827	0.000102
B3LYP/SDD, 6-311+G**	2.411551	2.415938	0.092551	0.004387	2.415485	0.003934	0.000453
B3LYP/LANL2DZ, 6-311+G**	2.425835	2.429787	0.106835	0.003952	2.429685	0.003850	0.000102
PBE0/SDD,6-31G*	2.370495	2.374272	0.051495	0.003777	2.374175	0.003680	0.000097
PBE0/LANL2DZ, 6-31G*	2.386278	2.389948	0.067278	0.003670	2.389852	0.003574	0.000096
PBE0/SDD,6-311+G**	2.371480	2.375535	0.052480	0.004055	2.375155	0.003675	0.000380
PBE0/LANL2DZ, 6-311+G**	2.385429	2.389109	0.066429	0.003680	2.389015	0.003586	0.000094
B3PW91/SDD,6-31G*	2.382956	2.386856	0.063956	0.003900	2.386756	0.003800	0.000100
B3PW91/LANL2DZ, 6-31G*	2.399122	2.402903	0.080122	0.003781	2.402806	0.003684	0.000097
B3PW91/SDD, 6-311+G**	2.384108	2.388299	0.065108	0.004191	2.387898	0.003790	0.000401
B3PW91/LANL2DZ, 6-311+G**	2.398117	2.401906	0.079117	0.003789	2.401809	0.003692	0.000097
M06/SDD,6-31G*	2.392186	2.398119	0.073186	0.005933	2.397697	0.005511	0.000422
M06/LANL2DZ, 6-31G*	2.406061	2.411824	0.087061	0.005763	2.411680	0.005619	0.000144
M06/SDD,6-311+G**	2.393517	2.399464	0.074517	0.005947	2.399133	0.005616	0.000331
M06/LANL2DZ, 6-311+G**	2.405736	2.411524	0.086736	0.005788	2.411380	0.005644	0.000144

[a]LANL2DZ denotes the Hay-Wadt ECP with its double-zeta basis (Hay P. J.; Wadt, W. R. *J. Chem. Phys.* **1985**, *82*, 299). [b]r_{exp} taken from: D. Steinborn, O. Gravenhorst, H. Hartung, U. Baumeister, *Inorg. Chem.* **1997**, *36*, 2195.

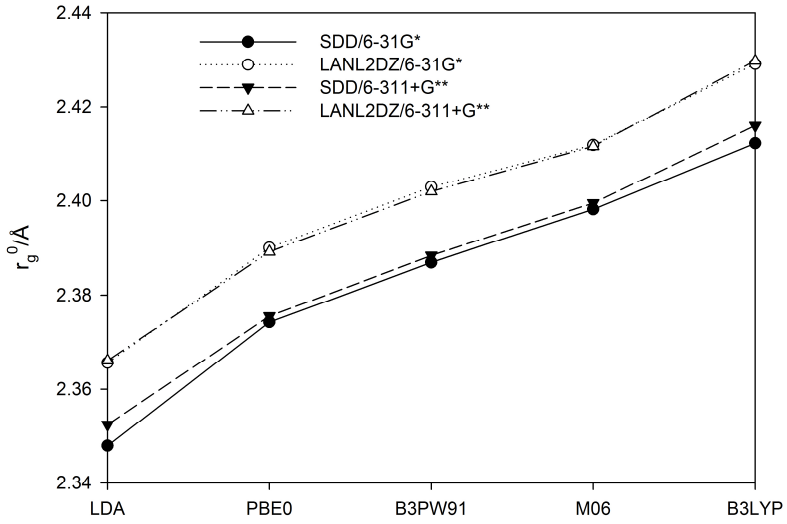

Figure 3.1: Vibrationally averaged bond length at 0 K, r_g^0, for $[Pt^{35}Cl_6]^{2-}$ determined at different levels of theory in the gas phase (SDD and LANL2DZ denoting Stuttgart-Dresden and Hay-Wadt effective core potentials (ECPs), respectively); see Table 3.1 for numerical data.

Except for LDA (which is deprecated for its tendency to overbind), PBE0/SDD/6-31G* affords the best accord with the observed mean Pt-Cl distance in the solid, *ca*. 2.369 Å.[107] and was chosen as the level of optimization in the present work.

3.2 NMR shielding tensors

For r_e and r_g^0 geometries of each isotopic substitution, ^{195}Pt and ^{103}Rh shielding tensors were computed at the relativistic spin-orbit ZORA level, using the GGA PW91[66c, 104] functional, together with an all-electron quadruple-ζ plus polarization function (QZ4P) basis set on Pt and Rh and polarized valence triple-ζ basis sets (TZP) on Cl and H_2O. The integration precision parameter was set to 10.0. These calculations employed the ADF2010.02 program.[108]

This level of theory performed well for the calculation of chemical shifts for various heavy metal complexes. For example, Autschbach *et al.* [6] reported ^{295}Pt and ^{205}Tl NMR chemical shifts of the complexes $[(NC)_5Pt—Tl(CN)n]^{n-}$ n=0–3, and of the related system $[(NC)_5Pt—Tl—Pt(CN)_5]^{3-}$ calculated at this level. Koch *et al.*[4] reported reasonably accurate ^{195}Pt chemical shifts of a series of octahedral $[PtX_{6-n}Yn]^{2-}$ complexes for X = Cl, Br, F, I .

Although $\delta(^{103}Rh)$ can be calculated at a non-relativistic level[79], for consistency with the ^{195}Pt chemical shift calculations, ZORA-SO is also applied, which has been shown to work well for ^{103}Rh[109].

Chapter 4

On the origin of $^{35/37}$Cl and $^{16/18}$O isotope effects on ^{195}Pt NMR nuclear shielding of $[Pt^{35/37}Cl_n(H_2O)_{6-n}]^{n-2}$ complexes

4.1 Introduction

^{195}Pt NMR spectroscopy has long been used to characterize diamagnetic Pt complexes, fuelled by the additional interest in Pt-containing drugs and catalytic applications, an immense body of Pt NMR data is available.[1b, 1c] As mentioned in Chapter 1, the ^{195}Pt nucleus can be so sensitive to its environment that rather subtle isotope effects can be detected.[2, 17]

It is the aim of this thesis to compute such isotope shifts from first principles, in order to provide a solid theoretical framework for the empirical observations, and to have a means of assignment in cases where the statistical distribution would be ambiguous. Quantum-chemical computation of transition-metal chemical shifts is a stronghold of density-functional theory (DFT),[23] and the advent of relativistic methods such as the zero-order regular approximation (ZORA) have made ^{195}Pt NMR parameters amenable to computational study. [6, 24]

Most of these calculations employ static equilibrium structures, which are independent of atomic masses. Using zero-point vibrationally averaged structures, isotope effects on ^{59}Co chemical shifts have been reproduced and rationalized computationally. [58] In a cobaloxime[58a] and the hexamine cobalt(III) complex, [58b] the observed ^{1}H/^{2}H shifts on the order of ca. 50 ppm - 100 ppm could be traced back to small changes in the Co-N bonds, on the order of 0.001 Å- 0.006 Å, upon isotopic substitution. Because of their much smaller magnitude, typically 1 ppm or less, [59] the abovementioned isotope effects on ^{195}Pt shifts pose a much bigger challenge to theory.

In this Chapter, a DFT study of the $^{35/37}$Cl and $^{16/18}$O induced isotope shifts in the ^{195}Pt NMR spectra of some prototypical Pt(IV) chlorido/aqua complexes,

$[PtCl_{6-n}(H_2O)_n]^{n-2}$ (n=0-3) is presented. The complexes were chosen with the anticipation of minimized solvation effects due to small charges i.e. -1, 0 and +1.

4.2 Results and Discussion

4.2.1 Numerical Stability

From the observed isotope shift between $[Pt^{35}Cl_6]^{2-}$ and $[Pt^{37}Cl_6]^{2-}$, $\Delta\delta(^{195}Pt) \approx 1$ ppm,[17] and the computed shielding/bond-length derivative of $[PtCl_6]^{2-}$, $\partial\sigma^{Pt}/\partial r_{PtCl}$ = –18,300 ppm/Å (ZORA/PW91/TZP/COSMO level),[4] it can be estimated that the changes in bond lengths brought about by the isotopic substitution should be on the order of ca. $6\cdot10^{-5}$ Å. Such small effects place quite stringent demands not only on the accuracy of the methods to be applied, but also on the numerical stability of the zero-point corrections evaluated through eq. 3.1. Because the cubic force field $V^{(3)}$ is obtained through numerical differentiation of analytical second derivatives, it must be made sure that the numerical noise introduced this way is not larger than the actual effects under scrutiny. Besides the step size involved in the creation of the displaced structures, the most important parameter is the size of the grid involved in the numerical integration of the exchange-correlation potential for energies and second derivatives (in the coupled perturbed Kohn-Sham equations). We have used pristine *cis*-$PtCl_4(H_2O)_2$ (**2**, Figure 4.1) as test molecule, gauging convergence of the results from the computed effects of vibrational averaging on the Pt-Cl distances in the all-^{35}Cl and all-^{37}Cl isotopomers (Tables 4.1 and 4.3).

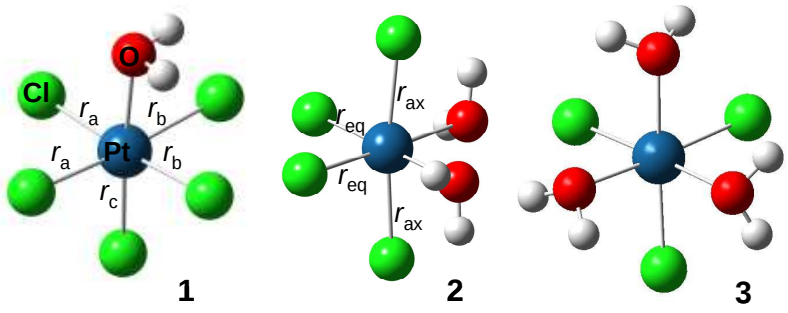

Figure 4.1: Optimized structures of $[PtCl_5(H_2O)]^-$ (**1**, left), *cis*-$PtCl_4(H_2O)_2$ (**2**, middle) and *fac*-$[PtCl_3(H_2O)_3]^+$ (**3**, right).

Table 4.1: Equilibrium bond lengths (r_e) and differences between equilibrium and effective bond lengths at 0K (Δr_{eq} and Δr_{ax}) in *cis*-$Pt^{35}Cl_4(H_2O)_2$ [Å], obtained with different grids and step lengths d [a.u.] in the numerical integration and differentiation, respectively.[a]

Grids[b]	r_e[c]		d = 0.1		d =0.01		d =0.001		CPU
	$r_{e,eq}$	$r_{e,ax}$	$\Delta r_{g,eq}{}^0$	$\Delta r_{g,ax}{}^0$	$\Delta r_{g,eq}{}^0$	$\Delta r_{g,ax}{}^0$	$\Delta r_{g,eq}{}^0$	$\Delta r_{g,ax}{}^0$	hours[d]
B/A	2.272205(0)	2.336298(4)	0.002444	0.005812	0.002356	0.005873	0.002355	0.005871	10.5
C/B	2.275561(0)	2.337360(2)	0.002313	0.003060	0.002251	0.003028	0.002250	0.003026	11.5
D/C	2.275548(0)	2.337465(1)	0.002418	0.003111	0.002379	0.003094	0.002378	0.003082	27.0
E/D	2.275536(1)	2.337448(1)	0.002437	0.003109	0.002401	0.003095	0.002401	0.003092	63.0

[a]PBE0/SDD/6-31G* level. [b]Numerical integration grids involved in energy/CPKS evaluations, labeled A (35,110), B (50,194), C (75, 302), D (99,590), E (99,770) (numbers in parentheses: radial and angular gridpoints, respectively). [c]Average value of the two axial r_{ax} and two equatorial bonds r_{eq} (in parentheses: standard deviation in units of the last digit, calculated from differences in results for formally equivalent bonds). [d]Approximate runtime on 8 CPUs of a local Opteron PC cluster.

Although the minimum turned out to possess C_2 symmetry, the calculations were done without imposing this. The differences in results for formally equivalent bonds can thus be a further probe for numerical stability.

Table 4.1 summarizes the equilibrium distances r_e and their changes $\Delta r_g{}^0$ upon inclusion of the zero-point vibrational corrections as a function of grid and step sizes in the numerical integration and differentiation steps involved. Ideally the results should converge smoothly with increasing grids and decreasing stepsize, i.e. going down and to the right in the table. The default setting in Gaussian is to use fine and coarse grids in the evaluation of energies and the solution of the coupled perturbed Kohn-Sham (CPKS) equations, respectively (C/A combination in the labeling of Table 4.1), together with a step size of 0.01 a.u. Even with the slightly better fine/SG1 grid combination (C/B) the results are not sufficiently converged, however: Further increase in grid quality (i.e. going from C/B to D/C) affects the equilibrium distances and the vibrational corrections by up to 10^{-4} Å, that is, above the desired accuracy.

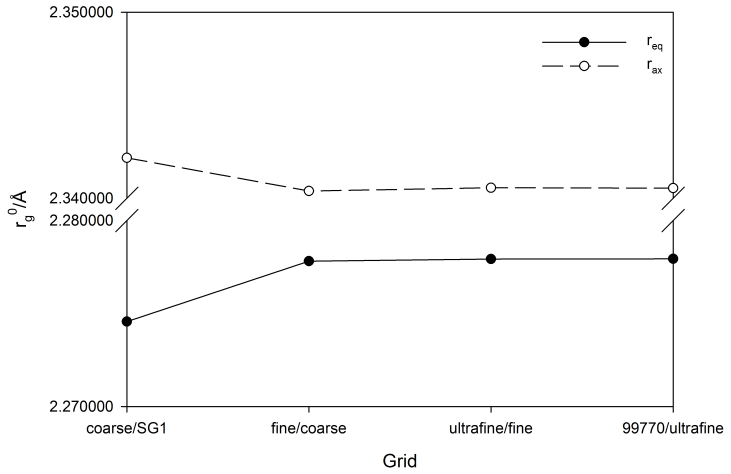

Figure 4.2: Vibrationally averaged bondlength, r_g^0 for *cis*-$Pt^{35}Cl_4(H_2O)_2$ as a function of numerical integration grids of increasing quality.

Further improvement of the grid (e.g. from D/C to E/D) results in only minor changes, $2 \cdot 10^{-5}$ Å or less (see Figure 4.2 for a graphical representation). Reassuringly, the vibrational corrections are only faintly sensitive to the step size (compare Δr as function of d in Table 4.1), in contrast to some first-row transition metal complexes, where this parameter proved to be important for the numerical stability.[85b] We note in passing that the overall magnitude of the zero-point corrections for the Pt-Cl bonds, on the order of ca. 0.2 Å - 0.3 Å, is very similar to that obtained for other 5d-metal chlorides. [103]

The same test calculations were carried out for the *cis*-$Pt^{37}Cl_4(H_2O)_2$ isotopologue. The resulting differences in the vibrational corrections between the ^{35}Cl and ^{37}Cl complexes (i.e. between the corresponding r_g^0 values) are summarized in Table 4.2 (note that these $\Delta\Delta r$ values are now reported in units of 10^{-5} Å; for the actual distances in the ^{37}Cl isotopomer see Table 4.3). As expected from the effect of anharmonicity, Pt-^{35}Cl bonds are longer than Pt-^{37}Cl bonds. Even though these isotope effects are now relative trends rather than absolute values, little error compensation is to be expected, because we are assessing numerical precision, not accuracy. Nonetheless, the same convergence pattern as for the vibrational corrections in Table 4.1 is apparent, and the largest change between any $\Delta\Delta^{35/37}r$ value on going from the D/C to the E/D grids is $2.8 \cdot 10^{-5}$ Å. Taking the computational expense into account (last column in Table 4.1), the ultrafine/fine grid combination (D/C) and the

default step size of 0.01 a.u. appeared to be the best compromise between precision and speed and was adopted for all further calculations.

Table 4.2: Differences $\Delta\Delta^{35/37}r$ between effective Pt-Cl distances in *cis*-$Pt^{35}Cl_4(H_2O)_2$ and *cis*-$Pt^{37}Cl_4(H_2O)_2$ in units of 10^{-5} Å, obtained with different grids and step lengths d [a.u.] in the numerical integration and differentiation, respectively.[a]

Grids[b]	d = 0.1		d =0.01		d =0.001	
	$\Delta\Delta^{35/37}r_{eq}$	$\Delta\Delta^{35/37}r_{ax}$	$\Delta\Delta^{35/37}r_{eq}$	$\Delta\Delta^{35/37}r_{ax}$	$\Delta\Delta^{35/37}r_{eq}$	$\Delta\Delta^{35/37}r_{ax}$
B/A	26.8	9.4	28.7	8.2	28.7	8.2
C/B	9.1	9.5	8.7	9.0	8.7	9.1
D/C	9.9	14.5	10.0	14.5	9.9	13.7
E/D	10.3	11.8	10.3	11.7	10.3	11.9

[a,b]See Table 4.1.

Table 4.3: Vibrationally averaged bond lengths at 0K (r_{eq} and r_{ax}) in cis-$Pt^{37}Cl_4(H_2O)_2$ [Å] and difference (Δr_{eq} and Δr_{ax}) with the cis-$Pt^{35}Cl_4(H_2O)_2$ isotopologue in units of the last digit[10^{-6} Å], obtained with different step lengths [a.u.] in the numerical differentiation (average value of the two axial r_{ax} and two equatorial bonds r_{eq}; in parentheses: standard deviation in units of the last digit). All data were calculated at the PBE0/SDD/6-31G* level with several grids of increasing quality.

Grid energy/CPHF	**Stepsize**											
	0.1				**0.01**				**0.001**			
	$\mathbf{r_{eq}}$	$\mathbf{r_{ax}}$	$\mathbf{^{35}r\text{-}^{37}r}$		$\mathbf{r_{eq}}$	$\mathbf{r_{ax}}$	$\mathbf{^{35}r\text{-}^{37}r}$		$\mathbf{r_{eq}}$	$\mathbf{r_{ax}}$	$\mathbf{^{35}r\text{-}^{37}r}$	
			$\mathbf{\Delta r_{eq}}$	$\mathbf{\Delta r_{ax}}$			$\mathbf{\Delta r_{eq}}$	$\mathbf{\Delta r_{ax}}$			$\mathbf{\Delta r_{eq}}$	$\mathbf{\Delta r_{ax}}$
coarse/SG1	2.274381(5)	2.342016(16)	268	94	2.274274(5)	2.342089(12)	287	82	2.274273(5)	2.342087(12)	287	82
fine/coarse	2.277783(3)	2.340325(1)	91	95	2.277725(4)	2.340298(1)	87	90	2.277724(3)	2.340294(1)	87	91
ultrafine/fine	2.277867(1)	2.340431(0)	99	145	2.277827(3)	2.340413(0)	100	145	2.277827(1)	2.340409(0)	99	137
99770/ultrafine	2.277871(2)	2.340439(1)	103	118	2.277834(2)	2.340425(1)	103	117	2.277833(1)	2.340421(1)	103	119

4.2.2 Geometries

The optimized structures of complexes **(1)-(3)** are shown in Figure 4.1. It is well known that the trans influence is prevalent among Pt(IV) and Pt(II) complexes.[110] This influence of a ligand on the bond trans to it can be seen when looking at the values in Table 4.4-4.6. Pt-Cl bonds trans to a coordinated H_2O are shorter as indicated by XRD measurements, shown in Table 4.5. This is mainly due to the larger trans influence of Cl^- relative to H_2O. The *cis*-$PtCl_4(H_2O)_2$ isomer is found as a stable crystal as shown by the XRD data in Table 4.5 and the possibility of separate isotopomers for the singly and triply substituted species (e.g. B and C in Figure 4.3 and 4.4 middle) would make the trans form an unlikely candidate for the experimentally observed spectrum. The Pt-^{35}Cl are longer than Pt-^{37}Cl bonds, as expected from the effect of anharmonicity. A similar trend is found for Pt-O bonds in Table 4.6 where the Pt-^{16}O bond extends further in space than the corresponding Pt-^{18}O bond.

Table 4.5: Equilibrium bond lengths r_e, differences between effective and equilibrium bond lengths Δr_{eff} (= Δr_g^0) and differences between effective bond distances for $[Pt^{35/37}Cl_6]^{2-}$, $[Pt^{35/37}Cl_5(H_2O)]^-$ and cis-$Pt^{35/37}Cl_4(H_2O)_2$ [in Å] calculated at the PBE0/SDD/6-31G* level. r^a, r^b etc. correspond to the labelling of the bonds in Figure 4.1 (for **2**, r^a and r^b correspond to r_{eq} and r_{ax}, respectively).

	r_e^a	r_e^b	r_e^c	$\Delta^{35}r_{eff}^a$	$\Delta^{35}r_{eff}^b$	$\Delta^{35}r_{eff}^c$	$\Delta^{37}r_{eff}^a$	$\Delta^{37}r_{eff}^b$	$\Delta^{37}r_{eff}^c$	$r_{eff}^{35\,a} - r_{eff}^{37\,a}$	$r_{eff}^{35\,b} - r_{eff}^{37\,b}$	$r_{eff}^{35\,c} - r_{eff}^{37\,c}$	$^{35}r_{w_{eff}} - {}^{37}r_{w_{eff}}$
$[PtCl_6]^{2-}$	2.3700			0.0043			0.0042			0.000097			
$[PtCl_5(H_2O)]^-$	2.3358	2.3730	2.2807	0.003741	0.003575	0.002539	0.003739	0.003421	0.002473	0.000002	0.000154	0.000066	-0.000020
Exp.[a]	2.3063	2.3163	2.2732										
***cis*-$PtCl_4(H_2O)_2$**	2.2755	2.3375		0.0024	0.0031		0.0023	0.0029		0.00010	0.00015		-0.1334
Exp.[b]	2.2644	2.3153											

Table 4.6: Equilibrium bond lengths r_e, differences between effective and equilibrium bond lengths Δr_{eff} and differences between effective bond distances for $[Pt^{35}Cl_5(H_2{}^{16/18}O)]^-$ and cis-$Pt^{35}Cl_4(H_2{}^{16/18}O)_2$ [in Å]] calculated at the PBE0/SDD/6-31G* level.

	r_e	$^{18}r_g^0$	$^{16}r_g^0$	$\Delta^{18}r_{eff}$	$\Delta^{16}r_{eff}$	$\Delta^{16}r_{eff} - {}^{18}\Delta r_{eff}$
$[PtCl_5(H_2O)]^-$	2.156201	2.166175	2.166823	0.009974	0.010622	0.000648
Exp.[a]	2.0610					
$PtCl_4(H_2O)_2$	2.132479	2.141841	2.142381	0.009362	0.009902	0.000540
$PtCl_4(^{18}OH_2)(^{16}OH_2)$	2.132479	2.141693	2.142337	0.009214	0.009858	0.000644
Exp.[b]	2.0447					

[a]From D. Steinborn, O. Gravenhorst, H. Hartung, U. Baumeister, *Inorg. Chem.* **1997**, *36*, 2195. [b] C.Wagner, C.Bruhn, O.Gravenhorst, D.Steinborn, Z.Kristallogr. **2000**,215, 61.

4.2.3 Isotope shifts

Subsequently, all possible $^{35/37}$Cl isotopomers were calculated in the gas phase for a representative set of mixed Pt(VI) chloro/aquo complexes (**1 - 3**, see Figure 4.1), namely $[Pt^{35}Cl_n{}^{37}Cl_{5-n}(H_2O)]^-$ (n = 0 - 5), *cis*-$Pt^{35}Cl_n{}^{37}Cl_{4-n}(H_2O)_2$ (n = 0 - 4), and *fac*-$[Pt^{35}Cl_n{}^{37}Cl_{(3-n)}(H_2O)_3]^+$ (n=0-3). The resulting vibrationally averaged structures were used as inputs for relativistic calculations of the isotropic magnetic shielding constants at the ZORA-SO/PW91/QZ4P/TZ2P level. To compare with experiment, isotope shifts $\Delta\delta$ were calculated relative to the corresponding all-^{35}Cl isotopologue set to $\delta = 0$.

Because the water molecules coordinate in a bent, "sp^3" mode, the symmetry of the isolated complexes in the gas phase is lower than that apparent on the NMR time scale, i.e. C_s instead of C_{4v} for **1**, C_2 instead of C_{2v} for **2**, and C_3 instead of C_{3v} for **3**. While this does not affect the number of possible isotopomers for **2** and **3**, for **1** there are many more static structures than experimentally resolved signals. However, many of the static structures can be interconverted through simple water rotation about the Pt-O bond or inversion at O, processes that are expected to occur very rapidly on the NMR time scale. It is thus reasonable to assume that those isotopomers of **1** that are grouped together in Figure 4.3 will only show a single NMR signal, and their computed shielding constants were averaged accordingly. A more detailed study is shown under Section 5.2.2.

The resulting shielding constants and the corresponding experimental isotope shifts are collected in Table 4.7 and, after conversion of the computed shieldings into relative shifts, plotted against each other in Figure 4.4. The sign of the experimental isotope shifts has been reversed, so that they appear in the same sequence as in a conventional NMR spectrum.

Table 4.7a: Experimental[2] ^{195}Pt chemical shifts and computed isotropic shielding constants for the isotopomers and isotopologues of **1** and **2**.

	cis-[$Pt^{35/37}Cl_4(H_2{}^{16}O)_2$]		[$Pt^{35/37}Cl_5(H_2{}^{16}O)$]$^-$		[$Pt^{35/37}Cl_5(H_2{}^{18}O)$]		cis-[$Pt^{35/37}Cl_4(H_2{}^{18}O)_2$]		cis-[$Pt^{35/37}Cl_4(H_2{}^{16}O)$ ($H_2{}^{18}O$)]	
	δ_{exp}/ppm	σ_{calc}/ppm	δ_{exp}/ppm	σ_{calc}/ppm	δ_{exp}/ppm	σ_{calc}/ppm	δ_{exp}/ppm	σ_{calc}/ppm	δ_{exp}/ppm	σ_{calc}/ppm
A	995.95	1763.62	487.16	1794.54	486.47	1794.47	976.10	1766.83	976.76	1765.28
B	995.80	1763.96	487.01	1795.19	486.31	1794.83	975.95	1766.96	976.62	1765.43
C	995.73	1763.77	486.94	1795.09	486.24	1795.42	975.89	1766.86	976.55	1765.96
D	995.65	1763.60	486.84	1795.24	486.15	1795.00	975.80	1767.00	976.47	1765.57
E	995.58	1764.01	486.84	1795.43	486.15	1795.44	975.74	1766.50	976.40	1766.11
F	995.51	1764.29	486.78	1795.53	486.08	1795.76	975.67	1766.73	976.33	1765.99
G	995.44	1764.14	486.69	1795.43	485.99	1795.21	975.60	1766.79	976.27	1766.11
H	995.37	1764.38	486.62	1795.39	485.91	1795.88	975.51	1766.95	976.19	1766.14
I	995.22	1764.61	486.62	1795.62	485.91	1796.25	975.39	1767.20	976.08	1766.21
J			486.51	1795.63	485.76	1795.51				
K			486.45	1795.86	485.67	1796.30				
L			486.34	1795.71	485.58	1796.33				

Table 4.7b: Experimental[2] ^{195}Pt chemical shifts and computed isotropic shielding constants for the isotopomers and isotopologues of **3**.

	fac-[$Pt^{35/37}Cl_3(H_2{}^{16}O)_3$]		fac-[$Pt^{35/37}Cl_3(H_2{}^{16}O)_2(H_2{}^{18}O)$]		fac-[$Pt^{35/37}Cl_3(H_2{}^{16}O)$ ($H_2{}^{18}O$)$_2$]		fac-[$Pt^{35/37}Cl_3(H_2{}^{18}O)_3$]	
	δ_{exp}/ppm	σ_{calc}/ppm	δ_{exp}/ppm	σ_{calc}/ppm	δ_{exp}/ppm	σ_{calc}/ppm	δ_{exp}/ppm	σ_{calc}/ppm
A	1484.05	1482.47	1483.40	1483.74	1482.77	1485.60	1482.11	1486.25
B	1483.85	1482.99	1483.20	1485.03	1482.56	1485.17	1481.93	1485.90
C	1483.65	1483.46	1483.01	1485.61	1482.35	1484.85	1481.71	1485.47
D	1483.43	1483.77	1482.80	1485.90	1482.21	1485.02	1481.52	1486.00

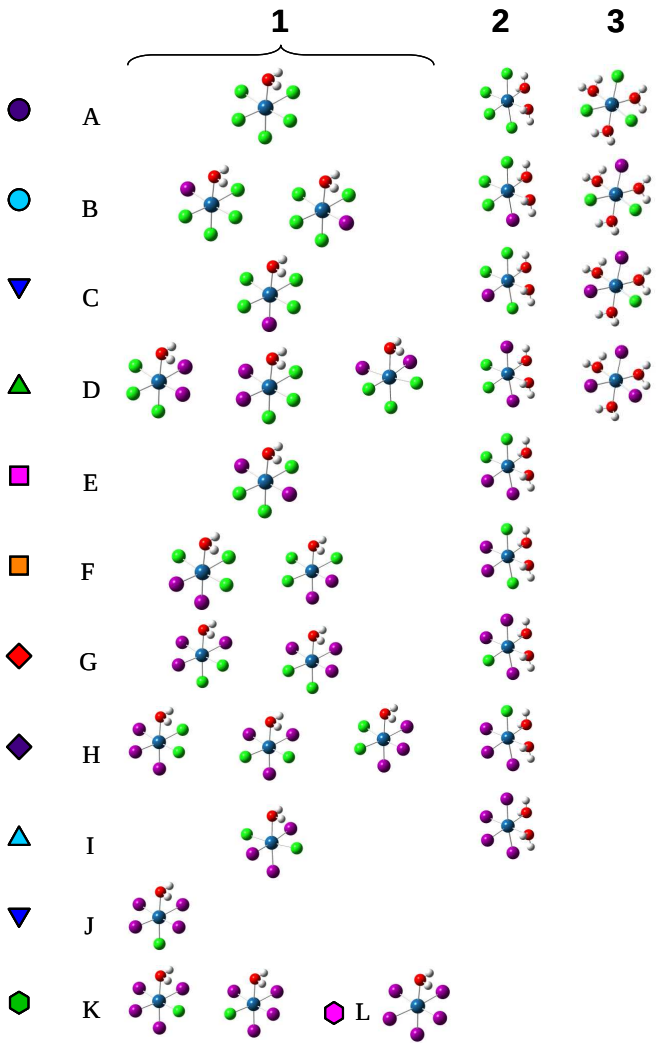

Figure 4.3: Isotopomers of $[PtCl_5(H_2O)]^-$ (**1**), *cis*-$PtCl_4(H_2O)_2$ (**2**), and fac-$[PtCl_3(H_2O)_3]^+$ (**3**), together with the labelling scheme adopted in the following figures; color code: ^{35}Cl green, ^{37}Cl purple.

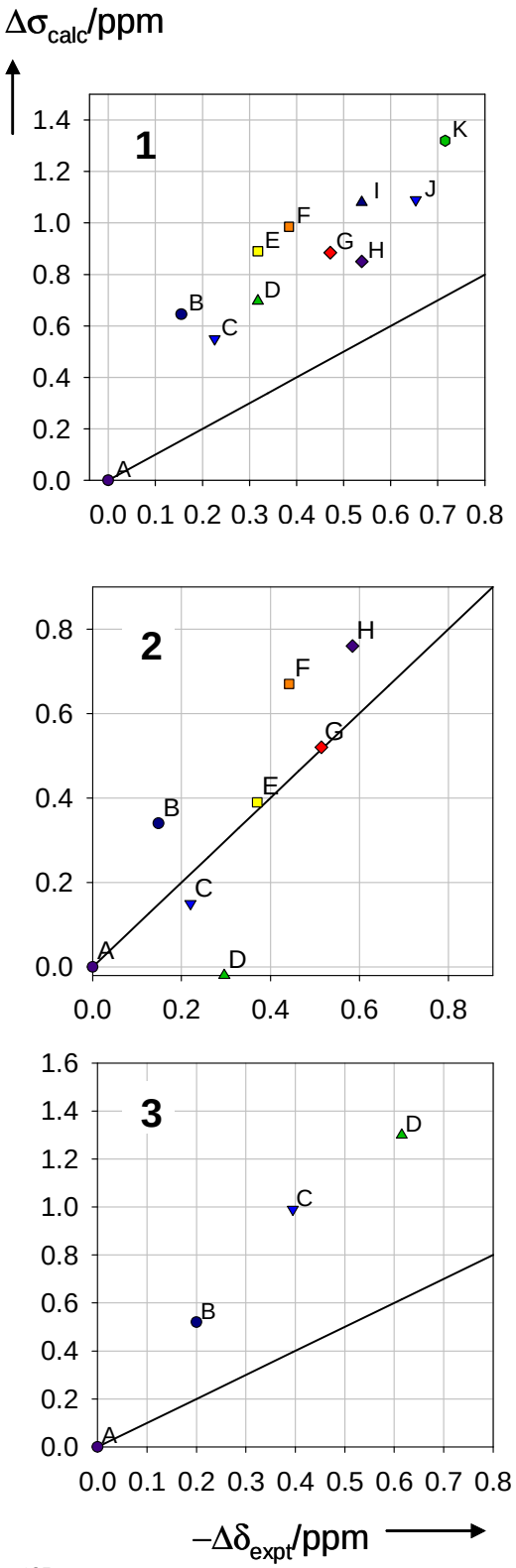

Figure 4.4 Calculated ^{195}Pt shielding differences vs. negative experimental $^{35/37}$Cl isotope shifts of the isotopomers of **1 - 3** in Figure 4.3, including the ideal line with unity slope; top: $[PtCl_5(H_2O)]^-$, middle: *cis*-$PtCl_4(H_2O)_2$, bottom: *fac*-$[PtCl_3(H_2O)_3]^+$.

Despite some scatter, the overall observed trends are reasonably well reproduced by our computational protocol. It is particularly gratifying that the overall order of

magnitude of the isotope shifts, ca. 1 ppm, is rather well recovered computationally. Only the isotope shifts of **(3)** appear to be overestimated by a factor of *ca.* 2. The sequence of individual, more closely spaced resonances (below *ca.* 0.2 ppm) is not always reproduced correctly, however. It is unclear at present whether these discrepancies are due to residual numerical errors in the computations, deficiencies of the overall model (e.g. the neglect of thermal effects beyond the zero-point corrections), or missing solvation (see below).

These minor inaccuracies notwithstanding, our results can be seen as first theoretical rationalization of the observed isotope effects. ^{195}Pt NMR thus can effectively resolve chemical shift differences between complexes whose metal-ligand distances vary on the femtometer scale (cf. Table 4.2, 1 fm = 10^{-5} Å), a truly remarkable resolution.

As commonly found for heavy-atom chemical shifts, it is the paramagnetic contribution to the shielding tensor, σ_{para}, that appear to dominate the overall observed ^{195}Pt shielding trends. The other contributions, namely the diamagnetic and spin-orbit terms, are rather insensitive to the isotopic substitution. This finding is illustrated in Table 4.8 and Figure 4.5 for the isotopomers of **2**. Generally, trends in heavy atom chemical shifts are rationalized through the orbital rotation model.[111] Localized orbital-based analyses of computed NMR shielding tensors provide intuitive and chemically meaningful contributions to the chemical shifts of heavy nuclei, but this was not attempted for the small effects under scrutiny in this study.

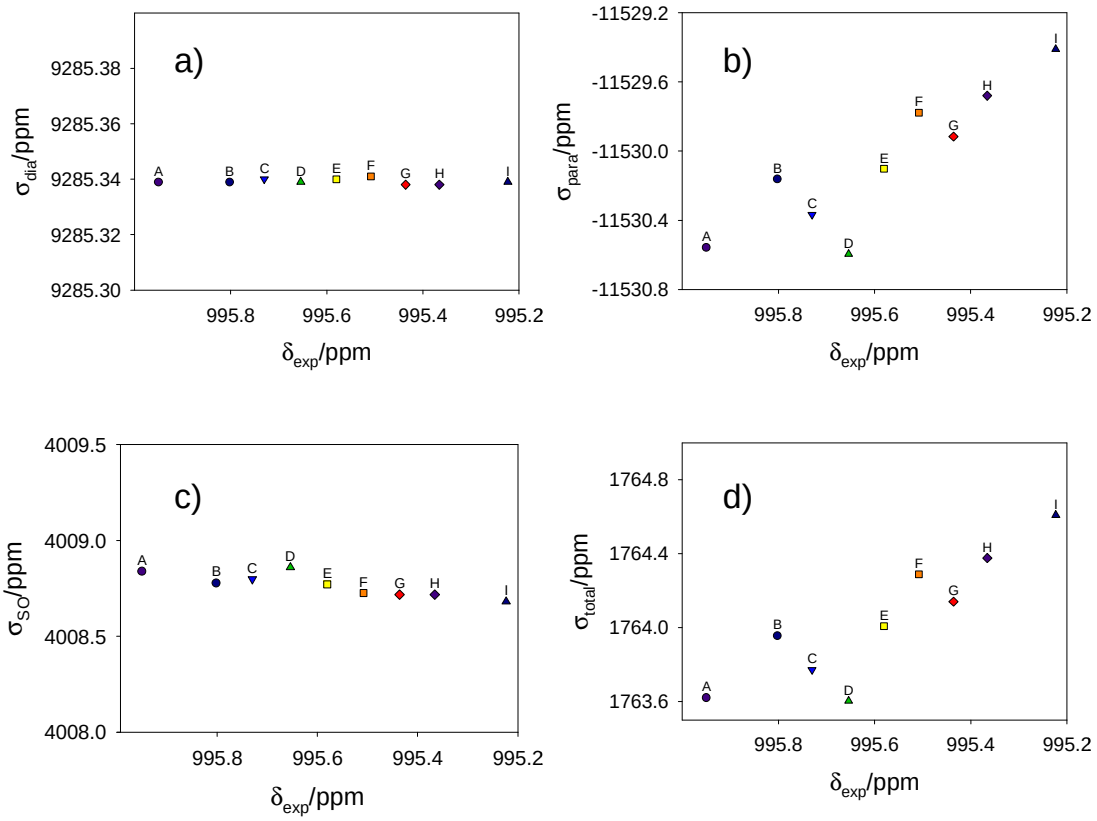

Figure 4.5: (a) Diamagnetic, (b) paramagnetic, (c) spin-orbit and (d) total shielding tensors plotted against experimental chemical shifts of the isotopologues/isotopomers of cis-$[Pt^{35/37}Cl_4(H_2O)_2]$. Note that the total shieldings are dominated by the paramagnetic contributions.

Table 4.8: Breakdown of calculated total shielding constants σ_{tot} into their constituents for *cis*-$[Pt^{35}Cl_4(H_2O)_2]$ isotopomers. For a plot vs. δ_{exp} see Figure 4.5.

	$^{35/37}$Cl *trans* to H_2O	Pt(IV) isotopologue/isotopomer	σ_{para}/ppm	σ_{dia}/ppm	σ_{SO}/ppm	σ_{tot}/ppm	δ_{exp}/ppm
A	^{35}Cl,^{35}Cl	*cis*-$[Pt^{35}Cl_4(H_2O)_2]$	-11530.6	9285.339	4008.839	1763.621	995.9502
B	^{35}Cl,^{35}Cl	*cis*-$[Pt^{35}Cl_3{}^{37}Cl(H_2O)_2]$	-11530.2	9285.339	4008.778	1763.956	995.8022
C	^{35}Cl,^{37}Cl		-11530.4	9285.340	4008.798	1763.771	995.7301
D	^{35}Cl,^{35}Cl	*cis*-$[Pt^{35}Cl_2{}^{37}Cl_2(H_2O)_2]$	-11530.6	9285.339	4008.859	1763.603	995.6542
E	^{35}Cl,^{37}Cl		-11530.1	9285.340	4008.770	1764.008	995.5801
F	^{37}Cl,^{37}Cl		-11529.8	9285.341	4008.725	1764.288	995.5080
G	^{35}Cl,^{37}Cl	*cis*-$[Pt^{35}Cl^{37}Cl_3(H_2O)_2]$	-11529.9	9285.338	4008.717	1764.140	995.4359
H	^{37}Cl,^{37}Cl		-11529.7	9285.338	4008.717	1764.376	995.3657
I	^{37}Cl,^{37}Cl	*cis*-$[Pt^{37}Cl_4(H_2O)_2]$	-11529.4	9285.339	4008.681	1764.608	995.2234

It has been observed that when ^{18}O-enriched water is used as solvent, the characteristic ^{195}Pt fingerprints from the $^{35/37}$Cl substitution patterns are split into two more sets of signals, which are ascribed to $H_2{}^{16/18}O$ isotopologues and isotopomers.

The computed $^{35/37}$Cl isotope shifts for these ^{18}O isotopomers are plotted against experiment in Figure 4.6. The same patterns as for the parent ^{16}O complexes (Figure 4.4) were expected, as found experimentally. However, noticeably different results were obtained.

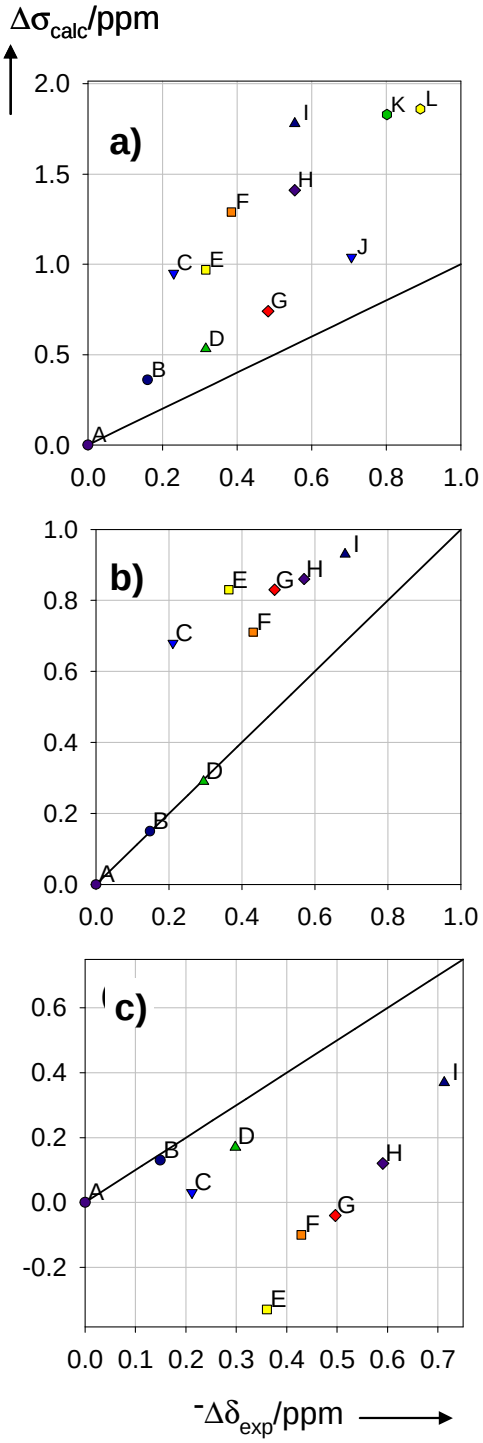

Figure 4.6 Calculated shielding differences vs. negative experimental $^{35/37}$Cl isotope shifts of the isotopomers of Figure 4.3, including the ideal line with unity slope. a) $[PtCl_5(H_2{}^{18}O)]^-$; b) *cis*-$PtCl_4(H_2{}^{16}O)(H_2{}^{18}O)$; c) *cis*-$PtCl_4(H_2{}^{18}O)_2$.

For instance, on going from $[Pt^{35/37}Cl_5(H_2{}^{16}O)]^-$ to $[Pt^{35/37}Cl)_5(H_2{}^{18}O)]^-$, the agreement with experiment deteriorates visibly (compare top of Figures 4.4 and 4.6a). The same is found for *cis*-$Pt^{35/37}Cl_4(H_2{}^{16}O)_2$ upon replacement of one or both water ligands with $H_2{}^{18}O$ (i.e. going from the middle of Figure 4.6 via 4.6b to 4.6c), as well as for *fac*-$[Pt^{35/37}Cl_3(H_2O^{16/18})_3]^+$ (see Figure 4.7).

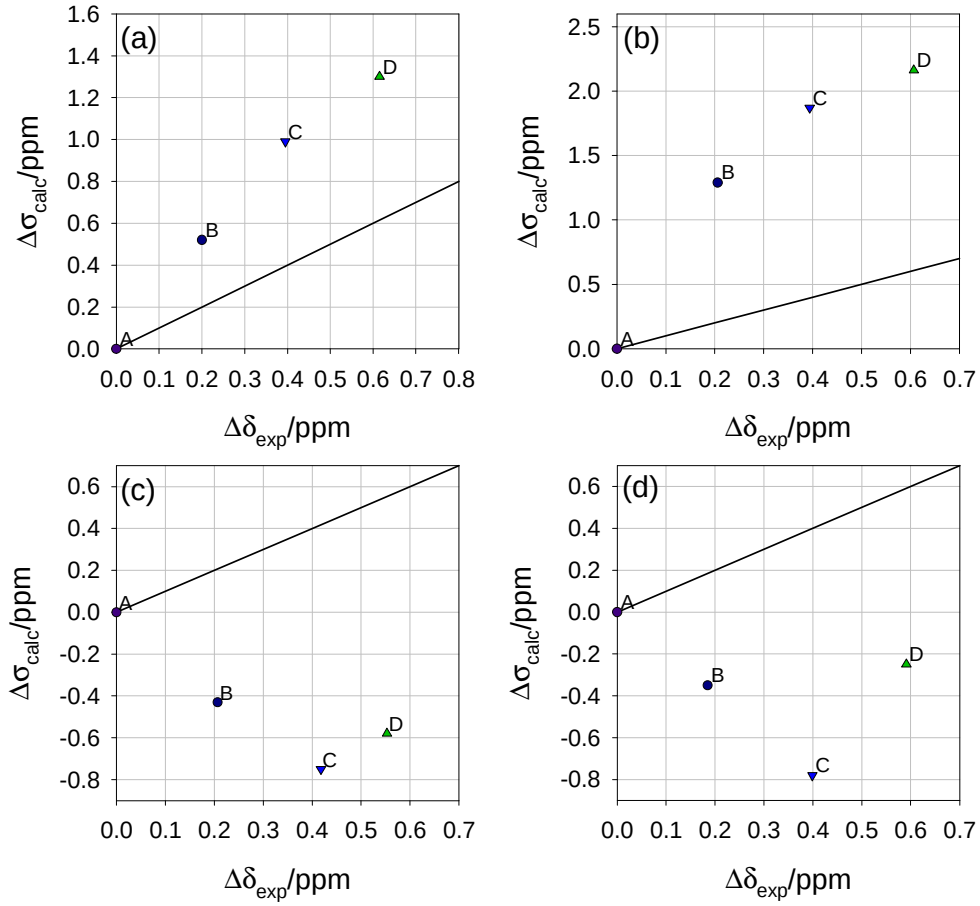

Figure 4.7: Calculated shielding differences vs. negative experimental $^{35/37}$Cl isotope shifts of the isotopomers of **3**, including the ideal line with unity slope. a) *fac*-$[PtCl_3(H_2{}^{16}O)_3]^+$ (same as bottom of Figure 3) b) *fac*-$[PtCl_3(H_2{}^{16}O)_2(H_2{}^{18}O)]^+$; c) *fac*-$[PtCl_3(H_2{}^{16}O)(H_2{}^{18}O)_2]^+$; d) *fac*-$[PtCl_3(H_2{}^{18}O)_3]^+$.

It appears that the sensitivity of the Pt-O bond length toward isotopic substitution is not very well captured by the present approach: e.g. for $[Pt^{35/37}Cl_5(H_2O)]^-$, substitution of ^{16}O for ^{18}O in each isotopomer affords a rather constant upfield shift of $\Delta\delta(^{195}Pt) \approx 0.7 \pm 0.05$ ppm. The variation in the computed $\Delta\sigma$ values is much larger and rather unsystematic, ranging from $\Delta\sigma \approx +0.8$ ppm to ≈ -0.5 ppm (see Figure 4.8).

The origin of this large discrepancy is not fully clear at present, but there are reasons to assume that solvation effects, so far neglected in our approach, can be decisive. In

many computational studies of transition-metal aquo complexes it has been found that the M-OH_2 distances can decrease appreciably on going from the gas phase into an aqueous solution.[112] In fact, remarkably large vibrational corrections $\Delta r_g^0 \approx 0.01$ Å are obtained for the Pt-O bonds in the gas phase (Table 4.4), indicative of rather anharmonic, shallow stretching potentials.

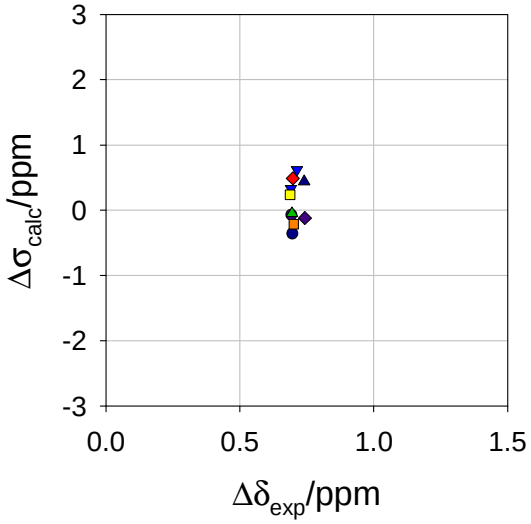

Figure 4.8: Plot of difference between calculated σ values of $[Pt^{35/37}Cl_5(H_2{}^{16}O)]^-$ and $[Pt^{35/37}Cl_5(H_2{}^{18}O)]^-$ vs. the corresponding difference between the experimental δ values.

When comparing the rather constant experimental differences between $[Pt^{35/37}Cl_5(H_2{}^{16}O)]^-$ and $[Pt^{35/37}Cl_5(H_2{}^{18}O)]^-$ to the corresponding calculated shielding values, the plot in Fig 4.8 is obtained. All the data points should have the same coordinates in the case of perfect agreement, however, the calculated shielding have a unsystematic deviation indicating that the model is unreliable in this case.

4.2.4 Shielding/bond-length derivatives

How closely can the isotope shifts be linked to the variations in bond distances? To address this question, we used three representative shielding/bond-length derivatives $\partial\sigma_{Pt}/\partial r_{PtX}$ (X = O and Cl), together with the computed zero-point corrections for each bond length (Δr_g^0 in eq 1), in order to estimate effective shieldings according to:

$$\sigma^0_{g,est} = \sigma_e + \sum_{i=1}^{6} \Delta r^0_{g,i} \frac{\partial \sigma_{Pt}}{\partial r_{PtX,i}} \qquad \ldots(4.1)$$

These estimated shieldings can then be compared to the actual effective shieldings computed for the actual vibrationally averaged structure. Pt-Cl and Pt-O shielding/bond-length derivatives have been evaluated for **(1)** – **(3)**, respectively, by rigid scans of the Pt-Cl and Pt-O bonds about their equilibrium values (see Figure 4.9 for **(2)**).

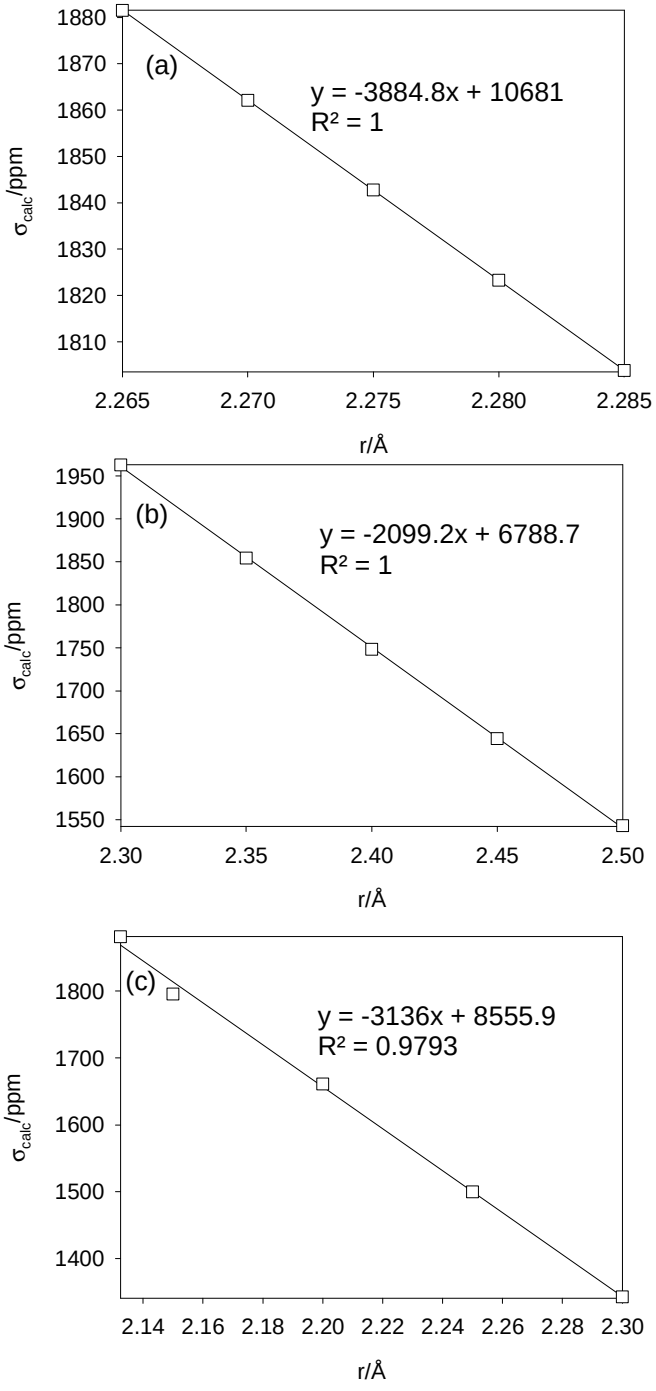

Figure 4.9: Plot of ^{195}Pt magnetic shielding of *cis*-$PtCl_4(H_2O)_2$ vs. (a) Pt-Cl_{eq}, (b) Pt-Cl_{ax} and (c) Pt-O bond distances, evaluated at the ZORA-SO/PW91 level.

Table 4.9: Shielding/bond-length derivatives $\partial\sigma_{Pt}/\partial r_{PtX}$ computed[a] for complexes **1 - 3** at the ZORA-SO/PW91 level.

Compd.	Bond[b]	$\partial\sigma_{Pt}/\partial r_{PtX}$ [ppm/Å]
1	Pt-O	-3167
	Pt-Cl_a	-2770
	Pt-Cl_b	-2529
	Pt-Cl_c[c]	-4240
2	Pt-O	-3136
	Pt-Cl_{ax}	-2099
	Pt-Cl_{eq}[c]	-3885
3	Pt-O	-1869
	Pt-Cl[c]	-2548

[a]Obtained through rigid displacements of the ligands about the equilibrium value of the designated bond, see Figure 4.9 for an example. [b]See Figure 4.1 for definition. [c]trans to water ligand

The resulting $\partial\sigma_{Pt}/\partial r_{PtX}$ values are remarkably different for the different bonds, ranging from ca. −2100ppm/Å to ca. −4200 ppm/Å for Pt-Cl bonds, and from ca. −1900 ppm/Å to ca. −3200 ppm/Å for Pt-O bonds. The Pt-Cl bonds trans to a chloride have smaller $\partial\sigma_{Pt}/\partial r_{PtX}$ values compared to that of the Pt-Cl bond in $[PtCl_6]^{2-}$, -3276 ppm/Å. Jameson [22a] reported $\partial\sigma_{Pt}/\partial r_{PtX}$ values estimated from measured isotope shifts as -4300 ppm/Å for $[PtCl_6]^{2-}$. Although, large errors were inherent in her estimations, it is indicative of the order of magnitude of $\partial\sigma_{Pt}/\partial r_{PtX}$.

These $\partial\sigma_{Pt}/\partial r_{PtX,i}$ values were subsequently used to evaluate the increments to $\sigma^0_{g,est}$ from the $r^0_{g,i}$ values in **(1) – (3)** for each bond *i* (using the appropriate $\partial\sigma_{Pt}/\partial r_{PtX,i}$ value from Table 4.9). Figure 4 shows the resulting estimated $^{37/35}$Cl isotope effects on the ^{195}Pt shieldings of **1**-**3**, plotted vs. the actual computed values (cf. Figure 4.10). Both span and sequence of the $\Delta\sigma$ values are described rather well by the increment method. This result substantiates our underlying model, namely that the bond length changes due to zero-point vibrations is the dominant factor influencing the isotope shifts. This is concordant with similar interpretations for zero-point corrections to transition-metal chemical shifts[113] themselves (i.e. not isotope shifts).

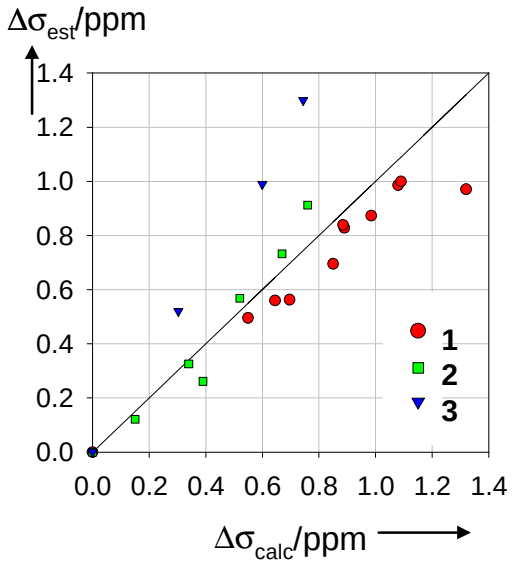

Figure 4.10 Shielding differences in $^{35/37}$Cl isotopomers of **1** - **3**, estimated from Eq. 4.1 vs. actual computation from r_g^0 geometries, including the line with unity slope.

4.2.5 Solvation effects

The simple polarizable continuum model (PCM) was used to evaluate isotope effects on the Pt aquo complexes in solution. The suitability of PCM in zero-point corrections has been successfully used to model ^{59}Co chemical shifts in aqueous solution[58a], however, $\delta(^{59}\text{Co})$ varied over 10,000 ppm. As discussed in Section 4.2.1, we are aiming at much smaller effects, where numerical stability can become an issue. In this context, PCM methods pose an additional problem during construction of the molecular cavity, which is built from interlocking spheres around the atoms. These spheres are discretized into triangular tesserae, which may lead to additional numerical uncertainties in the evaluation of $V^{(3)}$ in Eq. 3.1 via finite displacements. In principle, results should converge with increasing number of surface discretization points (see Figure 4.11 for selected three-dimensional plots of the latter), but in practice this becomes difficult because of the increasing CPU time and program limitations. In fact, the highest density of discretization points that could be used in conjunction with the vibrational averaging scheme in Gaussian09, 86 points/Å^2, is not sufficient to converge even the equilibrium distances to the desired precision, much less the zero-point corrections to them (see Table 4.10 and Figure 4.12). For cis-$Pt^{35/37}Cl_4(H_2O)_2$, increasing the number of discretization point or integration grids can

affect the $\Delta\Delta^{35/37}r$ values by up to $9.4 \cdot 10^{-5}$ Å (Table 4.10), i.e. above the desired target precision (cf. Section 4.2.1). If $^{35/37}$Cl isotope shifts are calculated for all isotopomers of **2** nonetheless, a seemingly reasonable correlation with experiment is obtained, but the computed span of shifts, 25 ppm, is more than one order of magnitude larger than observed (Figure 4.13). Clearly, simple continuum models are not suitable with our protocol for such small isotope shifts.

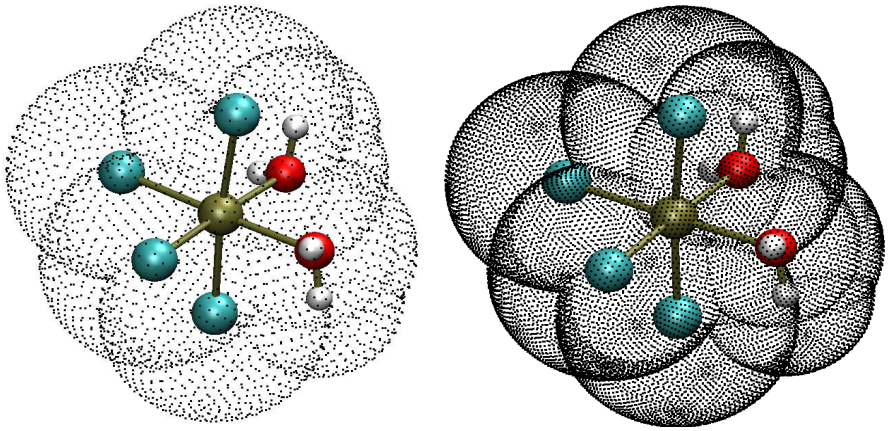

Figure 4.11: Surface discretization points defining the cavity in CPCM calculations for *cis*-$PtCl_4(H_2O)_2$; average densities in points/Å^2: left 14, right 86.

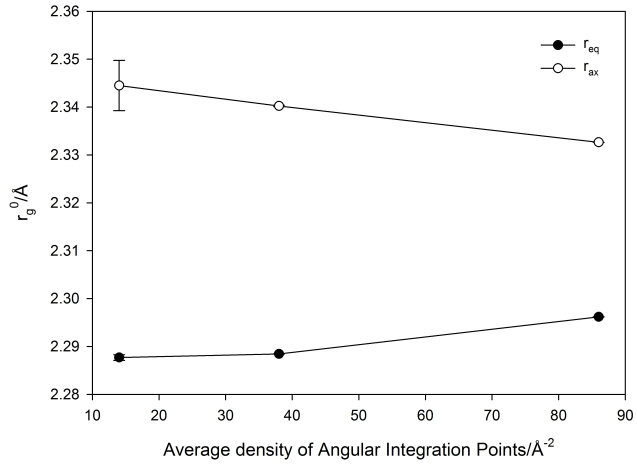

Figure 4.12: Vibrationally averaged bond lengths in *cis*-$Pt^{35}Cl_4(H_2O)_2$ as a function of surface descretization (the error bar denoting the standard deviation in the two formally equivalent bonds). Note that the bond lengths are not yet properly converged.

Table 4.10: Vibrationally averaged bond lengths at 0K (r_{eq} and r_{ax}) in *cis*-$Pt^{35}Cl_4(H_2O)_2$ [Å] and difference (Δr_{eq} and Δr_{ax}) with the *cis*-$Pt^{37}Cl_4(H_2O)_2$ isotopologue in units of the last digit, obtained with different surface-discretization point densities [$Å^{-2}$][a] (average value of the two axial r_{ax} and two equatorial bonds r_{eq}; in parentheses: standard deviation in units of the last digit). All data were calculated at the CPCM/PBE0/SDD/6-31G* level with several grids of increasing quality and a step size of 0.01 a.u. in the numerical differentiation.

Grid energy/CPHF	**Average density of surface discretization points[a]**											
	14 [3777]				**38 [9066]**				**86 [19668]**			
	$\mathbf{r_{eq}}$	$\mathbf{r_{ax}}$	$\mathbf{^{35}r\text{-}^{37}r}$		$\mathbf{r_{eq}}$	$\mathbf{r_{ax}}$	$\mathbf{^{35}r\text{-}^{37}r}$		$\mathbf{r_{eq}}$	$\mathbf{r_{ax}}$	$\mathbf{^{35}r\text{-}^{37}r}$	
			$\mathbf{\Delta r_{eq}}$	$\mathbf{\Delta r_{ax}}$			$\mathbf{\Delta r_{eq}}$	$\mathbf{\Delta r_{ax}}$			$\mathbf{\Delta r_{eq}}$	$\mathbf{\Delta r_{ax}}$
fine/coarse	2.286605(12)	2.344057(3)	204	116	2.283760(68)	2.3437885(417)	113	98	2.283681(10)	2.351955(112)	32	323
ultrafine/fine	2.291957(2)	2.343058(7)	1	116	2.288239(47)	2.3395875(65)	78	173	2.294762(139)	2.333146(162)	80	103
99770/ultrafine	2.287693(592)	2.344502(5251)	67	112	2.288440(36)	2.3402425(138)	100	204	2.296184(17)	2.332641(2)	174	66

[a] Pdens keyword in Gaussian (default value:5) [in brackets: total number of points].

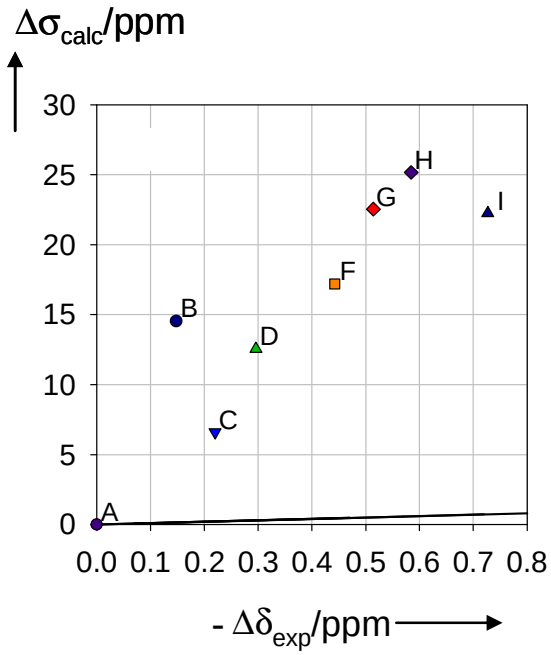

Figure 4.13: Calculated shielding differences vs. negative experimental $^{35/37}$Cl isotope shifts of the isotopomers of *cis*-$PtCl_4(H_2O)_2$ in a polarizable continuum, including the ideal line with unity slope (CPCM/PBE0/SDD/6-31G* level with ultrafine/fine grids). Note how the observed span is overestimated by more than an order of magnitude.

As a first step toward such a full description of solvation, we have optimized a microsolvated cluster, namely $[PtCl_5(H_2O)]^-\cdot 2H_2O$. Placing the two extra water molecules such that they each accepts an $OH\cdots OH_2$ hydrogen bond from the coordinated water ligand, the minimum shown on top of Figure 4.14 is obtained.

On going from pristine **1** to $[PtCl_5(H_2O)]^-\cdot 2H_2O$, the equilibrium Pt-O bond distance decreases from 2.156 Å to 2.112 Å, similar to what is found in a continuum (e.g. 2.118 Å for **1**). At the same time, the zero-point correction for the Pt-^{16}O distance changes from Δr_g^0 = 0.011 Å (Table 4.6) to 0.008 Å upon microsolvation, consistent with a stronger, stiffer bond.

How does this apparent change in the Pt-O stretching potential affect the isotope effects? The computed $^{35/37}$Cl shifts of all isotopomers are plotted against experiment in Figure 4.14. Comparing these plots to those of the pristine complex **1** (i.e. Figure 4.14a and top of Figure 4.4 for the ^{16}O isotopomers, and Figures 4.14b and 4.6a for the ^{18}O counterparts) shows no visible improvement upon solvation. There are

significant changes throughout, however, suggesting that solvent effects can indeed be very important.

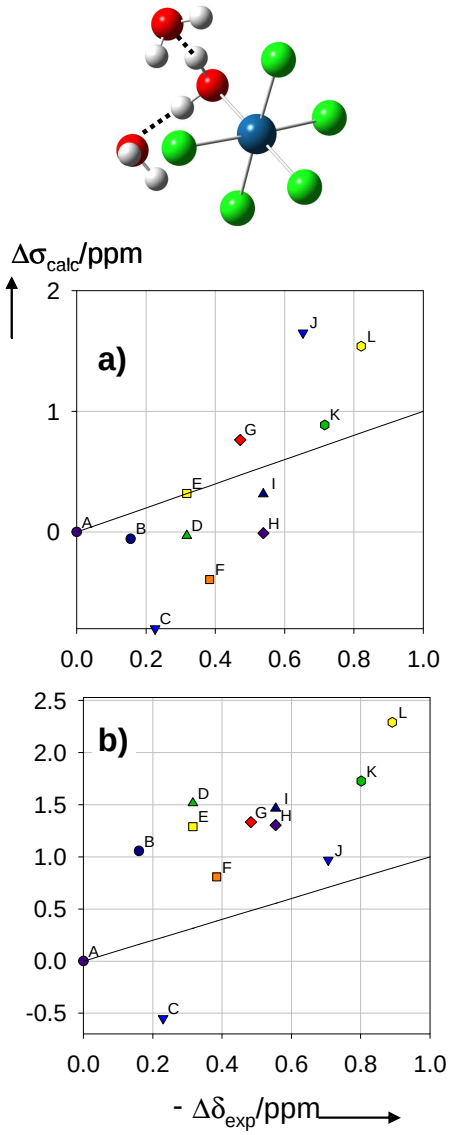

Figure 4.14 Calculated shielding differences vs. negative experimental $^{35/37}$Cl isotope shifts of the isotopomers of $[PtCl_5(H_2O)]^-\cdot 2H_2O$ (shown at the top, labeling as in Figure 4.3), including the ideal line with unity slope. a) $[PtCl_5(H_2{}^{16}O)]^-\cdot 2H_2{}^{16}O$; b) $[PtCl_5(H_2{}^{18}O)]^-\cdot 2H_2{}^{16}O$.

Figure 4.14a seems to contain two rather distinct series of data points, where isotopomers C, F, H, I, K and L form a linear correlation on their own (albeit with a much too large slope, ca. 4 instead of 1, and a significant offset from the ideal line). Interestingly, these are all the isotopomers that have a ^{37}Cl atom *trans* to the water ligand (Figure 4.3). Apparently, in our microsolvated complex the distinction between

cis and *trans* chloride ligands is overestimated to a large extent, consistent with the fact that only the former interact with the extra water molecules, not the latter. To accurately model the solvent, more waters must be added; eventually a MD description would be necessary, which is beyond the scope of this study.

The shielding/bond-length derivatives up until now were determined in the gas-phase. How would they be different in the continuum? To address this question, shielding/bond-length derivatives have been evaluated in the polarized continuum for **(2)**, by rigid scans of the Pt-Cl and Pt-O bonds about their equilibrium values as shown in Figure 4.15. The resulting $\partial\sigma_{Pt}/\partial r_{PtX}$ values are not much different from what was found in the gas-phase. Immersion in a polarized continuum, increased $\partial\sigma_{Pt}/\partial r_{PtX}$ for Pt-Cl_{eq} from -3885 to −4069 ppm/Å, Pt-Cl_{ax} from -2099 to −2370 ppm/Å. Interestingly, the Pt-O bonds remained unaffected, with $\partial\sigma_{Pt}/\partial r_{PtX}$ = −3036 ppm/Å in both the continuum and gas-phase.

In an attempt to improve on our model, the shielding/bond-length derivatives determined in the polarized continuum was used together with the gas-phase zero-point corrections for the isotopologues and isotopomers of **(2)** to estimate shielding according to the increment method by Eq. 4.1. The result is plotted in Figure 4.16 on the same axis as the gas-phase shieldings calculated using DFT. Overall, there seems to be no improvement, mainly because bond-length changes are the decisive factor and not the shielding/bond-length derivatives.

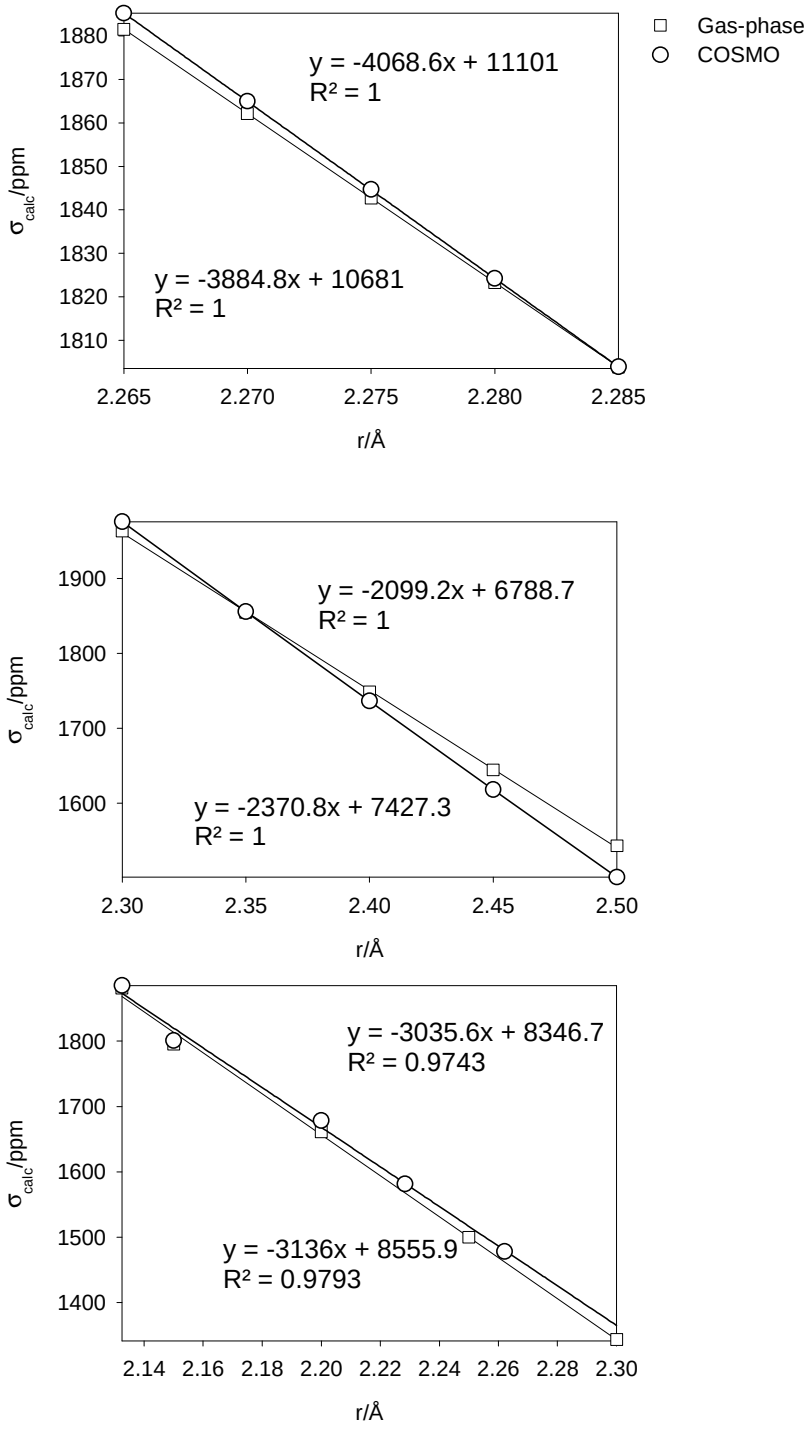

Figure 4.15: Plot of ^{195}Pt magnetic shielding of *cis*-$PtCl_4(H_2O)_2$ vs. (top) Pt-Cl_{eq}, (middle) Pt-Cl_{ax} and (bottom) Pt-O bond distances, evaluated at the COSMO/ZORA-SO/PW91 level as well as at the ZORA-SO/PW91 level.

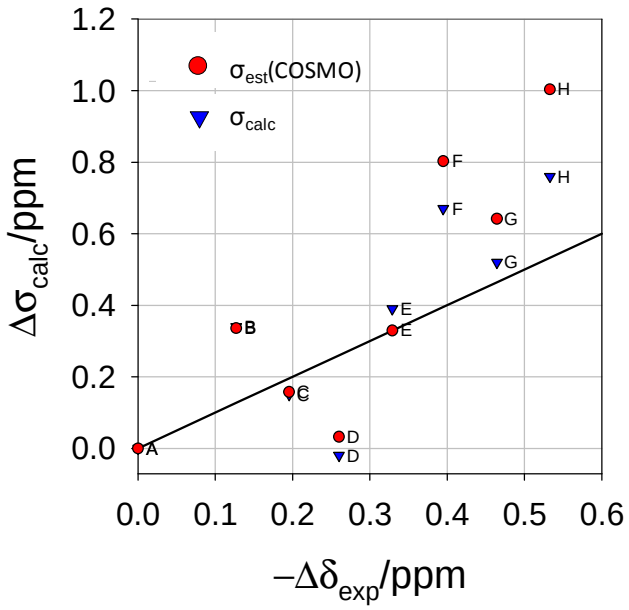

Figure 4.16 Shielding differences in $^{35/37}$Cl isotopomers of **2**, estimated from Eq. 4.1 using $\partial\sigma_{Pt}/\partial r_{PtX,I}$ in a polarizable continuum and calculated shielding differences vs. negative experimental $^{35/37}$Cl isotope shifts of the isotopomers of **2**, including the line with unity slope.

4.3 Conclusions

In summary, we have presented calculations of magnetic shieldings at appropriate DFT levels for the isotopologues and isotopomers of Pt(IV) aqua-chlorido complexes. To this end, zero-point vibrationally averaged (r_g^0) structures were computed. The numerical stability of the underlying perturbational approach has been validated by employing different step sizes and grids of increasing precision in the numerical integration. Gas-phase geometries were calculated for $[Pt^{35}Cl_6]^{2-}$ and $[Pt^{37}Cl_6]^{2-}$, for the $[Pt^{35}Cl_n{}^{37}Cl_{5-n}(H_2{}^{16}O)]^-$ (n=0-5), *cis*-$Pt^{35}Cl_n{}^{37}Cl_{(4-n)}(H_2{}^{16}O)_2$ (n=0-4), and *fac*-$[Pt^{35}Cl_n{}^{37}Cl_{(3-n)}(H_2{}^{16}O)_3]^+$ (n=0-3) isotopologues and isotopomers, as well as their $H_2{}^{16/18}O$ isotopologues. The ^{195}Pt NMR chemical shifts computed for these species reproduce the order of magnitude of the observed effect reasonably well, up to ca. 1 ppm. In most cases, general trends are also captured qualitatively, thus providing the first theoretical basis for the origin of subtle isotope shifts in ^{195}Pt NMR spectra. Unfortunately, neither simple polarizable continuum models nor small, microsolvated complexes lead to improved isotope shifts for the series investigated. The most important conclusion of our study is that the changes in bond distances necessary to rationalize these isotope shifts are but on the femtometer scale.

Chapter 5

Calculation of $^{35/37}$Cl and $^{16/18}$O isotope effects on ^{195}Pt NMR nuclear shielding of $[Pt^{35/37}Cl_n(^{16/18}OH)_{6-n}]^{2-}$ complexes

5.1 Introduction

In the previous chapter it was shown that the gas-phase geometries were calculated for $[Pt^{35}Cl_6]^{2-}$ and $[Pt^{37}Cl_6]^{2-}$, for the $[Pt^{35}Cl_n{}^{37}Cl_{5-n}(H_2{}^{16}O)]^{-}$ (n=0-5), *cis*-$Pt^{35}Cl_n{}^{37}Cl_{(4-n)}(H_2{}^{16}O)_2$ (n=0-4), and *fac*-$[Pt^{35}Cl_n{}^{37}Cl_{(3-n)}(H_2{}^{16}O)_3]^{+}$ (n=0-3) isotopologues and isotopomers, as well as their $H_2{}^{16/18}O$ isotopologues.

The computational protocol is now extended to $[Pt^{35}Cl_n{}^{37}Cl_{5-n}(OH)]^{2-}$ (n=0-5), *cis*-$[Pt^{35}Cl_n{}^{37}Cl_{(4-n)}(OH)_2]^{2-}$ (n=0-4), *fac*-$[Pt^{35}Cl_n{}^{37}Cl_{(3-n)}(OH)_3]^{2-}$ (n=0-3), *cis*-$[Pt^{35}Cl_n{}^{37}Cl_{2-n}(OH)_4]^{2-}$ (n=0-2) and $[Pt^{35}Cl_n{}^{37}Cl_{1-n}(OH)_5]^{2-}$ (n=0-1)., as well as their $^{16/18}$OH isotopologues. For the aquo complexes, large solvation effects were apparent, cf. the microsolvated complex (Figure 4.14). It is known that immersion in a polar solvent can reinforce metal-water bonds, probably due to cooperative polarization effects.[112] In the gas phase, DFT tends to underestimate metal-ligand bond strengths, in particular in dative bonds involving water. The consequences on the computed isotope shifts are yet unknown.

For the *fac*-$[Pt^{35/37}Cl_3(OH_2)_3]^{+}$ species, immersion in a polar solvent by means of the PCM method, shortens the Pt-O bond by 0.034 Å, consistent with a stronger stiffer bond. This caused the Pt-Cl bond-length to increase by 0.0127 Å. The effect was less pronounced in the *fac*-$[Pt^{35/37}Cl_3(OH)_3]^{2-}$ species, where the Pt-O bond-length decreased by only 0.0015 Å. Interestingly, the Pt-Cl bond-length also decreased, by 0.0290 Å. While the hydroxyl complexes are expected to interact more strongly with the solvent than the aquo species due to their higher charge (-2), this overall contraction of the coordination sphere indicates that solvation affects the bonds rather more uniformly in the hydroxy than in the aquo complexes. Thus, the protocol for the gas-phase calculations presented in Chapter 4, could still be a better approximation to the situation in solution, if effective error cancelation occurs.

5.2 Results and Discussion

5.2.1 Geometries

DFT geometry optimizations were performed to calculate the ground-state equilibrium and zero-point averaged structures in the gas-phase of all the relevant complexes in this part of the thesis. Details regarding basis-sets and other parameters were presented in Chapter 3. These structures were then used in the theoretical determination of the ^{195}Pt shielding tensors. Figure 5.1 shows the optimized geometries of **(4)** $[PtCl_5(OH)]^{2-}$, **(5)** *cis*-$[PtCl_4(OH)_2]^{2-}$, **(6)** *fac*-$[PtCl_3(OH)_3]^{2-}$, **(7)** *cis*-$[PtCl_2(OH)_4]^{2-}$ and **(8)** $[PtCl(OH)_5]^{2-}$.

In all minima, the OH bonds are essentially eclipsing other Pt-O or Pt-Cl bonds, arguably due to intramolecular OH...X interactions driven by electrostatics (for proper hydrogen bonds, the bond angles would be too small). No extensive conformational searches were undertaken, except for *cis*-$[PtCl_4(OH)_2]^{2-}$, as discussed in the following section.

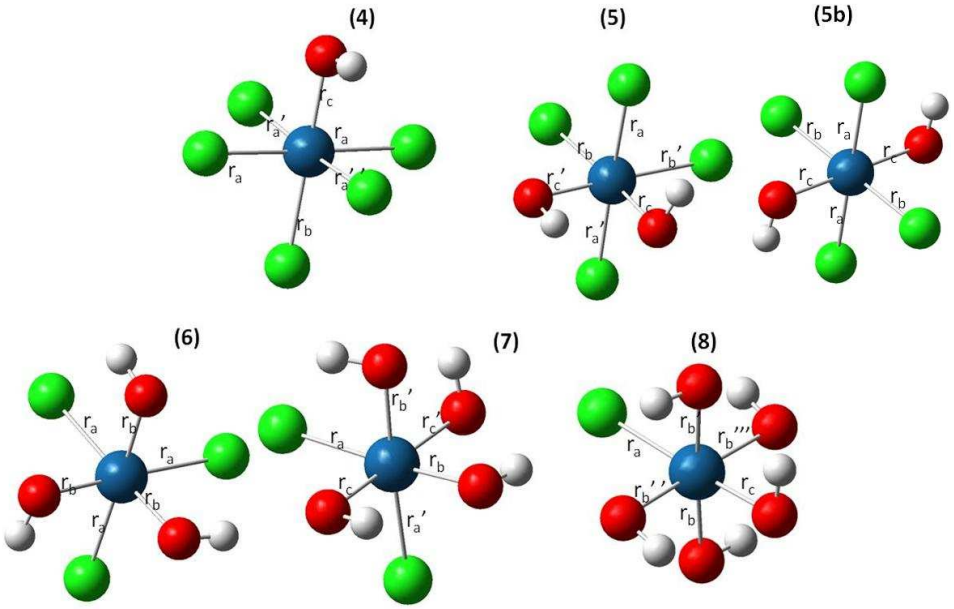

Figure 5.1: Optimized structures of **(4)** $[PtCl_5(OH)]^{2-}$, **(5)** *cis*-$[PtCl_4(OH)_2]^{2-}$, **(6)** *fac*-$[PtCl_3(OH)_3]^{2-}$, **(7)** *cis*-$[PtCl_2(OH)_4]^{2-}$, **(8)** $[PtCl(OH)_5]^{2-}$ and **(5b)** *trans*-$[PtCl_4(OH)_2]^{2-}$.

The Pt-Cl bonds trans to a hydroxyl group are longer as indicated by XRD measurements of r_b in Table 5.1. This is mainly due to the larger *trans* influence of OH^- relative to that of Cl^-.[110] For the aquo complexes, the *trans* influence of Cl^- was larger than that of H_2O, leading to a shorter Pt-Cl bond trans to a coordinated H_2O.

The Pt-^{35}Cl bonds are longer relative to Pt-^{37}Cl bonds as expected from the effect of anharmonicity as seen in Table 5.2. A similar trend was found for the Pt-O bonds in Table 5.3, where the Pt-^{16}O bonds extend further in space than the corresponding Pt-^{18}O bond.

Note that the zero-point corrections are of the same order of magnitude as for the aquo complexes.

Although the *trans* isomer of $[PtCl_4(OH)_2]^{2-}$ is found to crystallize better with particular counter-ions as shown by the lack of XRD data for the *cis* isomer, calculated energies for the *cis*-$[PtCl_4(OH)_2]^{2-}$ is 0.3 kcal/mol lower. Thus, for the purpose of this study, only **(5)** *cis*-$[PtCl_4(OH)_2]^{2-}$ was included in the isotope shift calculations.

Table 5.1: Differences between effective bond distances for **4** to **8** [in Å] calculated at the PBE0/SDD/6-31G* level.

	r^a	r^b	r^c	$\Delta^{35}r_{eff}{}^a$	$\Delta^{35}r_{eff}{}^b$	$\Delta^{35}r_{eff}{}^c$
4	2.370667	2.408578	2.00488	0.004065	0.003408	0.005835
Exp.[a]	2.3044	2.3091	2.0581			
5	2.384985	2.39589	2.009518	0.003700	0.004709	0.005444
6	2.435381	1.992067		0.003786	0.006267	
7	2.433925	1.989044	2.029329	0.002170	0.007513	0.005925
8	2.444902	2.02329	1.990212	0.004840	0.006471	0.006150
5b	2.36894	2.37285	2.03542			
Exp.[b]	2.32120	2.32432	2.02661			

[a]From Bondar, V. I., Potekhin, K. A., Rau, T. F., Rozman, S. P., Rau, V. G., & Struchkov, Y. T. (1988) *Soviet Physics Doklady* 33, 395. [b]From Murray, P., & Koch, K. R. (2010). *J. Coord. Chem.*, *63*(14-16), 2561.

Table 5.2: Differences between effective bond distances for **4** to **8** [in Å] calculated at the PBE0/SDD/6-31G* level.

	$^{35}r_{eff}{}^a$	$^{35}r_{eff}{}^b$	$^{35}r_{eff}{}^c$	$\Delta^{35}r_{eff}{}^a$-$\Delta^{37}r_{eff}{}^a$	$\Delta^{35}r_{eff}{}^b$-$\Delta^{37}r_{eff}{}^b$	$\Delta^{35}r_{eff}{}^c$-$\Delta^{37}r_{eff}{}^c$
4	2.374732	2.411986	2.010715	0.000088	0.000079	0.000009
5	2.388685	2.400599	2.014962	0.000247	0.000153	-0.000015
6	2.439167	1.998334		0.000343	0.000055	
7	2.436095	1.996557	2.035254	0.000388	-0.000001	0.000057
8	2.449742	2.029761	1.996362	0.000182	-0.000036	-0.000054

Table 5.3: Differences between effective bond distances for **4** to **8** [in Å] calculated at the PBE0/SDD/6-31G* level.

	$^{16}r_{eff}{}^{a}$	$^{16}r_{eff}{}^{b}$	$^{16}r_{eff}{}^{c}$	$\Delta^{16}r_{eff}{}^{a}-\Delta^{18}r_{eff}{}^{a}$	$\Delta^{16}r_{eff}{}^{b}-\Delta^{18}r_{eff}{}^{b}$	$\Delta^{16}r_{eff}{}^{c}-\Delta^{18}r_{eff}{}^{c}$
4	2.374732	2.411986	2.010715	0.000021	-0.000031	0.000211
5	2.388685	2.400599	2.014962	0.000246	0.000115	0.000213
6	2.439167	1.998334		0.000119	0.000196	
7	2.436095	1.996557	2.035254	-0.000153	0.000151	0.000068
8	2.449742	2.029761	1.996362	0.000074	0.000129	0.000258

5.2.2 Free rotation about the Pt-O bond

In complex **(5)**, there is one OH...O and one OH...Cl contact. Two OH...Cl contacts can be enforced by imposing C_2 symmetry. This stationary point is not a minimum, but rather a transition state (with one imaginary frequency) connecting two degenerate rotamers of the C_1-symmetric minimum, as shown in the energy profile below.

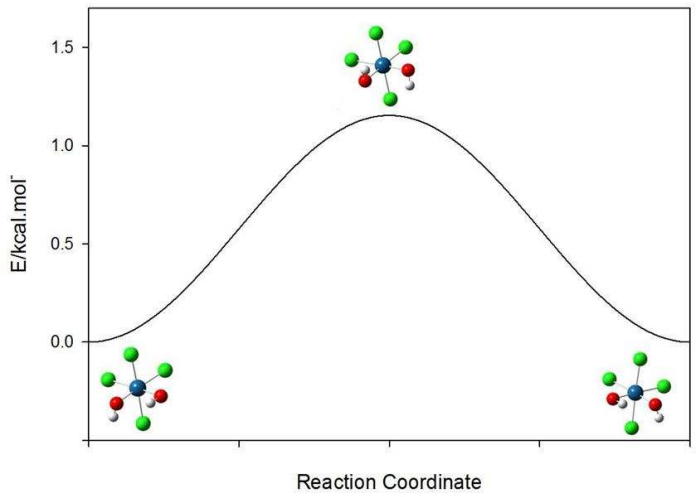

Figure 5.2: Energy profile of *cis*-$[PtCl_4(OH)_2]^{2-}$. The minima obtained interconvert via the transition state shown at the maximum.

The energy barrier for this interconversion shown in Figure 5.2, is 1.2 kcal.mol^{-1}, which is readily overcome on the timescale of the NMR experiments under standard conditions in solution (typical barriers that can be "frozen out" in variable-temperature NMR are on the order of ~10 kcal.mol^{-1}, the precise value depending on the shift difference and the actual rate constant[3]).

Thus, it is likely that the OH groups rotate spontaneously and rapidly about the Pt-O bonds on the NMR time-scale.[3]

5.2.3 Isotope shifts

All possible $^{35/37}$Cl isotopomers were calculated in the gas phase for a representative set of mixed Pt(VI) chloro/hydroxido complexes **4 – 8**. The resulting vibrationally averaged structures were used as inputs for relativistic calculations of isotropic magnetic shielding constants at the ZORA-SO/PW91/QZ4P/TZ2P level. To compare with experiment, isotope shifts $\Delta\delta$ were calculated relative to the corresponding all-^{35}Cl isotopologue set to $\delta = 0$.

Many of the static isotopomer structures can be interconverted through simple OH rotation about the Pt-O bonds, processes that are expected to occur very rapidly on the NMR time scale as discussed in 5.2.2. Thus, it is reasonable to assume that those isotopomers that are grouped together in the legends will only show a single NMR signal, and their computed shielding constants were averaged accordingly. The results for complex **4** will first be discussed in detail, then those for species **5 – 8** will be discussed together.

For complex **4**, the resulting shielding constants and the corresponding experimental isotope shifts are collected in Table 5.4 and, after conversion of the computed shieldings into relative shifts, plotted against each other in Figure 5.3. The sign of the experimental isotope shifts has been reversed, so that they appear in the same sequence as in a conventional NMR spectrum.

The overall observed trends as well as the overall order of magnitude of the isotope shifts are reasonably well reproduced by our computational protocol. As found for the aquo complexes in the previous chapter, however, there are quantitative discrepancies, apparent in a noticeable scatter of the data and a typically overestimated slope of the $\Delta\sigma_{calc}$ vs. $\Delta\delta_{exp}$ data. It is unclear at present whether these discrepancies are due to residual numerical errors in the computations, deficiencies of the overall model (e.g. the neglect of thermal effects beyond the zero-point corrections), or missing solvation.

Overall, however, this result is consistent with what has been found in the previous chapter, further validating our model.

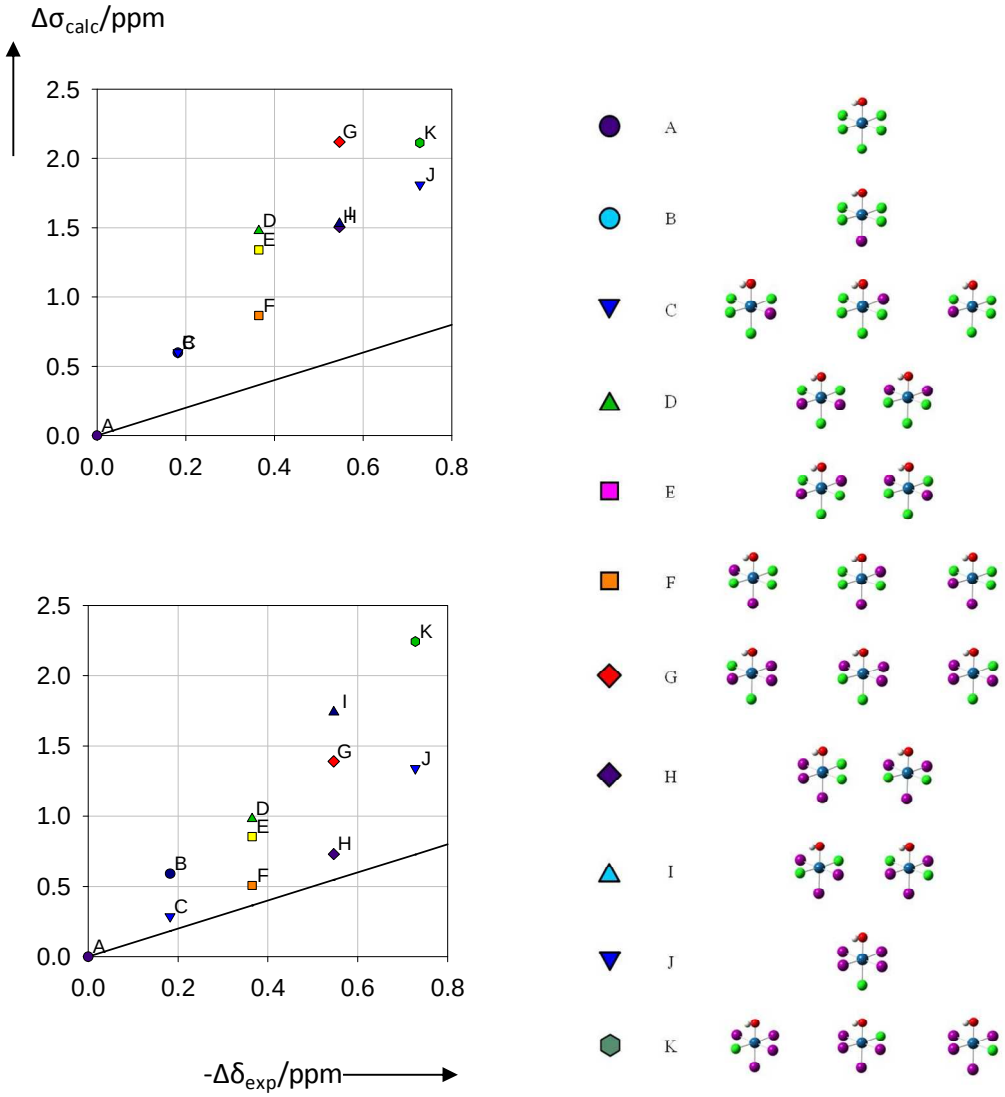

Figure 5.3: Calculated shielding differences vs. negative experimental $^{35/37}$Cl isotope shifts of the isotopomers of $[PtCl_5(OH)]^{2-}$;color code: ^{35}Cl green, ^{37}Cl purple. Top ^{16}O, bottom: ^{18}O

On going from the ^{16}O (top left) to ^{18}O species, there is a slight increase in agreement with experiment. This was not the case for the aquo complexes in Chapter 4 .

It appears that the sensitivity of the Pt-O bond length toward isotopic substitution is still not very well captured by the present approach: e.g. experimentally for $[Pt^{35/37}Cl_5(OH)]^{2-}$, substitution of ^{16}O for ^{18}O in each isotopomer affords a rather constant upfield shift of $\Delta\delta(^{195}Pt) \approx 0.7\pm0.05$ ppm. The variation in the computed $\Delta\sigma$ values is much larger and the isotopomers are not grouped together, ranging from $\Delta\sigma \approx +0.8$ ppm to $\approx$ -0.008 ppm (see Figure 5.4) similar to the aquo complexes (See Fig. 4.8). It is likely that neglecting the solvent would exaggerate the difference in r_g^0

between isotopomers. Upon moving from the ^{16}O to ^{18}O species, a stronger, stiffer Pt-O bond results in a slightly lower discrepancy between isotopomers (see Figure 5.3).

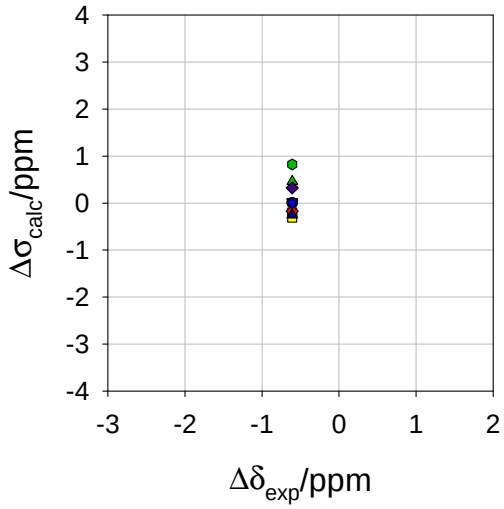

Figure 5.4: Plot of difference between calculated σ values of $[Pt^{35/37}Cl_5(^{16}OH)]^{2-}$ and $[Pt^{35/37}Cl_5(^{18}OH)]^{2-}$ vs. the corresponding difference between the experimental δ values(see Figure 5.3 for the color code denoting the isotopomers).

The corresponding isotope shifts in species **5 – 8** are plotted against experiment in Figures 5.5 – 5.8 (see Tables 5.4a and 5.4b for the numerical data).

Table 5.4a: Experimental[18] ^{195}Pt chemical shifts and computed isotropic shielding constants for the $^{35/37}$Cl isotopomers and isotopologues of (**4**) – (**8**).

	(4)		(5)		(6)		(7)		(8)	
	δ_{exp}/ppm	σ_{calc}/ppm	δ_{exp}/ppm	σ_{calc}/ppm	δ_{exp}/ppm	σ_{calc}/ppm	δ_{exp}/ppm	σ_{calc}/ppm	δ_{exp}/ppm	σ_{calc}/ppm
A	665.31	943.10	1276.00	447.62	1845.19	9.00	2351.99	-228.77	2820.86	-341.30
B	665.13	943.70	1275.81	449.77	1844.99	10.73	2351.78	-227.74	2820.63	-340.54
C	665.13	943.70	1275.81	447.68	1844.79	10.97	2351.57	-225.54		
D	664.95	944.58	1275.62	449.00	1844.59	11.21				
E	664.95	944.44	1275.62	448.71						
F	664.95	943.97	1275.62	448.80						
G	664.77	945.22	1275.42	448.84						
H	664.77	944.61	1275.42	449.15						
I	664.77	944.63	1275.23	450.53						
J	664.58	944.91								
K	664.58	945.21								

Table 5.4b: Experimental[18] ^{195}Pt chemical shifts and computed isotropic shielding constants for the ^{18}O enriched $^{35/37}$Cl isotopomers and isotopologues of (**4**) – (**8**).

	(4)		(5)		(6)		(7)		(8)	
	δ_{exp}/ppm	σ_{calc}/ppm	δ_{exp}/ppm	σ_{calc}/ppm	δ_{exp}/ppm	σ_{calc}/ppm	δ_{exp}/ppm	σ_{calc}/ppm	δ_{exp}/ppm	σ_{calc}/ppm
A	666.42	943.71	1276.56	449.61	1843.96	11.21	2345.84	-228.19	2811.97	-335.93
B	666.24	944.30	1276.36	450.14	1843.33	11.20	2345.63	-227.62	2811.75	-332.74
C	666.24	944.00	1276.36	449.72	1842.71	12.51	2345.41	-227.25		
D	666.06	944.69	1276.17	450.32	1842.09	11.64				
E	666.06	944.57	1276.17	450.72						
F	666.06	944.22	1276.17	450.56						
G	665.88	945.10	1275.98	450.39						
H	665.88	944.44	1275.98	451.37						
I	665.88	945.45	1275.78	452.80						
J	665.69	945.05								
K	665.69	945.95								

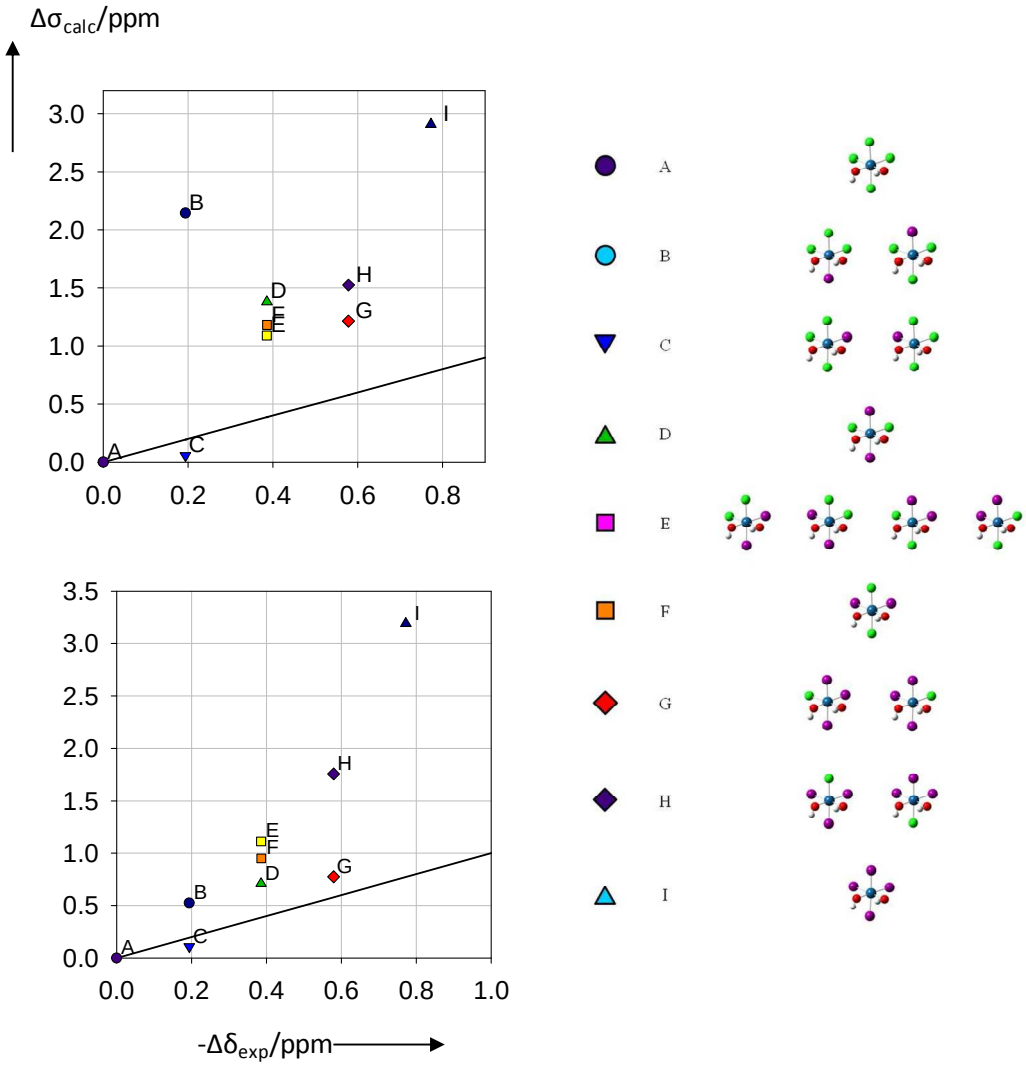

Figure 5.5: Calculated shielding differences vs. negative experimental $^{35/37}$Cl isotope shifts of the isotopomers of **(5)** *cis*-$[PtCl_4(OH)_2]^{2-}$; color code: ^{35}Cl green, ^{37}Cl purple. top left ^{16}O, bottom left: ^{18}O

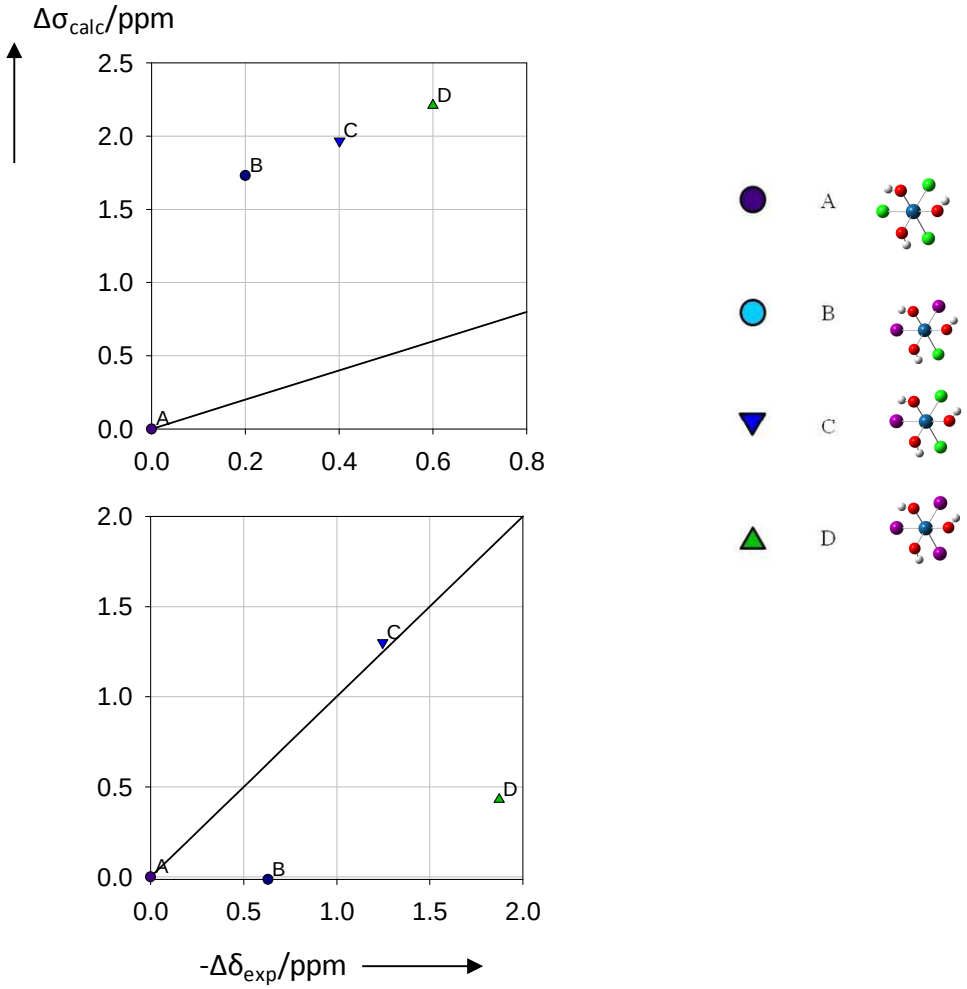

Figure 5.6: Calculated shielding differences vs. negative experimental $^{35/37}$Cl isotope shifts of the isotopomers of **(6)** *fac*-$[PtCl_3(OH)_3]^{2-}$color code: ^{35}Cl green, ^{37}Cl purple. top left ^{16}O, bottom left: ^{18}O

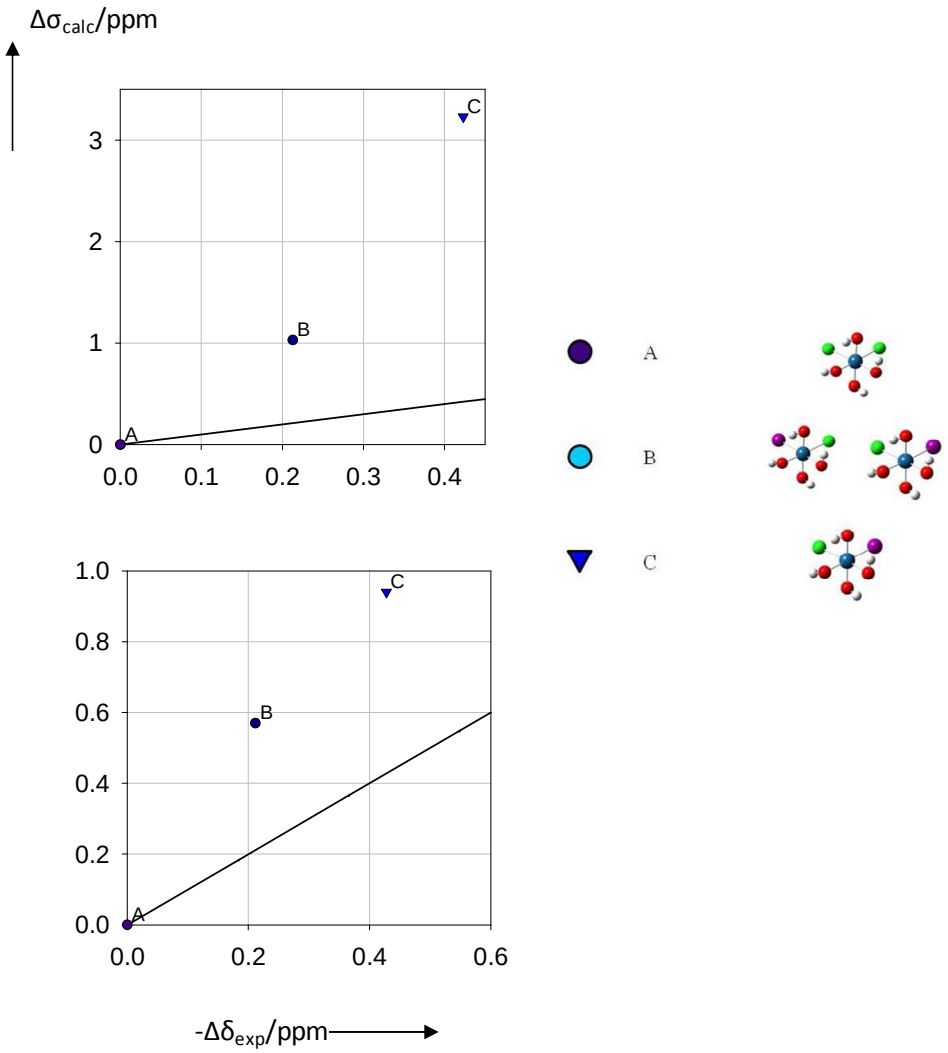

Figure 5.7: Calculated shielding differences vs. negative experimental $^{35/37}$Cl isotope shifts of the isotopomers of **(7)** *cis*-$[PtCl_2(OH)_4]^{2-}$; color code: ^{35}Cl green, ^{37}Cl purple. top left ^{16}O, bottom left: ^{18}O

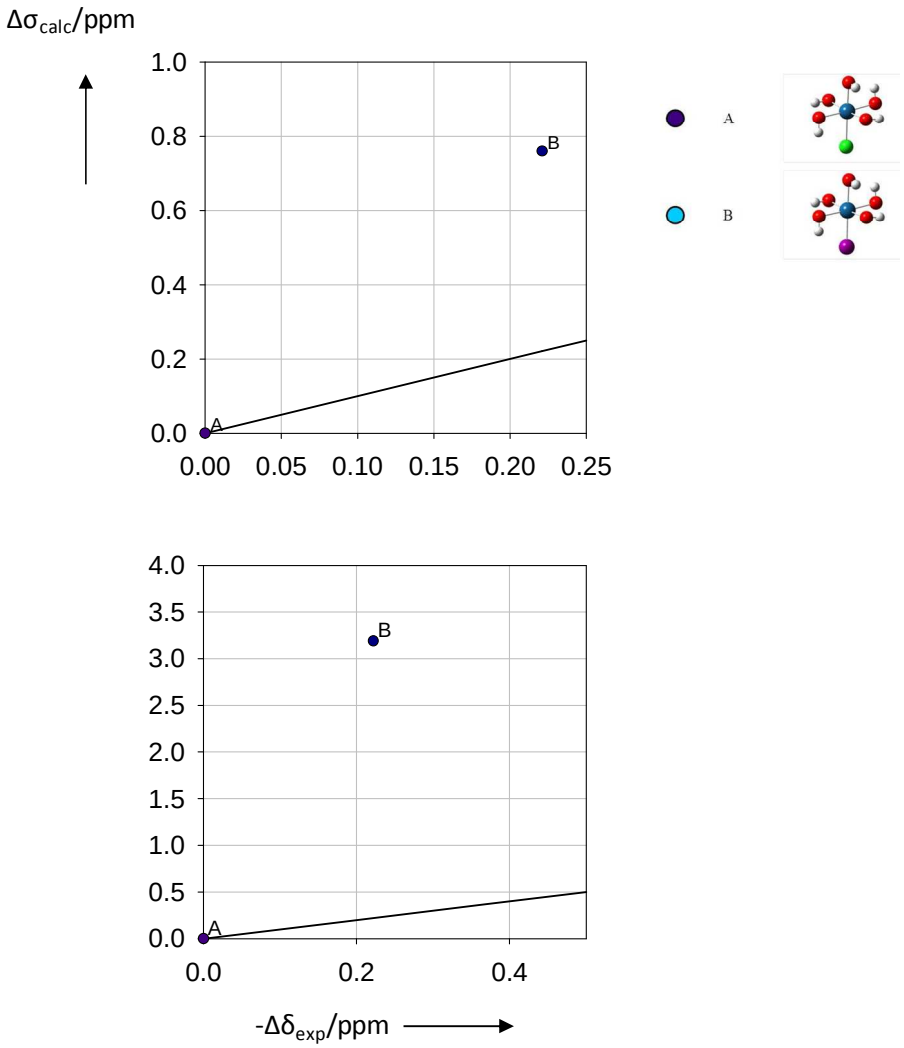

Figure 5.8: Calculated shielding differences vs. negative experimental $^{35/37}$Cl isotope shifts of the isotopomers of **(8)** $[PtCl(OH)_5]^{2-}$; color code: ^{35}Cl green, ^{37}Cl purple. top left ^{16}O, bottom left: ^{18}O

For complex **(5)**, there seems to be some improvement on moving to ^{18}O enriched species i.e. less scatter and deviation from the ideal line. The isotope shifts of isotopomers B and C are also closer together, consitant with what has been found experimentally.

The overestimation of Δσ, may be due to the neglect of the effect of the solvent, which causes the Pt-Cl bonds to contract, rendering it slightly less sensitive towards isotopic substation. The same effect is seen in Figure 5.7 for complex **(7)**.

Although, the general trend and order of magnitude is reasonably well reproduced for complexes **(4)-(8)**, the overall agreement with experiment is less pronounced for the hydroxyl than for the aquo complexes as can be seen by the overestimation of the slope of the calculated shielding differences vs. experimental $^{35/37}$Cl isotope shifts plots.

5.2.4 Shielding/bond-length derivatives

From the previous chapter, it was shown that the bond length changes due to zero-point vibrations is the dominant factor influencing the isotope shifts.

To test the models feasibility for the hydroxyl complexes we used representative shielding/bond-length derivatives $\partial\sigma_{Pt}/\partial r_{PtX}$ (X = O and Cl), together with the computed zero-point corrections for each bond length (Δr_g^0 in eq 4.1), in order to estimate effective shieldings according to Eq. 4.1.

These estimated shieldings can then be compared to the actual effective shieldings computed for the actual vibrationally averaged structure.

Pt-Cl and Pt-O shielding/bond-length derivatives have been evaluated for **(4)**-**(8)**, respectively, by rigid scans of the Pt-Cl and Pt-O bonds about their equilibrium values. The resulting $\partial\sigma_{Pt}/\partial r_{PtCl}$ and $\partial\sigma_{Pt}/\partial r_{PtO}$ values are listed in Table 5.5.

Table 5.5: Shielding/bond-length derivatives $\partial\sigma_{Pt}/\partial r_{PtX}$ computed[a] for complexes **1 - 5** at the ZORA-SO/PW91 level.

Compd.	Bond[b]	$\partial\sigma_{Pt}/\partial r_{PtX}$ [ppm/Å]
4	(r_c)Pt-O	-781
	(r_b)Pt-Cl[c]	-2144
	(r_a)Pt-Cl	-4452
5	(r_c)Pt-O	-2134
	(r_b)Pt-Cl[c]	-2934
	(r_a)Pt-Cl	-5188
7	(r_c)Pt-O[c]	-1880
	(r_b)Pt-O	-1721
	(r_a)Pt-Cl	-4142
8	(r_b)Pt-O[c]	-2323
	(r_c)Pt-O	-2608
	(r_a)Pt-Cl	-3306

[a]Obtained through rigid displacements of the ligands about the equilibrium value of the designated bond, see Figure 4.9 for an example. [b]See Figure 4.1 for definition. [c]trans to hydroxyl ligand

Because Pt-Cl bonds trans to a hydroxyl ligand may behave differently from those trans to another chloride, the shielding/bond-length derivative was also evaluated for the trans-Cl atom in **(4)** and **(5)**, similarly, for the trans-O atom in **(7)** and **(8)**.

Figure 5.9 shows the resulting estimated $^{37/35}$Cl isotope effects on the ^{195}Pt shieldings of **4**-**8**, plotted vs. the actual computed values. These shielding/bond-length derivatives will be compared to those in the aquo complexes in Section 5.2.6.

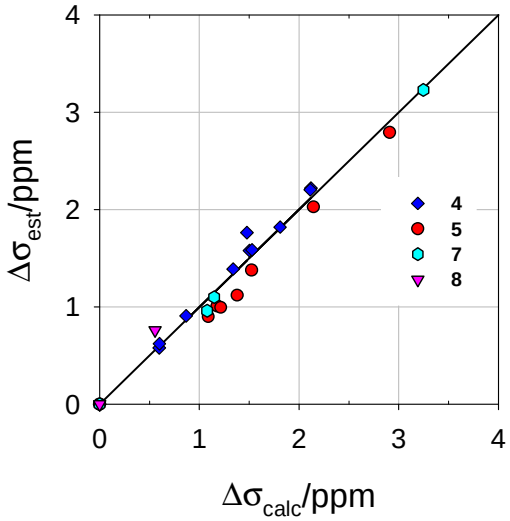

Figure 5.9 Shielding differences in $^{35/37}$Cl isotopomers of **4** - **8**, estimated from eq 4.1 vs. actual computation from r_g^0 geometries, including the line with unity slope.

Both span and sequence of the Δσ values are described rather well by the increment method. This result further substantiates our underlying model, namely that the bond length changes due to zero-point vibrations is the dominant factor influencing the isotope shifts.

5.2.5 Solvation effects

In an attempt to understand the interaction with the solvent, an explicit H_2O was added to the input structure of **(4)**. The optimization converged to the minimum shown below.

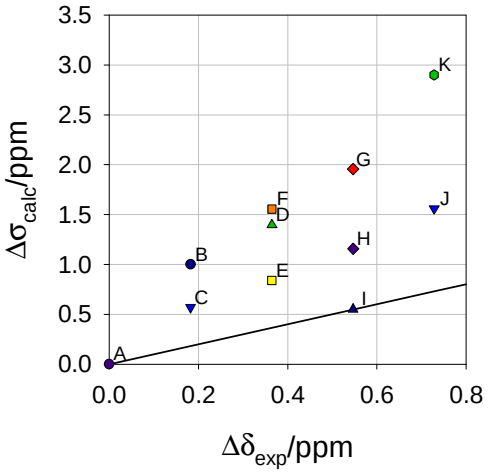

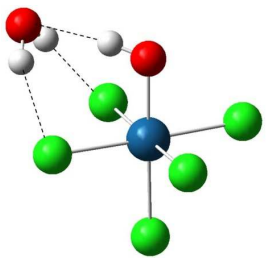

Figure 5.10: Calculated shielding differences vs. negative experimental $^{35/37}$Cl isotope shifts of the isotopomers of $[PtCl_5(OH)]^{2-}\cdot H_2O$, including the ideal line with unity slope.

The geometry is different from the gas-phase structure, as the Pt-O bond is staggered relative to the Pt-Cl bonds. The solvent is in proximity to the chlorides and hydroxide to allow for hydrogen bonding, as shown by the dotted lines.
This bonding mode is not necessarily representative of the situation in solution, where the water in the first hydration-sphere may rather interact with water molecules from the bulk. This species is studied as a first step towards full solvation.
On going from pristine **(4)** to $[PtCl_5(OH)]^{2-}\cdot H_2O$, the equilibrium Pt-O bond-length decreases from 2.005 Å to 2.002 Å, similar to what has been found for complex **(6)** when going from the gas-phase to the continuum, with a bond contraction from 0.003-0.002 Å consistent with a stronger, stiffer bond.

The isotopomers of each isotopologue (grouped together here as: B,C ; D,E,F ; H,I,G and J,K) are not resolved experimentally. Thus, computationally, each group of isotopomers should have the same Pt shielding. This would imply that all the data points B,C should fall on the same point, the same with D,E,F ; H,I,G and J,K.

However, this is not the case neither for the pristine complex in the gas-phase (Fig. 5.3) nor for this microsolvated complex in fact, also, the discrepancies between isotopomers increase somewhat upon microsolvation.

The failure to resolve isotopomers could also be due to rapid (on the NMR time-scale) interconversion between them. This possibility is highly unlikely, however, because conformational non-rigidity is very difficult to explain why the hydroxyl complex should be fluxional whereas the corresponding aquo species would not be.

An associate exchange mechanism involving more fluxional 7-coordinate intermediates is also unlikely. Indeed, recent preliminary studies on $[PtCl_6]^{2-}$ in enriched $Na^{35}Cl$ solution suggest that Cl^- exchange is slow on the NMR time-scale.[18]

Modeling isotope effects in solution has been difficult with our protocol, however, insight can be gained into the factors affecting shielding without the need to fully model the solvent. To this end shielding/bond-length derivatives have been evaluated in the polarized continuum for **(5)**, by rigid scans of the Pt-Cl and Pt-O bonds about their equilibrium values as shown in Figure 5.11. The resulting $\partial\sigma_{Pt}/\partial r_{PtX}$ values are not much different from what was found in the gas-phase. Immersion in a polarized continuum, increased $\partial\sigma_{Pt}/\partial r_{PtX}$ for $Pt\text{-}Cl_{eq}$ from -2934 to

−2962 ppm/Å, while, that for Pt-Cl_{ax} decreased significantly from -5188 to −4019 ppm/Å. The $\partial\sigma_{Pt}/\partial r_{PtX}$ value for the Pt-O bonds decreased from -2134 to −1978 ppm upon immersion in a polar solvent. Shielding is slightly less dependent on the Pt-Cl_{ax} bonds in the polarized continuum, although this is still the largest contribution to the total shielding for this complex.

In an attempt to improve on our model, the shielding/bond-length derivatives determined in the polarized continuum was used together with the gas-phase zero-point corrections for the isotopologues and isotopomers of **(5)** to estimate shielding according to the increment method by Eq. 4.1. The result is plotted in Figure 5.12 on the same axis as the gas-phase shieldings calculated using DFT. Despite some scatter, the estimated shieldings are closer to our experimental observations. Moreover, the near-degenerate isotopomers D, E & F, are much closer together than in the pure gas-phase DFT calculations.

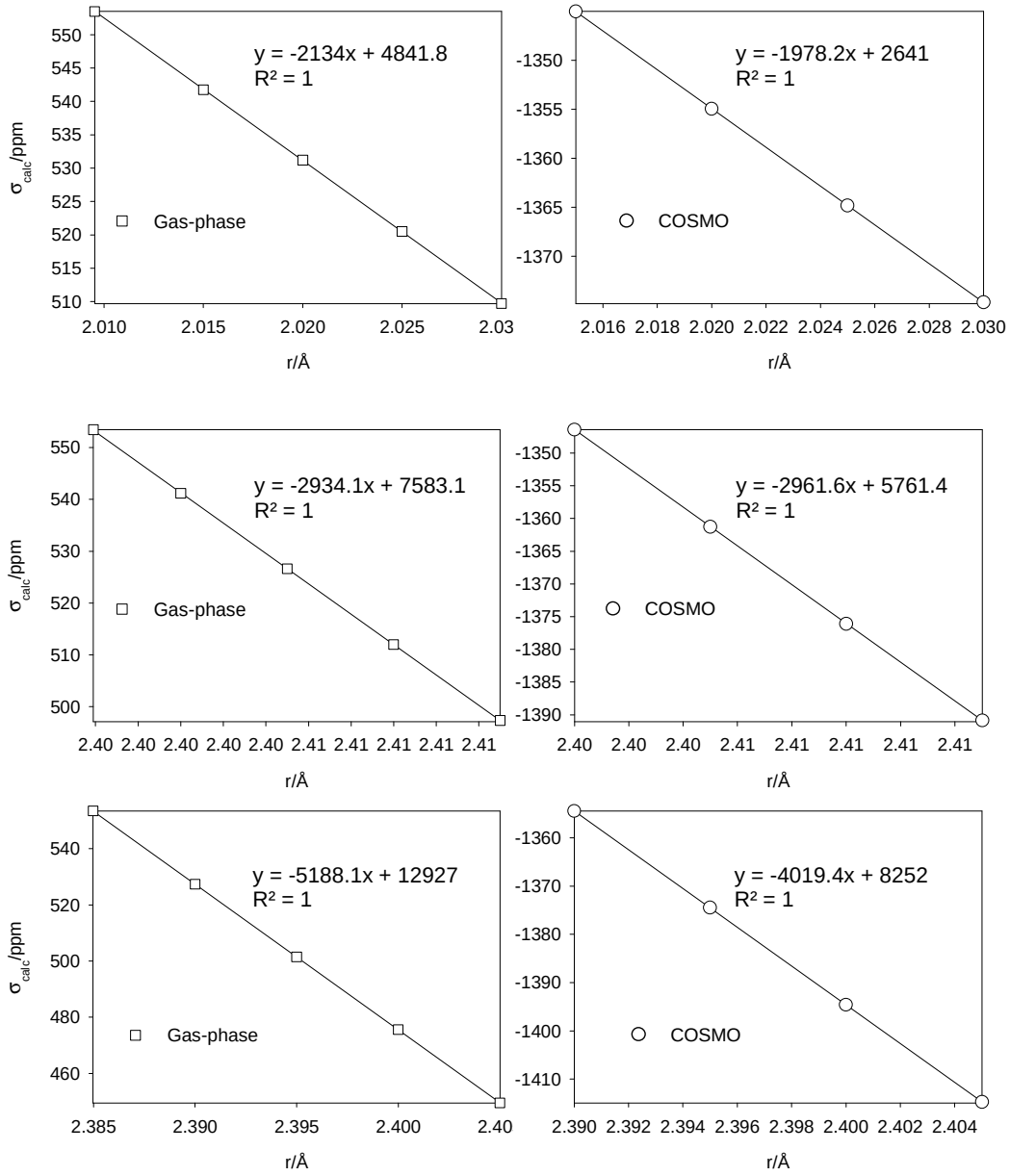

Figure 5.11: Plot of ^{195}Pt magnetic shielding of *cis*-$[PtCl_4(OH)_2]^{2-}$ vs. (top) Pt-O bond, (middle) Pt-Cl_{eq} and (bottom) Pt-Cl_{ax} distances, evaluated at the COSMO/ZORA-SO/PW91 level as well as at the ZORA-SO/PW91 level.

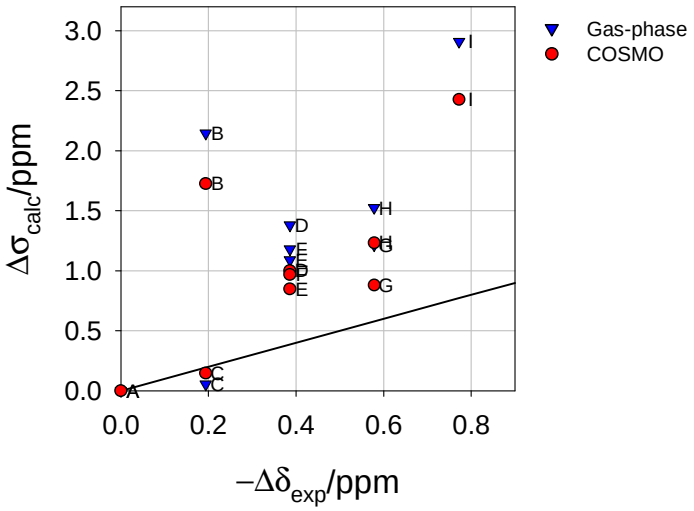

Figure 5.12 Shielding differences in $^{35/37}$Cl isotopomers of **5**, estimated from Eq. 4.1 using $\partial\sigma_{Pt}/\partial r_{PtX,I}$ in a polarizable continuum and calculated shielding differences vs. negative experimental $^{35/37}$Cl isotope shifts of the isotopomers of **5**, including the line with unity slope.

5.2.6 Comparison with aqua complexes

The main difference seen in the experimental ^{195}Pt NMR spectra between the aquo and the hydroxy complexes is the absence of isotopomers for the latter. As mentioned in the Chapter 1, no isotopomers can be resolved experimentally for the hydroxyl complexes.

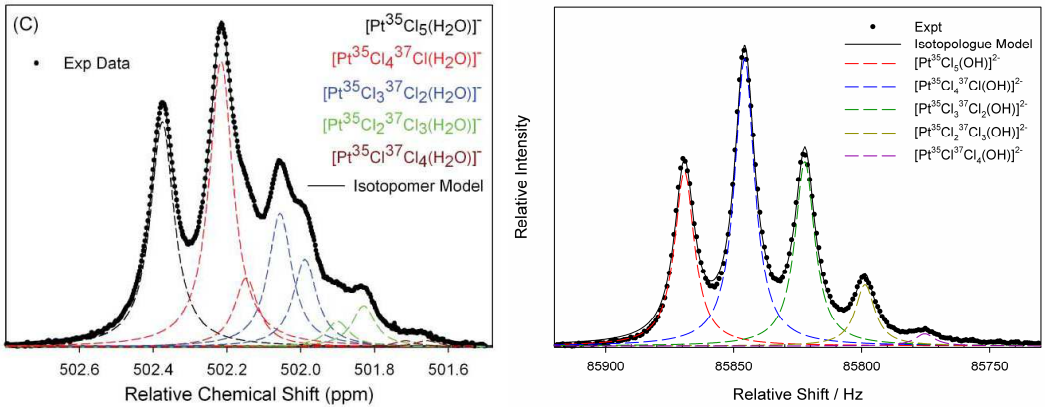

Figure 5.11: Experimental ^{195}Pt NMR spectra of $[PtCl_5(H_2O)]^-$ ^{2}and $[PtCl_5(OH)]^{2-}$.

When comparing $[PtCl_5(OH)]^{2-}$ and its protonated analogue $[PtCl_5(H_2O)]^-$, the calculated bond-length changes upon isotopic substitution alone cannot account for the absence of isotopomers in **(4)** to **(8)**.

Comparing the shielding/bondlength derivatives of $[PtCl_5(OH)]^{2-}$ (Pt-Cl_w -2143.9 ppm/Å, Pt-Cl -4451.8 ppm/Å) and $[PtCl_5(H_2O)]^-$ (Pt-Cl_w -4240 ppm/Å, Pt-Cl -2770 ppm/Å) where Cl_w is

trans to an OH^- or H_2O, it is noted that the Pt-Cl_w bond has a larger shielding/bondlength derivative than that of the Pt-Cl bond in $[PtCl_5(H_2O)]^-$. Also, this complex has isotopomers which can be detected experimentally.

Table 5.6 shows the shielding/bond-length derivatives of the complexes **(1)** and **(2)** as well as the protonated analogues thereof. Again, in the protonated complex **(2)** the Pt-Cl_{eq} bonds *trans* to a H_2O has a larger shielding/bond-length derivative than the Pt-Cl_{ax} bonds and the isotopomers are detected experimentally.

In the hydroxyl analogue, however, the Pt-Cl bonds trans to the OH^- group has a smaller shielding/bond-length derivative than the other Pt-Cl bonds in this complex and the isotopomers are not detected experimentally.

From Table 5.6 it seems that if the shielding/bond-length derivatives of the Pt-Cl bonds *trans* to the OH^- or H_2O are sufficiently larger than for the other Pt-Cl bonds and the averaged bond-displacements of the isotopomers are sufficiently dissimilar, isotopomers may be resolved.

Table 5.6: Shielding/bond-length derivatives $\partial\sigma_{Pt}/\partial r_{PtX}$ evaluated at the ZORA-SO/PW91 level.

Compd.	Bond[b]	$\partial\sigma_{Pt}/\partial r_{PtX}$ [ppm/Å]	Compd.	Bond[b]	$\partial\sigma_{Pt}/\partial r_{PtX}$ [ppm/Å]
4	(r_c)Pt-OH	-781	**1**	Pt-OH_2	-3167
	(r_b)Pt-Cl[c]	-2144		Pt-Cl_a	-2770
	(r_a)Pt-Cl	-4452		Pt-Cl_b	-2529
				Pt-Cl_c[c]	-4240
5	(r_c)Pt-OH	-2134	**2**	Pt-OH_2	-3136
	(r_b)Pt-Cl[c]	-2934		Pt-Cl_{ax}	-2099
	(r_a)Pt-Cl	-5188		Pt-Cl_{eq}[c]	-3885

[b]See Figures 4.1 and 5.1 for definition. [c]trans to hydroxyl/water ligand.

Table 5.7: Difference between shielding/bond-length derivatives $\partial\sigma_{Pt}/\partial r_{PtX}$ evaluated at the COSMO/ZORA-SO/PW91 and ZORA-SO/PW91 levels.

Compd.	Bond[b]	[a]$\Delta(\partial\sigma_{Pt}/\partial r_{PtX})$ [ppm/Å]	Compd.	Bond[b]	[a]$(\Delta\partial\sigma_{Pt}/\partial r_{PtX})$ [ppm/Å]
5	(r_c)Pt-OH	-156	**2**	Pt-OH_2	0
	(r_b)Pt-Cl_{eq}[c]	+28		Pt-Cl_{eq}[c]	+184
	(r_a)Pt-Cl_{ax}	-1169		Pt-Cl_{ax}	+271

[a]The negative sign implies a decrease in the absolute value of $\partial\sigma_{Pt}/\partial r_{PtX}$ when going from the gas-phase to the continuum. [b]See Figures 4.1 and 5.1 for definition. [c]trans to hydroxyl/water ligand.

Using the increment method to estimate shieldings from the gas-phase bond displacements and shielding/bond-length derivatives determined in a polarized continuum did not improve the results for the aquo complex **2**, possibly because bond-length changes are the decisive factor and not the shielding/bond-length derivatives. Despite some scatter, the estimated shieldings for the hydroxyl complex are closer to experimental observations.[18] Table 5.7 shows the changes in shielding/bond-length derivatives for **5** and **2** upon immersion in a polarized continuum. Remarkably, $\partial\sigma_{Pt}/\partial r_{PtX}$ for the aquo complex remains almost unaffected, compared to the hydroxyl complex.

For the *fac*-$[Pt^{35/37}Cl_3(OH_2)_3]^+$ species, immersion in a polar solvent by means of the PCM method, shortens the Pt-O bond by 0.034 Å, consistent with a stronger stiffer bond. This caused the Pt-Cl bond-length to increase by 0.0127 Å. The effect was less pronounced in the *fac*-$[Pt^{35/37}Cl_3(OH)_3]^{2-}$ species, where the Pt-O bond-length decreased by only 0.0015 Å. Interestingly, the Pt-Cl bond-length also decreased, by 0.0290 Å. Thus, for the aquo complexes, there is much larger distinction between adjacent Pt-Cl bonds, as opposed to the more uniform contraction of the coordination sphere in the hydroxyl complexes, which renders all Pt-Cl bonds in the hydroxyl complex nearly magnetically equivalent. This effect was illustrated in the previous section with Figure 5.12, where isotopomers D, E & F, are much closer together in the partial solvation model, consistent with experimental observations.

5.3 Conclusions

The computational protocol formulated in the previous chapter was extended to $[Pt^{35}Cl_n{}^{37}Cl_{5-n}(OH)]^{2-}$ (n=0-5), *cis*-$[Pt^{35}Cl_n{}^{37}Cl_{(4-n)}(OH)_2]^{2-}$ (n=0-4), *fac*-$[Pt^{35}Cl_n{}^{37}Cl_{(3-n)}(OH)_3]^{2-}$ (n=0-3), *cis*-$[Pt^{35}Cl_n{}^{37}Cl_{2-n}(OH)_4]^{2-}$ (n=0-2) and $[Pt^{35}Cl_n{}^{37}Cl_{1-n}(OH)_5]^{2-}$ (n=0-1)., as well as their $^{16/18}$OH isotopologues. The ^{195}Pt NMR chemical shifts computed for these species reproduce the order of magnitude of the observed effect reasonably well. In most cases, general trends are also captured qualitatively, although the isotope shifts tend to be notably overestimated.

It was indicated that the Pt-O bond can rotate spontaneous and rapidly on the NMR time-scale. A possible explanation based on the computed shielding/bond-length derivatives and calculations in a polarized continuum was proposed for why isotopomers are not resolved experimentally in some cases.

Chapter 6

Calculation of $^{35/37}$Cl isotope effects on ^{103}Rh NMR nuclear shielding of $[Rh^{35/37}Cl_n(H_2O)_{6-n}]^{3-n}$ complexes

6.1 Introduction

Recent developments show that at high magnetic fields with carefully controlled solution temperatures, the 19.11 MHz ^{103}Rh NMR signals of the series of $[RhCl_n(H_2O)_{6-n}]^{3-n}$ (n = 3–6) complexes in equilibrated hydrochloric acid solutions, are well-resolved into a distinctive 'fine-structure' due to ^{35}Cl/^{37}Cl isotopologue and isotopomer effects, resulting in a unique NMR 'finger-print', [19] with which it is possible to uniquely identify all chlorido containing Rh(III) complexes, an advantage due to the absence of a suitable universal reference compound in ^{103}Rh NMR spectroscopy, [20] which makes identifying peaks on the basis of chemical shift alone, impossible.

The ^{195}Pt NMR isotope shifts computed thus far reproduce the order of magnitude of the observed effect reasonably well, up to ca. 1 ppm. In most cases, general trends are also captured qualitatively, but quantitative accuracy has not been reached yet.

The computational protocol is now extended to $[Rh^{35}Cl_n{}^{37}Cl_{5-n}(H_2O)]^{2-}$ (n=0-5), *cis*-$[Rh^{35}Cl_n{}^{37}Cl_{(4-n)}(H_2O)_2]^-$ (n=0-4), and *fac*-$Rh^{35}Cl_n{}^{37}Cl_{(3-n)}(H_2O)_3$ (n=0-3) isotopologues and isotopomers.

The mono-aquo Rh(III) complex has a higher charge (-2) than the Pt(IV) complexes (up to ±1), which might lead to increased interactions with the solvent. With the same kind of trans influence operative in both Pt(IV) and Rh(III) series, the importance of the overall charge on the computed isotope shifts can now be assessed. Investigating these species and comparison to Pt(IV) aquo complexes would shed light on why isotopomers are resolved in some cases.

6.2 Results and Discussion

6.2.1 Geometries

DFT geometry optimizations were performed to calculate the ground-state equilibrium and zero-point averaged structures in the gas-phase of all the relevant complexes in this part of the thesis. Details regarding basis-sets and other parameters were presented in Chapter 3. These structures were then used in the theoretical determination of the ^{103}Rh shielding tensors. Figure 6.1 shows the optimized geometries of **(9)** $[Rh^{35}Cl_n{}^{37}Cl_{5-n}(H_2O)]^{2-}$ (n=0-5), **(10)** *cis*-$[Rh^{35}Cl_n{}^{37}Cl_{(4-n)}(H_2O)_2]^-$ (n=0-4), and **(11)** *fac*-$Rh^{35}Cl_n{}^{37}Cl_{(3-n)}(H_2O)_3$

The geometries for complexes **(9)-(11)** are symmetrically equivalent to the Pt-aquo complexes in Chapter 4. The equilibrium bond-lengths are longer(by ~0.03 Å) for Rh complexes however.

The zero-point corrections on the complexes **(9)-(11)** are very similar to that of the Pt-aquo complexes(compare Tables 4.5-4.6 and 6.1).

The Rh-Cl bond trans to a coordinated water (r_c in **(9)** and r_a in **(10)**) is shorter relative to the other Rh-Cl bonds as indicated by XRD measurements, probably due to the larger trans influence of Cl^- relative to water.

The Rh-^{35}Cl bonds extend further than the Rh-^{37}Cl bonds as expected from the effect of anharmonicity.

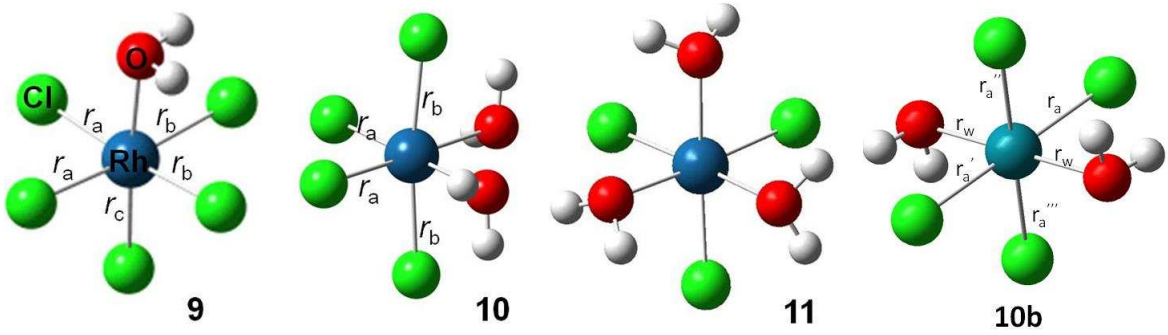

Figure 6.1: Optimized structures of **(9)** $[Rh^{35}Cl_n{}^{37}Cl_{5-n}(H_2O)]^{2-}$ (n=0-5), **(10)** *cis*-$[Rh^{35}Cl_n{}^{37}Cl_{(4-n)}(H_2O)_2]^-$ (n=0-4), **(11)** *fac*-$Rh^{35}Cl_n{}^{37}Cl_{(3-n)}(H_2O)_3$. and **(10b)** *trans*-$[RhCl_4(H_2O)_2]^-$.

Table 6.1: Differences between effective bond distances for **9** to **11** [in Å] calculated at the PBE0/SDD/6-31G* level.

	r^a	r^b	r^c	r^w	$\Delta^{35}r_{eff}{}^a$	$\Delta^{35}r_{eff}{}^b$	$\Delta^{35}r_{eff}{}^c$	$\Delta^{35}r_{eff}{}^w$
9	2.358749	2.437788	2.318817	2.190223	0.004371	0.005158	0.002922	0.015064
10	2.314206	2.364366		2.141847	0.002433	0.004077		0.011705
Exp.[a]	2.2980	2.3407		2.0858				
10b	2.36606			2.075620				
Exp.[b]	2.3571			2.0319				
11	2.299244			2.126453	0.001947			0.011279

[a] From Varshavsky, Yu.S. *et al. Koord.Khim.*(2007) 33, 202. [b]From Thomas, C. K., & Stanko, J. A. (1973) *J. Coord. Chem.*, *2*(3), 211.

Table 6.2: Differences between effective bond distances for **9** to **11** [in Å] calculated at the PBE0/SDD/6-31G* level.

	$^{35}r_{eff}{}^a$	$^{35}r_{eff}{}^b$	$^{35}r_{eff}{}^c$	$^{35}r_{eff}{}^w$	$\Delta^{35}r_{eff}{}^a$-$\Delta^{37}r_{eff}{}^a$	$\Delta^{35}r_{eff}{}^b$-$\Delta^{37}r_{eff}{}^b$	$\Delta^{35}r_{eff}{}^c$-$\Delta^{37}r_{eff}{}^c$	$\Delta^{35}r_{eff}{}^w$-$\Delta^{37}r_{eff}{}^w$
9	2.363120	2.442946	2.321739	2.205287	0.000072	0.000187	0.000350	0.000084
10	2.316639	2.368443		2.153552	0.000026	0.000019		0.000110
11	2.301191			2.137732	0.000042			0.000074

Both the trans and cis isomers of $[RhCl_4(H_2O)_2]^-$ are found as stable crystals as indicated by the XRD data in Table 6.1. The calculated energies for both differ by a mere 0.002 kcal/mol, however, for consistency with the ^{195}Pt system in this study, only the cis isomer, **(10)** is used in the calculation of isotope shifts.

6.2.2 Isotope Shifts

All possible $^{35/37}$Cl isotopomers were calculated in the gas phase for **(9)-(11)**. The resulting vibrationally averaged structures were used as inputs for relativistic calculations of isotropic magnetic shielding constants at the ZORA-SO/PW91/QZ4P/TZ2P level.

To compare with experiment, isotope shifts $\Delta\delta$ were calculated relative to the corresponding all-^{35}Cl isotopologue set to $\delta = 0$. Many of the static isotopomer structures can be interconverted through simple OH rotation about the Rh-O bonds, processes that are expected to occur very rapidly on the NMR time scale as dicussed in 5.2.2. Thus, it is reasonable to assume that those isotopomers that are grouped together in the legends will only show a single NMR signal, and their computed shielding constants were averaged accordingly. As with the Pt homologue **2** (Chapter 4.2), resolution of the isotopomers for the singly or doubly $^{35/37}$Cl

substituted forms of **10** would only be compatible with a cis, not a trans geometry (c.f. B and C in the left middle part of Figure 6.2).

For complex **(9)-(11)**, the resulting shielding constants and the corresponding experimental isotope shifts are collected in Table 6.3 and, after conversion of the computed shieldings into relative shifts, plotted against each other in Figure 6.2. The sign of the experimental isotope shifts has been reversed, so that they appear in the same sequence as in a conventional NMR spectrum.

The overall observed trends as well as the overall order of magnitude of the isotope shifts are reasonably well reproduced by our computational protocol. As found for the Pt complexes in Chapters 4 and 5, however, there are quantitative discrepancies, apparent in a noticeable scatter of the data and a typically overestimated slope of the $\Delta\sigma_{calc}$ vs. $\Delta\delta_{exp}$ data. It is unclear at present whether these discrepancies are due to residual numerical errors in the computations, deficiencies of the overall model (e.g. the neglect of thermal effects beyond the zero-point corrections), or missing solvation.

Compared to the Pt-aquo complexes, there is much more scatter, that may be due to the softer nature of the Rh-L (L=H_2O, Cl^-) bonds, which enhance solvent interaction. The effect is more pronounced with complexes C, F, H and I for **(9)** and F, G and H for **(10)**. Interestingly, these are the isotopomers with a ^{37}Cl trans to a H_2O ligand.

When comparing the isotopomers D and E for complex **(9)**, a number of interesting differences are spotted, however, these species are magnetically equivalent according to experiment. These two isotopomers are not resolved experimentally, but gas-phase computations indicate that they are not magnetically equivalent(see top of Figure 6.3 in following section). Near-degeneracy found experimentally for **(1)**; where calculations found a small difference in isotope shifts between D and E (0.4 ppm, Table 4.7a). For Rh, the distinction is much larger, 1.1 ppm (Table 6.3). For **(9)**, the theoretical results are particularly poor (Figure 6.2a), probably related to the higher negative charge

Overall it appears that the errors in the computations increase with overall (absolute) charge: neutral complexes are described the best **(2, 11)**, followed by singly charged species **(1, 3, 10)**, with the largest deviations found for dianionics **(4-9)**. This could point to missing solvation as the key factor. For **9**, this is probably compounded by the softer nature of the M-OH_2 bond, compared to the M-OH bond in dianionic (**4-8)**.

Table 6.3: Experimental ^{103}Rh chemical shifts[a] and computed isotropic shielding constants for the $^{35/37}$Cl isotopomers and isotopologues of (**9**) – (**11**).

	(9)		(10)		(11)	
	δ_{exp}/ppm	σ_{calc}/ppm	δ_{exp}/ppm	σ_{calc}/ppm	δ_{exp}/ppm	σ_{calc}/ppm
A	8284.13	-8217.05	8535.43	-7139.55	8794.36	-6764.99
B	8283.87	-8216.31	8535.20	-7139.16	8794.05	-6764.78
C	8283.80	-8214.65	8535.10	-7139.34	8793.73	-6764.16
D	8283.62	-8214.58	8534.98	-7140.45	8793.40	-6763.34
E	8283.62	-8215.64	8534.85	-7138.95		
F	8283.53	-8211.92	8534.78	-7139.68		
G	8283.36	-8215.63	8534.66	-7139.64		
H	8283.27	-8211.37	8534.48	-7139.14		
I	8283.27	-8212.13				
J	8282.99	-8215.21				

[a] In the absence of a suitable reference compound, chemical shifts (ppm) are reported to Ξ (^{103}Rh) = 3.16 MHz on the TMS scale at 100.000 MHz, as proposed by Goodfellow[12]; the high-frequency positive-shift convention was used [20].

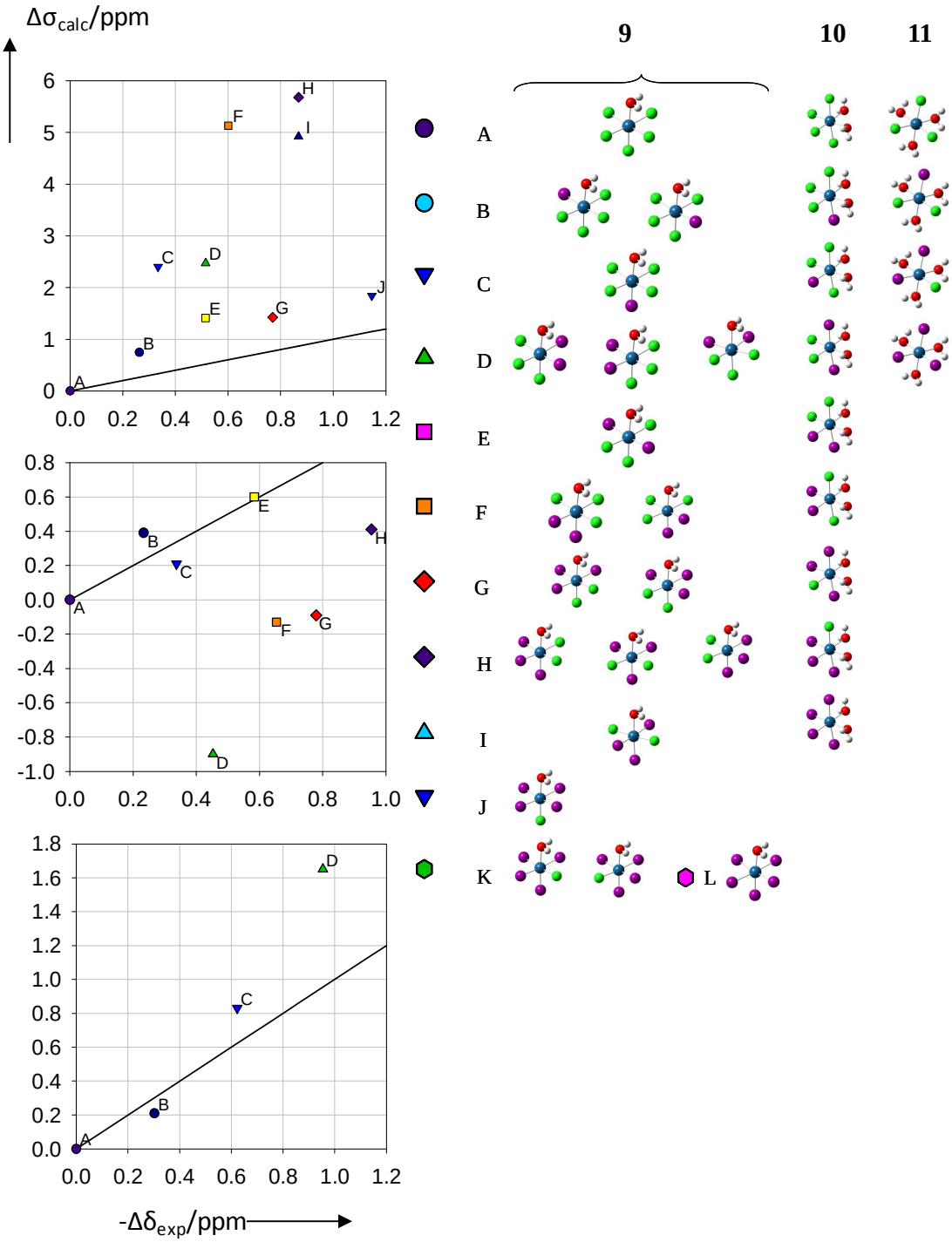

Figure 6.2: Calculated shielding differences vs. negative experimental ^{19} $^{35/37}$Cl isotope shifts of the isotopomers of (top) **(9)** $[Rh^{35}Cl_n{}^{37}Cl_{5-n}(H_2O)]^{2-}$ (n=0-5), (middle) **(10)** *cis*-$[Rh^{35}Cl_n{}^{37}Cl_{(4-n)}(H_2O)_2]^{-}$ (n=0-4), and (bottom) **(11)** *fac*-$Rh^{35}Cl_n{}^{37}Cl_{(3-n)}(H_2O)_3$. The labeling scheme is the same as in Figure 4.3.

6.2.3 Shielding/bond-length derivatives

From the previous chapter, it was shown that the bond length changes due to zero-point vibrations is the dominant factor influencing the isotope shifts. To test the models feasibility for the Rh(III) complexes we used representative shielding/bond-length derivatives $\partial\sigma_{Rh}/\partial r_{RhX}$ (X = O and Cl), together with the computed zero-point corrections for each bond length (Δr_g^0 in eq 1), in order to estimate effective shieldings according to Eq 4.1. These estimated shieldings can then be compared to the actual effective shieldings computed for the actual vibrationally averaged structure. Rh-Cl and Rh-O shielding/bond-length derivatives have been evaluated for **(9)-(11)**, respectively, by rigid scans of the Rh-Cl and Rh-O bonds about their equilibrium values. The resulting $\partial\sigma_{Rh}/\partial r_{RhCl}$ and $\partial\sigma_{Rh}/\partial r_{RhO}$ values are listed in Table 6.4.

Table 6.4: Shielding/bond-length derivatives $\partial\sigma_{Rh}/\partial r_{RhX}$ computed[a] for complexes **9 - 11** at the ZORA-SO/PW91 level.

Compd.	Bond[b]	$\partial\sigma_{Pt}/\partial r_{PtX}$ [ppm/Å]
9	(r_a)Rh-Cl	-3045
	(r_b)Rh-Cl	-5814
	(r_c)Rh-Cl[c]	-3707
	Rh-O	-6500
10	(r_a)Rh-Cl[c]	-4200
	(r_b)Rh-Cl	-5100
	Rh-O	-4400
11	Rh-Cl	-4100
	Rh-O	-3700

[a]Obtained through rigid displacements of the ligands about the equilibrium value of the designated bond, see Figure 4.9 for an example. [b]See Figure 6.1 for definition. [c]trans to water ligand

Figure 6.4 shows the resulting estimated $^{37/35}$Cl isotope effects on the ^{103}Rh shieldings of **(9)-(11)**, plotted vs. the actual computed values.

Compared to the Pt-aquo complexes, the shielding/bond-length derivatives are consistently larger (typically by a factor of 1.5). Taking that into account while considering the enhanced solvent interactions of the Rh(III) complexes (**9)-(11)**, it gives a clue to the origin of the large deviations from experiment.

Compared to the Pt(IV) species discussed previously, the increment system seems to work less well for the Rh(III) complexes, although the order of magnitude of the calculated isotope shifts can still be traced back to that in zero-point corrections to the bond distances (Figure 6.4). Larger discrepancies are found for complexes C, F, H and I for **(9)**, as before these are the isotopomers with a ^{37}Cl trans to a H_2O ligand.

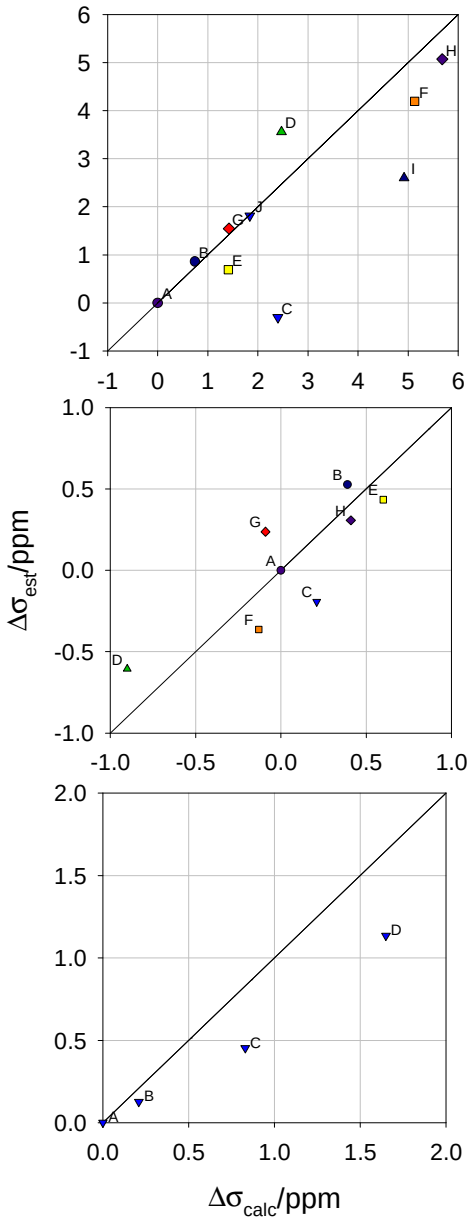

Figure 6.4 Shielding differences in $^{35/37}$Cl isotopomers of (top to bottom) **(9)** – (**11)**, estimated from Eq . 4.1 vs. actual computation from r_g^0 geometries, including the line with unity slope.

6.2.4 Solvation effects

For the *fac*-$[Pt^{35/37}Cl_3(OH_2)_3]^+$ species, immersion in a polar solvent by means of the PCM method, the Pt-O bonds contracted from 2.1367 Å to 2.1027 Å, consistent with a stronger, stiffer bond. This causes the Pt-Cl bonds to elongate from 2.2658 Å to 2.2785 Å which may lead to increased solvent interaction. For *fac*-$RhCl_3(H_2O)_3$, the Rh-O bond contracts from 2.1265 Å to 2.1052 Å, when gong from the gas-phase to the continuum. The Rh-Cl bonds extend further from 2.2992 Å to 2.3082 Å. The ionic radii of Rh(III) and Pt(IV) are 68 pm and 65 pm respectively. Thus, it is reasonable to assume that decreased Columbic potential in M-Cl bonds arising from the larger size and lower formal charge on the Rh(III) centre, would lead to longer , softer M-Cl bonds which would interact with the surrounding polar solvent molecules. The Rh-Cl bond is ~0.03 Å longer in the continuum than the corresponding Pt-Cl bond, suggesting increased interaction with water from the solvent.

As a first step toward such a full description of solvation, we have optimized a microsolvated cluster, namely $[RhCl_5(H_2O)]^{2-}\cdot 2H_2O$. Placing the two extra water molecules such that they each accepts an $OH\cdots OH_2$ hydrogen bond from the coordinated water ligand, the minimum obtained is similar to what has been found for $[PtCl_5(H_2O)]^{-}\cdot 2H_2O$ shown on top of Figure 4.14.

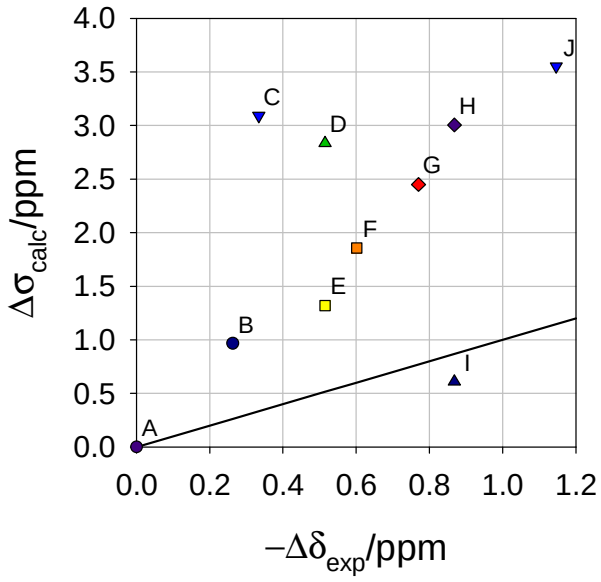

Figure 6.5: Calculated shielding differences vs. negative experimental $^{35/37}Cl$ isotope shifts of the isotopomers of $[RhCl_5(H_2O)]^{2-}\cdot 2H_2O$, including the ideal line with unity slope.

On going from pristine **(9)** to $[RhCl_5(H_2O)]^- \cdot 2H_2O$, the equilibrium Rh-O bond distance decreases from 2.190 Å to 2.148 Å, similar to what is found in a continuum for (e.g. decrease from 2.1265 Å to 2.1052 Å for (**11)**). At the same time, the zero-point correction for the Rh-O distance changes from Δr_g^0 = 0.015 Å (Table 6.1) to 0.013 Å upon microsolvation, consistent with a stronger, stiffer bond.

There is visible improvement in the result for the microsolvated complex, i.e. less scatter and values closer to what has been found experimentally. The slope of the linear trend is still much higher than unity, though, as expected from the neglect of the effect of the solvent on the Rh-Cl bond strength. The deviation from the trend by isotopomer D can be attributed to the isotopic trans influence as discussed in Section 6.2.1. In the fully solvated complex this effect will be minimal, as a consequence D and E will be magnetically equivalent. Isotopomer C is directly influenced by the Rh-O bond contraction upon microsolvation, as the Rh-Cl bond trans to the coordinated water contracts when substituted with ^{37}Cl due to anharmonicity, causing the Rh-O bond to contract by a further 0.00012 Å, due to the isotopic trans influence. In isotopomer I, there is a ^{35}Cl *trans* to another ^{35}Cl; the isotopic trans influence causes these bonds to contract, a similar contraction is found for the Rh-^{37}Cl bonds. The Rh-O and the Rh-Cl bond trans to the coordinated water contracts when substituted with ^{37}Cl due to anharmonicity, causing the Rh-O bond to contract, such that the coordination sphere is contracted to the extent that interaction with water from the solvent is less significant than for the other isotopomers. As mentioned before, this effect is leveled out when the complex is fully solvated.

Shielding/bond-length derivatives have been evaluated in the polarized continuum for **(10)**, by rigid scans of the Rh-Cl and Rh-O bonds about their equilibrium values as shown in Figure 6.6. The resulting $\partial\sigma_{Rh}/\partial r_{RhX}$ values are not much different from what was found in the gas-phase. Immersion in a polarized continuum, increased $\partial\sigma_{Rh}/\partial r_{RhX}$ for Rh-Cl_{eq} from -4200 to −4600 ppm/Å, from Rh-O -4400 to −4200 ppm/Å. The Rh-Cl_{ax} bonds remained unaffected, with $\partial\sigma_{Rh}/\partial r_{RhX}$ = −5100 ppm/Å in both the continuum and gas-phase.

In an attempt to improve on our model, the shielding/bond-length derivatives determined in the polarized continuum was used together with the gas-phase zero-point corrections for the isotopologues and isotopomers of **(2)** to estimate shielding according to the increment method by Eq. 4.1. The result is plotted in Figure 6.7 on the same axis as the gas-phase shieldings

calculated using DFT. Overall, there seems to be no improvement, mainly because bond-length changes are the decisive factor and not the shielding/bond-length derivatives.

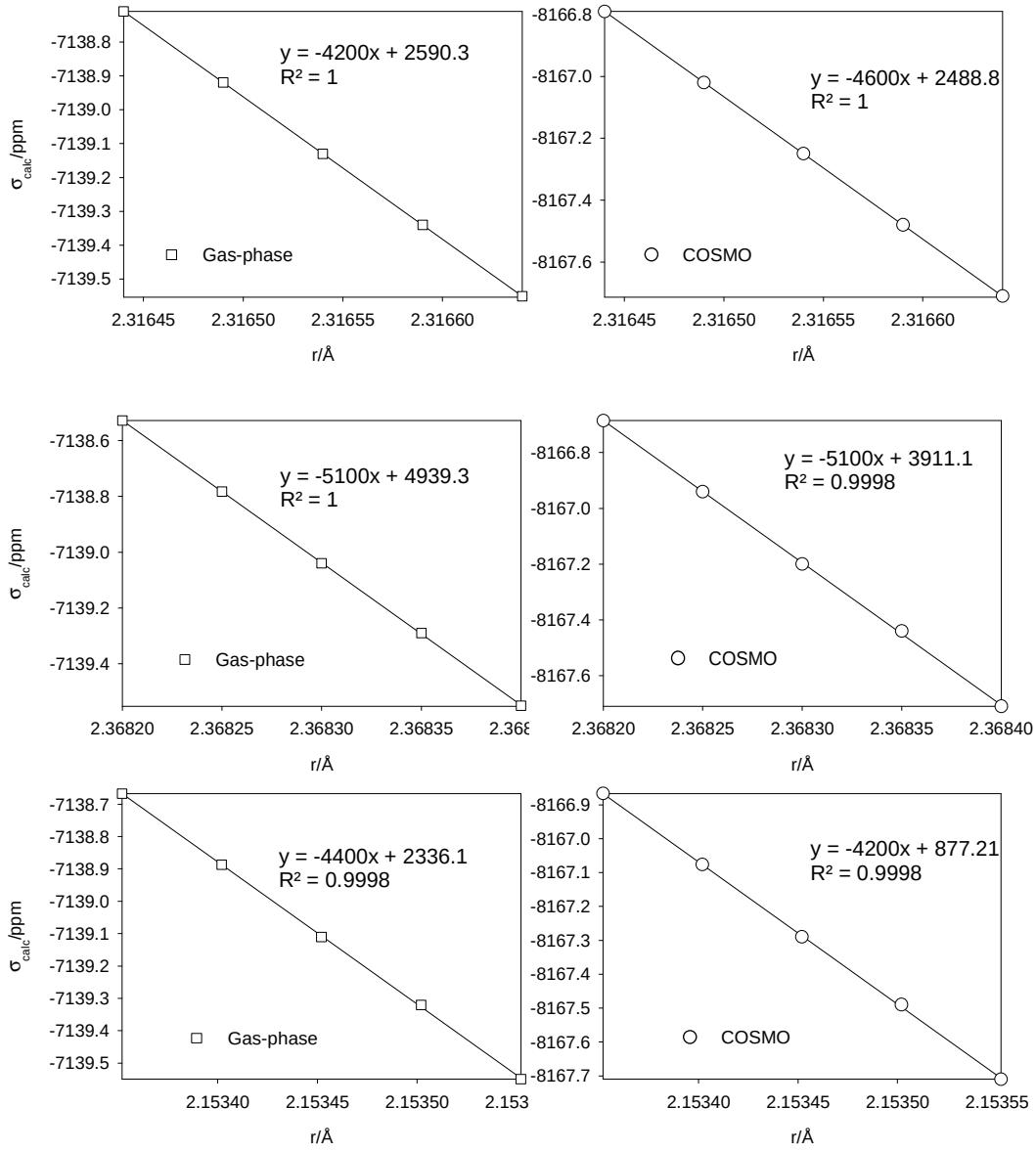

Figure 6.6: Plot of ^{103}Rh magnetic shielding of *cis*-$[RhCl_4(H_2O)_2]^-$ vs. (top) Rh-Cl_{eq}, (middle) Rh-Cl_{ax} and (bottom) Rh-O bond distances, evaluated at the COSMO/ZORA-SO/PW91 level as well as at the ZORA-SO/PW91 level.

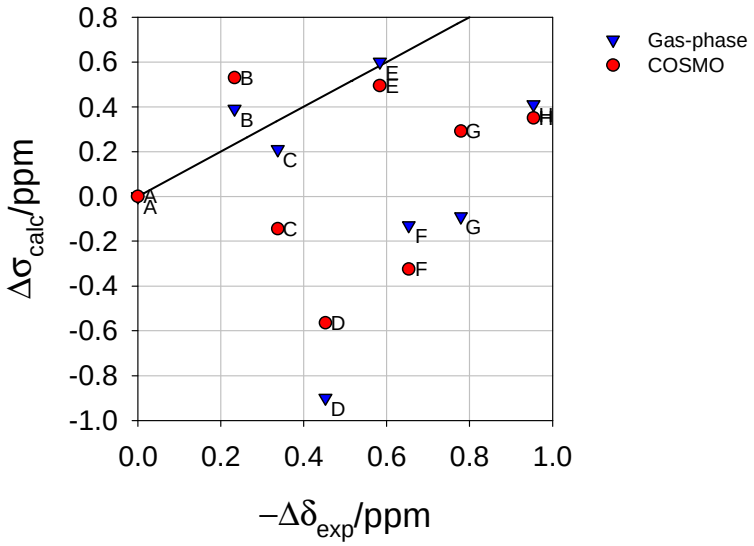

Figure 6.7 Shielding differences in $^{35/37}$Cl isotopomers of **10**, estimated from Eq. 4.1 using $\partial\sigma_{Rh}/\partial r_{RhXi}$ in a polarizable continuum and calculated shielding differences vs. negative experimental $^{35/37}$Cl isotope shifts of the isotopomers of **10**, including the line with unity slope.

6.3 Conclusions

The computational protocol was extended to $[Rh^{35}Cl_n{}^{37}Cl_{5-n}(H_2O)]^{2-}$ (n=0-5), *cis*-$[Rh^{35}Cl_n{}^{37}Cl_{(4-n)}(H_2O)_2]^-$ (n=0-4), and *fac*-$Rh^{35}Cl_n{}^{37}Cl_{(3-n)}(H_2O)_3$ (n=0-3) isotopologues and isotopomers. Even though the Rh(III) aquo system is reasonably similar to the Pt(IV) analogue, it shows poorer agreement with experiment. Except for the dianionic monohydrate **(9)**, the order of magnitude was reproduced but larger scatter was evident, which is probably due to increased solvent interaction. The error inherent from the neglect of the solvent in the computational protocol, is exaggerated by the higher (w.r.t. Pt(IV)) sensitivity towards isotopic substitution seen by the shielding/bond-length derivatives for these complexes.

Chapter 7

Conclusions

We have presented calculations of magnetic shieldings at appropriate DFT levels for the isotopologues and isotopomers of Pt(IV) and Rh(III) complexes obtained from $^{35/37}$Cl or $^{16/18}$O substitution of chlorido, aquo and hydroxido ligands. At the PBE0/ECP1 level, effective geometries, r_g^0 at 0 K were constructed in a perturbational approach from the equilibrium geometries r_e, the (mass-dependent) harmonic frequencies ω_e, and the cubic force field $V^{(3)}$[97]. For r_g^0 geometries of each isotopic substitution, ^{195}Pt and ^{103}Rh shielding tensors were computed at the relativistic spin-orbit ZORA level, using the GGA PW91[66c, 104] functional, together with a locally dense basis of QZ4P quality on Pt and Rh. The integration precision parameter was set to 10.0. These calculations employed the ADF2010.02 program.[108]
The ^{195}Pt and ^{103}Rh NMR nuclear shieldings computed for these species reproduce the order of magnitude of the observed effect reasonably well, up to ca. 1 ppm as shown in Figure 7.1.

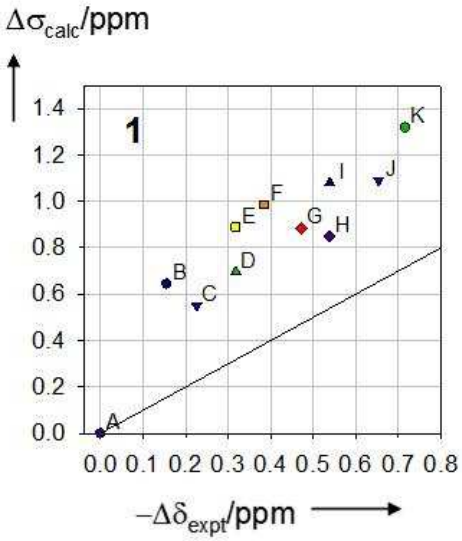

Figure 7.1 Calculated ^{195}Pt shielding differences vs. negative experimental $^{35/37}$Cl isotope shifts of the isotopomers of $[PtCl_5(H_2O)]^-$, including the ideal line with unity slope.

In most cases, general trends are also captured qualitatively, thus providing the first theoretical basis for the origin of subtle isotope shifts in ^{195}Pt and ^{103}Rh NMR spectra. NMR was shown to be able to detect bond-length changes upon isotopic substitution on the femtometer scale.

The computed isotope shifts can be tracked back to bond-length changes via an increment method and Eq. 4.1 as shown in Figure 5.9.

$$\sigma^{0}_{g,est} = \sigma_e + \sum_{i=1}^{6} \Delta r^{0}_{g,i} \frac{\partial \sigma_{Pt}}{\partial r_{PtX,i}} \quad \ldots(4.1)$$

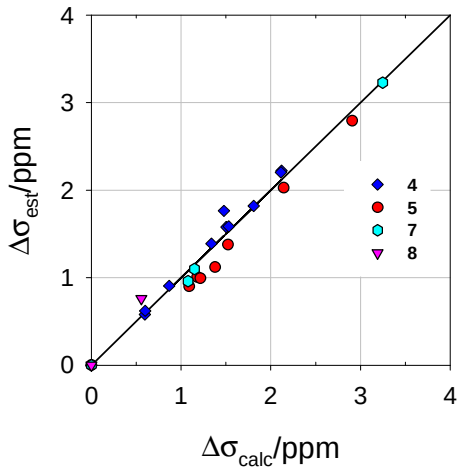

Figure 5.9 Shielding differences in $^{35/37}$Cl isotopomers of **(4)** $[PtCl_5(OH)]^{2-}$, **(5)** *cis*-$[PtCl_4(OH)_2]^{2-}$, **(7)** *cis*-$[PtCl_2(OH)_4]^{2-}$, **(8)** $[PtCl(OH)_5]^{2-}$, estimated from eq 4.1 vs. actual computation from r_g^0 geometries, including the line with unity slope.

It was shown that the hydroxido ligands can rotate spontaneous and rapidly (on the NMR time-scale) about the M-O bond by investigating the interconversion of two degenerate Pt(IV) rotamers(See Figure 5.2), indicating that observed chemical shifts are essentially averaged between rotamers.

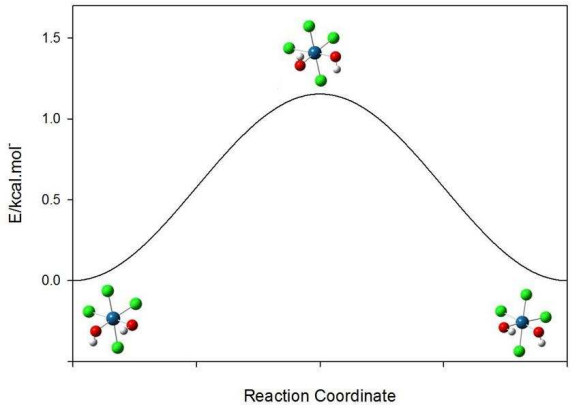

Figure 5.2: Energy profile of *cis*-$[PtCl_4(OH)_2]^{2-}$. The minima obtained interconvert via the transition state shown at the maximum.

Agreement with experiment tends to decrease with increasing charge on the complex. Neglect of solvation appears to be the critical factor. For the Rh complexes, the error inherent from the

neglect of the solvent in the computational protocol, is inflated by the higher (relative to Pt(IV)) sensitivity towards isotopic substitution seen by the shielding/bond-length derivatives calculated for these complexes.

A possible explanation based on the computed shielding/bond-length derivative was proposed for why isotopomers are not detected experimentally in some cases. Using the polarized continuum model to calculate shielding/bond-length derivatives together with gas-phase zero-point corrections to estimate shieldings, it was shown that the contraction of the coordination sphere in the hydroxide complexes cause the Pt-Cl bonds to become magnetically equivalent. This was not the case for the aquo complexes, yielding experimentally resolvable isotopomers. The isotopic trans-influence is responsible for bond-displacements on the femtometer scale, significant in the gas-phase, considering that bond-displacements of neighbouring isotopomers differ by femtometers. This effect seems to dissolve upon immersion in a polar solvent, as the M-L bonds, M-OH_2 in particular, become much stronger and stiffer, effectively rendering isotopomers unresolvable in some cases.
Unfortunately, neither simple polarizable continuum models nor small, microsolvated complexes lead to improved isotope shifts for the series investigated. Apparently, in our microsolvated complexes the distinction between *cis* and *trans* chloride ligands is overestimated to a large extent, consistent with the fact that only the former interact with the extra water molecules, not the latter. Many more water molecules would have to be added, eventually necessitating a dynamical description (CPMD or QM/MM) and exceeding the scope of this study.

Besides such solvation effects, there could be other methodological shortcomings in our model that might compromise the accuracy of the results. As has been shown in a recent study of ^{199}Hg shieldings of small Hg(II) species, the ZORA-SO method does not accurately reproduce full four-component relativistic results and even the QZ4P basis set in ADF may not be fully saturated for this purpose.[46] Also, we are only evaluating shieldings at instantaneous r_g^0 (or r_{eff}) structures, ignoring effects from a possible curvature of the shielding hypersurface about this structure. While such effects tend to be small, they can be noticeable if high accuracy is sought.[97, 114] For both Pt(IV) and Rh(III) thermal effects have been neglected, as only the vibrational ground state at 0 K was calculated. Heavy nuclei inherently have more closely spaced vibrational energy levels, occupation of these is governed by a Boltzmann distribution at a given temperature. We tacitly assume that all these effects, noticeable as they would be

for the absolute shielding constants, are transferable enough between different molecules (or isotopomers), so that they cancel to a large extent in the relative (i.e. isotope) shifts. Proper convergence of all these issues (i.e. computation of fully relativistic potential energy and shielding hypersurfaces at the basis-set limit) is, arguably, a formidable task. In light of the results discussed above in this section we believe that proper inclusion of solvent effects may be rather more important.

The relativistic treatment of heavy nuclei and the addition of zero-point corrections have enhanced the use of NMR, rendering it a powerful structural tool. Often candidates differing in constitution or conformation can be distinguished based on the accord between computed and experimental chemical shifts.[115] Now, theoretical modeling of structural effects on NMR parameters extends to the smallest scale, distance changes of a few femtometers upon isotopic substitution.

Bibliography

1. (a) Pregosin, P. S., *Trans. Metal Nucl. Magn. Reson.* 1991; (b) Priqueler, J. R. L.; Butler, I. S.; Rochon, F. D., *Appl. Spectrosc. Rev.* **2006,** *41*, 185; (c) Still, B. M.; Kumar, P. G. A.; Aldrich-Wright, J. R.; Price, W. S., *Chem. Soc. Rev.* **2007,** *36*, 665.
2. Murray, P.; Gerber, W. J.; Koch, K. R., *Dalt. Trans.* **2012,** *41* (35), 10533.
3. Keeler, J., *Understanding NMR spectroscopy*. Wiley, New York: 2011.
4. Burger, M. R.; Kramer, J.; Chermette, H.; Koch, K. R., *Magn. Reson. Chem.* **2010,** *48 Suppl 1*, S38.
5. (a) Nama, D.; Anil Kumar, P. G.; Pregosin, P. S., *Magn. Reson.. Chem.* **2005,** *43* (3), 246; (b) Naidoo, K. J.; Lopis, A. S.; Westra, A. N.; Robinson, D. J.; Koch, K. R., *J. Am. Chem. Soc.* **2003,** *125* (44), 13330.
6. Autschbach, J.; Le Guennic, B., *Chem. Eur. J.* **2004,** *10*, 2581.
7. Autschbach, J.; Le Guennic, B., *J. Am. Chem. Soc.* **2003,** *125* (44), 13585.
8. Appleton, T. G.; Hall, J. R.; Ralph, S. F., *Inorg. Chem.* **1985,** *24*, 4685.
9. Zelewsky, A. V., *Helv. Chim. Acta* **1968,** *51* (4), 803.
10. Mason, J. J. P. a. W. R., *J. Mag. Reson.* **1977,** (25), 519.
11. Kerrison, S. J. S. S., P. J. , *J. Mag. Reson.* **1978,** (31), 321.
12. Carr, C.; Goggin, P. L.; Goodfellow, R. J., *Inorg. Chim. Acta* **1984,** *81* (0), L25.
13. (a) McFarlene, H. C. E.; McFarlane, W.; Rycroft, D. S., *J. Chem. Soc., Dalt. Trans.* **1976,** (16), 1616; (b) Bendall, M.; Doddrell, D., *Australian J. Chem.* **1978,** *31* (5), 1141; (c) Näumann, F.; Rehder, D.; Pank, V., *J. Organometallic Chem.* **1982,** *240* (4), 363; (d) Hoch, M.; Rehder, D., *Inorg. Chim. Acta* **1986,** *111* (1), L13.
14. Jameson, CJ; Osten, H-J., *Annu. Rep. NMR Spectrosc.* **1986,** *17*, 1.
15. Groening, O.; Elding, L. I., *Inorg. Chem.* **1989,** *28* (17), 3366.
16. Ismail, I. M.; Kerrison, S. J. S.; Sadler, P. J., *J. Chem. Soc., Chem. Comm.* **1980,** (23), 1175.
17. Gerber, W. J.; Murray, P.; Koch, K. R., *Dalt. Trans.* **2008,** (31), 4113.
18. Engelbrecht, L. A., *A study of isotope-effects in high-resolution ^{195}Pt NMR spectra of octahedral complexes of the type $[PtCl_{6-n}(OH)_n]^{2-}$, n = 0-6, in water*, *MSc thesis*, Stellenbosch, **2013**.
19. Geswindt, T. E.; Gerber, W. J.; Brand, D. J.; Koch, K. R., *Anal. Chim. Acta* **2012,** *730* (0), 93.
20. Ernsting, J. M.; Gaemers, S.; Elsevier, C. J., *Mag. Reson. Chem.* **2004,** *42* (9), 721.

21. Carr, C.; Glaser, J.; Sandström, M., *Inorg Chim. Acta* **1987,** *131* (2), 153.

22. (a) Jameson, C. J.; Jameson, A. K., *J. Chem. Phys.* **1986,** *85* (10), 5484; (b) Jameson, C. J.; Jameson, A. K.; Oppusunggu, D., *J. Chem. Phys.* **1986,** *85*, 5480; (c) Jameson, C. J.; Rehder, D.; Hoch, M., *J. Am. Chem. Soc.* **1987,** *109*, 2589.

23. Bühl, M., *Annu. Rep. NMR Spectrosc.* **2008,** *64*, 77.

24. (a) Sterzel, M.; Autschbach, J., *Inorg. Chem.* **2006,** *45*, 3316; (b) Autschbach, J.; Zheng, S. H., *Magn. Reson. Chem.* **2008,** *46*, S45.

25. Bühl, M., *Chem. Phys. Lett* **1997,** *267* (3), 251.

26. Schreckenbach, G., *J. Chem. Phys.***1999,** *110* (24), 11936.

27. Wilson, P. J.; Amos, R. D.; Handy, N. C., *Chem. Phys. Lett.***1999,** *312* (5), 475.

28. Bühl, M.; Gaemers, S.; Elsevier, C. J., Chem. Eur. J. **2000,** *6* (17), 3272.

29. Bühl, M., *Theoretical Chemistry Accounts: Theory, Computation, and Modeling (Theoretica Chimica Acta)* **2002,** *107* (6), 336.

30. Bühl, M.; Mauschick, F. T., *Magn. Reson. Chem.* **2004,** *42* (9), 737.

31. Bühl, M., Chem. Eur. J. **1999,** *5* (12), 3514.

32. (a) Zhou, P.; Au-Yeung, S. C. F.; Xu, X. P., *J. Am. Chem. Soc.* **1999,** *121* (5), 1030; (b) Gao, Y.; Zhou, L., *Theor. Chem. Acc.* **2009,** *123*, 455.

33. (a) Bagno, A.; Bonchio, M., *Chem. Phys. Lett.* **2000,** *317* (1), 123; (b) Bagno, A.; Bonchio, M., *Eur. J. Inorg. Chem.* **2002,** *2002* (6), 1475.

34. Bühl, M.; Baumann, W.; Kadyrov, R.; Börner, A., *Helv. Chim. Acta* **1999,** *82* (6), 811.

35. (a) Donkervoort, J. G.; Bühl, M.; Ernsting, J. M.; Elsevier, C. J., *Eur. J. Inorg. Chem.* **1998,** *1999* (1), 27; (b) Leitner, W.; Bühl, M.; Fornika, R.; Six, C.; Baumann, W.; Dinjus, E.; Kessler, M.; Krüger, C.; Rufinska, A., *Organometallics* **1999,** *18* (7), 1196.

36. (a) Bühl, M., *J. Inorg. Biochem.* **2000,** *80* (1–2), 137; (b) Bühl, M., *J. Comp. Chem.* **1999,** *20* (12), 1254.

37. Sanders, L. K.; Arnold, W. D.; Oldfield, E., *J. Porphyrins and Phthalocyanines* **2001,** *05* (03), 323.

38. Bühl, M.; Håkansson, M.; Mahmoudkhani, A. H.; Öhrström, L., *Organometallics* **2000,** *19* (26), 5589.

39. (a) Bühl, M., *Angew. Chem. Int. Ed.* **1998,** *37* (1-2), 142; (b) Bühl, M., *Organometallics* **1999,** *18* (24), 4894; (c) Bühl, M.; Mauschick, F. T., *Organometallics* **2003,** *22* (7), 1422.

40. Bühl, M.; Kaupp, M.; Bühl, M.; Malkin, V. G., *Calculation of NMR and EPR Parameters. Theory and Applications*. 2004, Wiley-VCH, Weinheim.

41. Bühl, M.; Parrinello, M., *Chem. Eur. J.* **2001,** *7* (20), 4487.

42. Bühl, M., *J. Phys. Chem. A* **2002,** *106* (44), 10505.

43. (a) Bühl, M.; Mauschick, F. T.; Terstegen, F.; Wrackmeyer, B., Angew. *Chem. Int. Ed* **2002,** *41* (13), 2312; (b) Bühl, M.; Mauschick, F. T., *Phys. Chem. Chem. Phys.* **2002,** *4* (22), 5508.

44. (a) Wan, J.; Fukuda, R.; Hada, M.; Nakatsuji, H., *J. Phys. Chem. A* **2001,** *105* (1), 128; (b) Fukuda, R.; Hada, M.; Nakatsuji, H., *J. Chem. Phys.* **2003,** *118*, 1027.

45. (a) Autschbach, J.; Zheng, S., *Annu. Rep. NMR Spectrosc.* **2009,** *67*, 1; (b) de Dios, A. C.; Jameson, C. J., Chapter One - Recent Advances in Nuclear Shielding Calculations. In *Annu. Rep. NMR Spectrosc.*, Graham, A. W., Ed. Academic Press: 2012; 77, 1.

46. Arcisauskaite, V.; Melo, J. I.; Hemmingsen, L.; Sauer, S. P. A., *J. Chem. Phys.* **2011,** *135*, 044306.

47. Melo, J. I.; Maldonado, A.; Aucar, G. A., *Theor. Chim. Acta* **2011,** *129* (3), 483.

48. Krykunov, M.; Ziegler, T.; van Lenthe, E., *J. Phys. Chem. A* **2009,** *113*, 11495.

49. Dmitrenko, O.; Bai, S.; Dybowski, C., *Solid State Nucl. Magn.* **2008,** *34* (3), 186.

50. Bagno, A.; Bini, R., *Angew. Chem. Int. Ed.* **2010,** *49* (6), 1083.

51. Nakanishi, W.; Hayashi, S.; Katsura, Y.; Hada, M., *J. Phys. Chem. A* **2011,** *115* (31), 8721.

52. Wren, J. E. C.; Schreckenbach, G., *Can. J. Chem.* **2009,** *87* (10), 1436.

53. Neto, A. C.; Ducati, L. C.; Rittner, R.; Tormena, C. F.; Contreras, R. H.; Frenking, G., *J. Chem. Theory Comput.* **2009,** *5* (9), 2222.

54. Standara, S.; Maliňáková, K.; Marek, R.; Marek, J.; Hocek, M.; Vaara, J.; Straka, M., *Phys. Chem. Phys.* **2010,** *12* (19), 5126.

55. Autschbach, J.; Sutter, K.; Truflandier, L. A.; Brendler, E.; Wagler, J., *Chem. Eur. J.* **2012,** *18* (40), 12803.

56. Bagno, A.; Saielli, G., *Phys. Chem. Phys.* **2011,** *13* (10), 4285.

57. Saielli, G.; Bini, R.; Bagno, A., *Theor. Chim. Acta* **2012,** *131* (3), 1.

58. (a) Grigoleit, S.; Bühl, M., *J. Chem. Theory Comput.* **2005,** *1*, 181; (b) Bühl, M.; Grigoleit, S.; Kabrede, H.; Mauschick, F. T., *Chem. Eur. J.* **2006,** *12*, 477.

59. Koch, K. R.; Burger, M. R.; Kramer, J.; Westra, A. N., *Dalton Trans.* **2006**, 3277.

60. Cramer, C. J., *Essentials of computational chemistry: theories and models*. Wiley, Chichester, 2004.

61. Koch, W.; Holthausen, M. C.; Holthausen, M. C., *A chemist's guide to density functional theory*. Wiley-Vch Weinheim: 2001; Vol. 2.

62. Neese, F., *Coord. Chem. Rev.* **2009,** *253* (5), 526.

63. Hohenberg, P.; Kohn, W., *Phys. Rev.* **1964,** *136*, 864.

64. (a) Thomas, L. H. In *The calculation of atomic fields*, Mathematical Proceedings of the Cambridge Philosophical Society, Cambridge Univ Press: 1927; pp 542-548; (b) Fermi, E., *Atti Accad. Nazl. Lincei* **1927,** *6*, 602.

65. Kohn, W., *Phys. Rev. A* **1965,** *1133*, 140.

66. (a) Slater, J. C., *The self-consistent field for molecules and solids*. McGraw-Hill: 1974; Vol. 4; (b) Vosko, S. H.; Wilk, L.; Nusair, M., *Can. J. Phys.* **1980,** *58*, 1200; (c) Perdew, J. P.; Wang, Y., *Phys. Rev. B* **1992,** *45*, 13244.

67. Becke, A. D., *Phys. Rev. A* **1988,** *38*, 3098.

68. Lee, C.; Yang, W.; Parr, R. G., *Phys. Rev. B* **1988,** *37*, 785.

69. Perdew, J. P., *Phys. Rev. B* **1986,** *33*, 8822.

70. Dykstra, C.; Frenking, G.; Kim, K.; Scuseria, G., *Theory and Applications of Computational Chemistry: the first forty years*. Elsevier Science: **2005**.

71. Becke, A. D., *J. Chem. Phys.* **1993,** *98*, 5648.

72. Stephens, P. J.; Devlin, F. J.; Chablowski, C. F.; Frisch, M. J., *J. Phys. Chem.* **1994,** *98*, 11623.

73. (a) Grimme, S., *J. Comput. Chem.* **2006,** *27* (15), 1787; (b) Kozuch, S.; Martin, J. M. L., *Phys. Chem. Phys.* **2011,** *13* (45), 20104; (c) Dewar, M. J. S.; Thiel, W., *J. Am. Chem. Soc.* **1977,** *99* (15), 4899.

74. Liakos, D. G.; Neese, F., *J. Chem. Theory Comput.* **2011,** *7* (5), 1511.

75. (a) Ditchfield, R.; Hehre, W. J.; Pople, J. A., *J. Chem. Phys.* **1971,** *54*, 724; (b) Hehre, W. J.; Ditchfield, R.; Pople, J. A., *J. Chem. Phys.* **1972,** *56*, 2257.

76. Hariharan, P. C.; Pople, J. A., *Theor. Chim. Acta* **1973,** *28*, 213.

77. Clark, T.; Chandrasekhar, J.; Spitznagel, G.; Schleyer, P., *J. Comp. Chem.* ***1983,*** *4, 294*.

78. Kaupp, M.; Malkin, V. G.; Malkina, O. L.; Salahub, D. R., *Chem. Phys. Lett.* **1995,** *235* (3), 382.

79. Pyykko, P., *Chem. Rev.* **1988,** *88* (3), 563.

80. Jensen, F., *Introduction to computational chemistry*. Wiley, Chichester, 2007.

81. Beiser, A., *Concepts of modern physics*. McGraw-Hill, 1995.

82. van Lenthe, E.; Baerends, E. J.; Snijders, J. G., *J. Chem. Phys.* **1993,** *99*, 4597.

83. Köppel, H.; Domcke, W., *PVR Schleyer, PVR, Ed* **1998**, 3166.

84. (a) Boese, A. D.; Oren, M.; Atasoylu, O.; Martin, J. M. L.; Kallay, M.; Gauss, J., *J. Chem. Phys.* **2004,** *120* (9), 4129; (b) Bomble, Y. J.; Vazquez, J.; Kallay, M.; Michauk, C.; Szalay, P. G.; Csaszar, A. G.; Gauss, J.; Stanton, J. F., *J. Chem. Phys.* **2006,** *125* (6), 064108; (c) Csaszar, A. G.; Allen, W. D.; Schaefer Iii, H. F., *J. Chem. Phys.* **1998,** *108* (23), 9751; (d) Feller, D.; Dixon, D. A., *J. Chem. Phys.* **2001,** *115* (8), 3484; (e) Feller, D.; Peterson, K. A.; Crawford, T. D., *J. Chem. Phys.* **2006,** *124* (5), 054107; (f) Hirata, S.; Yanai, T.; de Jong, W. A.; Nakajima, T.; Hirao, K., *J. Chem. Phys.* **2004,** *120* (7), 3297; (g) Kenny, J. P.; Allen, W. D.; Schaefer Iii, H. F., *J. Chem. Phys.* **2003,** *118* (16), 7353; (h) Martin, J. M. L.; de Oliveira, G., *J. Chem. Phys.* **1999,** *111* (5), 1843; (i) Schuurman, M. S.; Muir, S. R.; Allen, W. D.; Schaefer Iii, H. F., *J. Chem. Phys.* **2004,** *120* (24), 11586; (j) Tajti, A.; Szalay, P. G.; Csaszar, A. G.; Kallay, M.; Gauss, J.; Valeev, E. F.; Flowers, B. A.; Vazquez, J.; Stanton, J. F., *J. Chem. Phys.* **2004,** *121* (23), 11599.

85. (a) Ruud, K.; Astrand, P.; Taylor, P. R., *J. Chem. Phys.* **2000,** *112*, 2668; (b) Bühl, M.; Imhof, P.; Repisky, M., *Chemphyschem* **2004,** *5*, 414.

86. Sundholm, D.; Gauss, J.; Schafer, A., *J. Chem. Phys.***1996,** *105* (24), 11051.

87. Sundholm, D.; Gauss, J., *Mol. Phys.* **1997,** *92* (6), 1007.

88. Standara, S.; Kulhánek, P.; Marek, R.; Horníček, J.; Bouř, P.; Straka, M., *Theor. Chim. Acta* **2011,** *129* (3), 677.

89. (a) Pfrommer, B. G.; Mauri, F.; Louie, S. G., *J. Am. Chem. Soc.* **2000,** *122* (1), 123; (b) Sebastiani, D.; Parrinello, M., *Chemphyschem* **2002,** *3* (8), 675.

90. Bagno, A.; D'Amico, F.; Saielli, G., *Chemphyschem* **2007,** *8* (6), 873.

91. Bagno, A.; Rastrelli, F.; Saielli, G., *J. Org. Chem.* **2007,** *72* (19), 7373.

92. Jameson, C. J.; Stueber, D., *J. Chem. Phys.***2004,** *120* (21), 10200.

93. Komin, S.; Gossens, C.; Tavernelli, I.; Rothlisberger, U.; Sebastiani, D., *J. Phys Chem. B* **2007,** *111* (19), 5225.

94. Sebastiani, D.; Rothlisberger, U., *J. Phys Chem. B* **2004,** *108* (9), 2807.

95. Truflandier, L. A.; Sutter, K.; Autschbach, J., *Inorg. Chem.* **2011,** *50* (5), 1723.

96. (a) Malkin, V. G.; Malkina, O. L.; Steinebrunner, G.; Huber, H., *Chem. Eur. J.* **1996,** *2* (4), 452; (b) Pfrommer, B. G.; Mauri, F.; Louie, S. G., *J. Am. Chem. Soc.* **1999,** *122* (1), 123.

97. (a) Barone, V., *J. Chem. Phys.* **2005,** *122*, 014108; (b) Barone, V., *J. Chem. Phys.* **2004,** *120*, 3059; (c) Ruud, K.; Åstrand, P. O.; Taylor, P. R., *J. Chem. Phys.* **2000,** *112*, 2668; (d) Ruud, K.; Åstrand, P. O.; Taylor, P. R., *J. Am. Chem. Soc.* **2001,** *123*, 4826; (e) Ruden, T.; Lutnæss, O. B.; Helgaker, T., *J. Chem. Phys.* **2003,** *118*, 9572.

98. McWeeny, R. *Phys. Rev.*, 126 **1962** 1028.

99. Ditchfield, R. *Mol. Phys.* **1974,** *27*, 789.

100. Adiga, S.; Aebi, D.; Bryce, D. L., *Can. J. Chem.* **2007,** *85* (7-8), 496.

101. (a) Perdew, J. P.; Burke, K.; Ernzerhof, M., *Phys. Rev. Lett.* **1996,** *77*, 3865; (b) Adamo, C.; Barone, V., *J. Chem. Phys.* **1999,** *110*, 6158.

102. Dolg, M.; Wedig, U.; Stoll, H.; Preuss, H., *J. Chem. Phys.* **1987,** *86*, 866.

103. Bühl, M.; Reimann, C.; Pantazis, D. A.; Bredow, T.; Neese, F., *J. Chem. Theory Comput.* **2008,** *4*, 1449.

104. Perdew, J. P.; Ziesche, P.; Eischrig, H., *Electr. Struct. Solids*. 1991.

105. (a) Barone, V.; Cossi, M., *J. Phys. Chem. A* **1998,** *102*, 1995; (b) Cossi, M.; Rega, N.; Scalmani, G.; Barone, V., *J. Comput. Chem.* **2003,** *24*, 669.

106. Frisch, M. J.; Trucks, G. W.; Schlegel, H. B.; Scuseria, G. E.; Robb, M. A.; Cheeseman, J. R.; Scalmani, G.; Barone, V.; Mennucci, B.; Petersson, G. A.; Nakatsuji, H.; Caricato, M.; Li, X.; Hratchian, H. P.; Izmaylov, A. F.; Bloino, J.; Zheng, G.; Sonnenberg, J. L.; Hada, M.; Ehara, M.; Toyota, K.; Fukuda, R.; Hasegawa, J.; Ishida, M.; Nakajima, T.; Honda, Y.; Kitao, O.; Nakai, H.; Vreven, T.; Montgomery, J. A.; Peralta, J. E.; Ogliaro, F.; Bearpark, M.; Heyd, J. J.; Brothers, E.; Kudin, K. N.; Staroverov, V. N.; Kobayashi, R.; Normand, J.; Raghavachari, K.; Rendell, A.; Burant, J. C.; Iyengar, S. S.; Tomasi, J.; Cossi, M.; Rega, N.; Millam, J. M.; Klene, M.; Knox, J. E.; Cross, J. B.; Bakken, V.; Adamo, C.; Jaramillo, J.; Gomperts, R.; Stratmann, R. E.; Yazyev, O.; Austin, A. J.; Cammi, R.; Pomelli, C.; Ochterski, J. W.; Martin, R. L.; Morokuma, K.; Zakrzewski, V. G.; Voth, G. A.; Salvador, P.; Dannenberg, J. J.; Dapprich, S.; Daniels, A. D.; Farkas, Ö.; Foresman, J. B.; Ortiz, J. V.; Cioslowski, J.; Fox, D. J., *Gaussian 09*. 2009.

107. Steinborn, D.; Gravenhorst, O.; Hartung, H.; Baumeister, U., *Inorg. Chem.* **1997,** *36* (10), 2195.

108. Baerends, E. J.; Ziegler, T.; Autschbach, J.; Bashford, D.; Bérces, A.; Bickelhaupt, F. M.; Bo, C.; Boerrigter, P. M.; Cavallo, L.; Chong, D. P.; Deng, L.; Dickson, R. M.; Ellis, D. E.; van Faassen, M.; Fan, L.; Fischer, T. H.; Fonseca Guerra, C.; Ghysels, A.; Giammona, A.; van Gisbergen, S. J. A.; Götz, A. W.; Groeneveld, J. A.; Gritsenko, O. V.; Grüning, M.; Gusarov, S.; Harris, F. E.; van den Hoek, P.; Jacob, C. R.; Jacobsen, H.; Jensen, L.; Kaminski, J. W.; van Kessel, G.; Kootstra, F.; Kovalenko, A.; Krykunov, M. V.; van Lenthe, E.; McCormack, D. A.; Michalak, A.; Mitoraj, M.; Neugebauer, J.; Nicu, V. P.; Noodleman, L.; Osinga, V. P.; Patchkovskii, S.; Philipsen, P. H. T.; Post, D.; Pye, C. C.; Ravenek, W.; Rodríguez, J. I.; Ros, P.; Schipper, P. R. T.; Schreckenbach, G.; Seldenthuis, J. S.; Seth, M.; Snijders, J. G.; Solà, M.; Swart, M.; Swerhone, D.; te Velde, G.; Vernooijs, P.; Versluis, L.;

Visscher, L.; Visser, O.; Wang, F.; Wesolowski, T. A.; van Wezenbeek, E. M.; Wiesenekker, G.; Wolff, S. K.; Woo, T. K.; Yakovlev, A. L. *ADF2010*.

109. Orian, L.; Bisello, A.; Santi, S.; Ceccon, A.; Saielli, G., *Chem. Eur. J.* **2004,** *10* (16), 4029.

110. Elder, R. C.; Heeg, M. J.; Payne, M. D.; Trkula, M.; Deutsch, E., *Inorg. Chem.* **1978,** *17* (2), 431.

111. Autschbach, J.; Zheng, S., *Magn. Reson. Chem.* **2008,** *46 Suppl 1*, S45.

112. Bühl, M.; Sieffert, N.; Chaumont, A.; Wipff, G., *Inorg. Chem.* **2011,** *50*, 299.

113. Grigoleit, S.; Bühl, M., *Chem. Eur. J.* **2004,** *10* (21), 5541.

114. Wigglesworth, R. D.; Raynes, W. T.; Kirpekar, S.; Oddershede, J.; Sauer, S. P. A., *J. Chem. Phys.* **2000,** *112*, 736.

115. Bühl, M.; van Mourik, T., *WIREs Comput. Mol. Sci.* **2011,** *1* (4), 634.

Appendix A

Table A.1: Vibrationally averaged bond-lengths at 0K for the $^{35/37}Cl$ isotopologues and isotopomers of $[PtCl_5(H_2{}^{16}O)]^-$ calculated at the PBE0/SDD/6-31G* level [in Å].

Bond[a]	Isotopologue/Isotopomer[b]											
	A	B	C	D	E	F	G	H	I	J	K	L
r^o	2.166823	2.166814	2.166855	2.166812	2.166818	2.166828	2.166816	2.166728	2.166831	2.166828	2.166828	2.166843
r^b	2.376545	2.376443	2.376524	2.376560	2.376548	2.376535	2.376222	2.376417	2.376227	2.376390	2.376217	2.376391
r^a	2.339531	2.339499	2.339541	2.339561	2.339405	2.339595	2.339627	2.339596	2.339728	2.339525	2.339624	2.339529
r^b	2.376558	2.376564	2.376538	2.376573	2.376245	2.376474	2.376564	2.376420	2.376567	2.376403	2.376572	2.376404
r^a	2.339536	2.339594	2.339545	2.339566	2.339731	2.339507	2.339446	2.339583	2.33942	2.339528	2.339453	2.339532
r^c	2.283269	2.283213	2.283142	2.283246	2.283228	2.283159	2.283234	2.283191	2.283173	2.283232	2.283182	2.283203
r^o		2.166811		2.166715		2.166818	2.166916	2.166839			2.166923	
r^b		2.376605		2.376413		2.376611	2.376425	2.376188			2.376413	
r^a		2.339532		2.339597		2.339540	2.339478	2.339595			2.339483	
r^b		2.376188		2.376416		2.376182	2.376476	2.376605			2.376480	
r^a		2.339612		2.339583		2.339608	2.339524	2.339549			2.339536	
r^c		2.283266		2.283238		2.283147	2.283205	2.283150			2.283171	
r^o				2.166824				2.166833				
r^b				2.376191				2.376562				
r^a				2.339598				2.339563				
r^b				2.376598				2.376575				
r^a				2.339542				2.339568				
r^c				2.283208				2.283206				

[a]See Fig. 4.1 for definition. [b]See Figure 4.3 for an explanation of the labelling scheme.

Table A.2: Vibrationally averaged bond-lengths at 0K for the $^{35/37}Cl$ isotopologues and isotopomers of $[PtCl_5(H_2{}^{18}O)]^-$ calculated at the PBE0/SDD/6-31G* level [in Å].

Bond[a]	Isotopologue/Isotopomer[b]											
	A	B	C	D	E	F	G	H	I	J	K	L
r^o	2.166175	2.166241	2.166239	2.166208	2.166245	2.166291	2.166238	2.166260	2.166296	2.166257	2.166302	2.166312
r^b	2.376534	2.376467	2.376539	2.376409	2.376611	2.376518	2.376279	2.376496	2.376224	2.376413	2.376254	2.376417
r^a	2.339594	2.339584	2.339597	2.339625	2.339353	2.339565	2.339691	2.339595	2.339694	2.339524	2.339686	2.339525
r^b	2.376548	2.376564	2.376553	2.376422	2.376234	2.376535	2.376528	2.376494	2.376634	2.376426	2.376564	2.376430
r^a	2.339598	2.339582	2.339601	2.339630	2.339700	2.339567	2.339532	2.339575	2.339359	2.339527	2.339431	2.339528
r^c	2.283641	2.283569	2.283371	2.283614	2.283609	2.283356	2.283589	2.283359	2.283383	2.283595	2.283366	2.283365
r^o		2.166212		2.166210		2.166302	2.166256	2.166335			2.166304	
r^b		2.376695		2.376478		2.376649	2.376330	2.376264			2.376306	
r^a		2.339617		2.339634		2.339532	2.339576	2.339675			2.339525	
r^b		2.376138		2.376475		2.376195	2.376475	2.376566			2.376519	
r^a		2.339632		2.339613		2.339705	2.339622	2.33957			2.339639	
r^c		2.283663		2.283567		2.283375	2.283597	2.283355			2.283366	
r^o				2.166279				2.166249				
r^b				2.376305				2.376411				
r^a				2.339612				2.339631				
r^b				2.376555				2.376424				
r^a				2.339588				2.339635				
r^c				2.283583				2.283382				

[a]See Fig. 4.1 for definition. [b]See Figure 4.3 for an explanation of the labelling scheme.

Table A.3: Vibrationally averaged bond-lengths at 0K for the $^{35/37}$Cl isotopologues and isotopomers of *cis*-$PtCl_4(H_2{}^{16}O)_2$ calculated at the PBE0/SDD/6-31G* level [in Å].

Bond[a]	Isotopologue/Isotopomer[b]								
	A	B	C	D	E	F	G	H	I
r^{eq}	2.277928	2.277892	2.277879	2.277901	2.277927	2.277844	2.277882	2.277834	2.277829
r^{ax}	2.340558	2.340332	2.340389	2.340481	2.340695	2.340497	2.340672	2.340574	2.340413
r^{eq}	2.277925	2.277968	2.277910	2.277898	2.277857	2.277841	2.277871	2.277851	2.277825
r^{ax}	2.340558	2.340711	2.340673	2.340481	2.340266	2.340497	2.340268	2.340343	2.340413
r^{o}	2.142387	2.142340	2.142438	2.142478	2.142400	2.142416	2.142420	2.142411	2.142434
r^{o}	2.142374	2.142358	2.142399	2.142465	2.142466	2.142401	2.142401	2.142400	2.142420

Table A.4: Vibrationally averaged bond-lengths at 0K for the $^{35/37}$Cl isotopologues and isotopomers of *cis*-$PtCl_4(H_2{}^{18}O)_2$ calculated at the PBE0/SDD/6-31G* level [in Å].

Bond[a]	Isotopologue/Isotopomer[b]								
	A	B	C	D	E	F	G	H	I
r^{eq}	2.277850	2.277731	2.277765	2.277861	2.278007	2.277854	2.278015	2.277959	2.277870
r^{ax}	2.340599	2.340315	2.340490	2.340560	2.340923	2.340574	2.340755	2.340639	2.340507
r^{eq}	2.277849	2.277955	2.277939	2.277860	2.277770	2.277853	2.277721	2.277796	2.277870
r^{ax}	2.340599	2.340836	2.340666	2.340559	2.340266	2.340573	2.340345	2.340454	2.340506
r^{o}	2.141842	2.141909	2.141871	2.141837	2.141825	2.141870	2.141845	2.141733	2.141844
r^{o}	2.141840	2.141797	2.141828	2.141836	2.141852	2.141868	2.141845	2.141920	2.141842

[a]See Fig. 4.1 for definition. [b]See Figure 4.3 for an explanation of the labelling scheme.

Table A.5: Vibrationally averaged bond-lengths at 0K for the $^{35/37}$Cl isotopologues and isotopomers of *cis*-$PtCl_4(H_2{}^{18}O)$ ($H_2{}^{16}O$) calculated at the PBE0/SDD/6-31G* level [in Å].

Bond[a]	Isotopologue/Isotopomer[b]								
	A	B	C	D	E	F	G	H	I
r^{eq}	2.277846	2.277848	2.277776	2.277826	2.277879	2.277738	2.277837	2.277723	2.277784
r^{ax}	2.340479	2.340412	2.340319	2.340376	2.340841	2.340472	2.340439	2.340390	2.340385
r^{eq}	2.278027	2.278020	2.277907	2.278012	2.277694	2.277928	2.277769	2.277944	2.277895
r^{ax}	2.340687	2.340686	2.340789	2.340634	2.340219	2.340557	2.340522	2.340550	2.340529
r^{o}	2.142337	2.142343	2.142277	2.142359	2.142493	2.142388	2.142491	2.142363	2.142366
r^{o}	2.141693	2.141705	2.141820	2.141738	2.141835	2.141759	2.141829	2.141809	2.141796

Table A.6: Vibrationally averaged bond-lengths at 0K for the $^{35/37}$Cl isotopologues[b] and isotopomers of *fac*-$[PtCl_3(H_2{}^{16}O)_3]^+$ and *fac*-$[PtCl_3(H_2{}^{16}O)_2(H_2{}^{18}O)]^+$ calculated at the PBE0/SDD/6-31G* level [in Å].

Bond	*fac*-$[PtCl_3(H_2{}^{16}O)_3]^+$				*fac*-$[PtCl_3(H_2{}^{16}O)_2(H_2{}^{18}O)]^+$			
	A	B	C	D	A	B	C	D
Pt-Cl	2.268296	2.268085	2.268151	2.268104	2.268419	2.268238	2.268202	2.268252
Pt-Cl	2.268240	2.268284	2.268051	2.268116	2.268201	2.268006	2.267966	2.267988
Pt-Cl	2.268259	2.268233	2.268241	2.268156	2.268319	2.268254	2.268270	2.268154
Pt-O	2.146565	2.146522	2.146625	2.146619	2.145716	2.145751	2.145601	2.145649
Pt-O	2.146547	2.146543	2.146555	2.146494	2.146356	2.146468	2.146478	2.146421
Pt-O	2.146495	2.146643	2.146586	2.146667	2.146445	2.146530	2.146364	2.146450

[a]See Fig. 4.1 for definition. [b]See Figure 4.3 for an explanation of the labelling scheme.

Table A.7: Vibrationally averaged bond-lengths at 0K for the $^{35/37}$Cl isotopologues of *fac*-[$PtCl_3(H_2{}^{18}O)_2(H_2{}^{16}O)]^+$ calculated at the PBE0/SDD/6-31G* level [in Å].

Bond	Isotopologues[b]			
	A	B	C	D
Pt-Cl	2.268290	2.268194	2.268335	2.268299
Pt-Cl	2.268103	2.268191	2.268219	2.268141
Pt-Cl	2.268032	2.268037	2.268072	2.268029
Pt-O	2.145889	2.146042	2.146000	2.146115
Pt-O	2.145884	2.145802	2.145765	2.145765
Pt-O	2.146782	2.146786	2.146713	2.146735

Table A.8: Vibrationally averaged bond-lengths at 0K for the $^{35/37}$Cl isotopologues of *fac*-[$PtCl_3(H_2{}^{18}O)_3]^+$ calculated at the PBE0/SDD/6-31G* level [in Å].

Bond	Isotopologues[b]			
	A	B	C	D
Pt-Cl	2.268093	2.268030	2.268142	2.268165
Pt-Cl	2.268173	2.268192	2.268096	2.268100
Pt-Cl	2.268098	2.268190	2.268263	2.268056
Pt-O	2.146225	2.146152	2.146140	2.146114
Pt-O	2.146169	2.146064	2.146131	2.146092
Pt-O	2.146116	2.146283	2.146190	2.146248

[b]See Figure 4.3 for an explanation of the labelling scheme.

Table A.9: Vibrationally averaged bond-lengths at 0K for the $^{35/37}$Cl isotopologues and isotopomers of $[PtCl_5(^{16}OH)]^{2-}$ calculated at the PBE0/SDD/6-31G* level [in Å].

Bond[a]	Isotopologue/Isotopomer[b]										
	A	B	C	D	E	F	G	H	I	J	K
r_b	2.411986	2.412010	2.411975	2.412140	2.412035	2.412082	2.411997	2.411791	2.411944	2.412023	2.412024
r_a	2.385947	2.385877	2.385961	2.385880	2.385724	2.385846	2.385946	2.385983	2.385807	2.385880	2.385726
r_a''	2.374731	2.374705	2.374608	2.374506	2.374646	2.374743	2.374614	2.374749	2.374652	2.374618	2.374740
r_a'	2.361494	2.361475	2.361447	2.361377	2.361480	2.361449	2.361122	2.361500	2.361437	2.361361	2.361369
r_a	2.374732	2.374706	2.374764	2.374798	2.374645	2.374564	2.374661	2.374475	2.374653	2.374619	2.374742
r_c	2.010715	2.010714	2.010731	2.010719	2.010716	2.010731	2.010770	2.010749	2.010716	2.010711	2.010710
r_b			2.412140	2.412002	2.411969	2.412043	2.412060	2.412089	2.411790		2.411883
r_a			2.385885	2.385772	2.385921	2.385805	2.385760	2.385880	2.385752		2.385787
r_a''			2.374785	2.374864	2.374652	2.374750	2.374654	2.374860	2.374720		2.374590
r_a'			2.361307	2.361251	2.361448	2.361375	2.361336	2.361162	2.361468		2.361463
r_a			2.374785	2.374476	2.374653	2.374750	2.374655	2.374527	2.374720		2.374591
r_c			2.010698	2.010766	2.010710	2.010710	2.010710	2.010724	2.010717		2.010722
r_b			2.412194			2.411817	2.412006				2.411819
r_a			2.385721			2.385896	2.385842				2.386003
r_a''			2.374709			2.374687	2.374602				2.374666
r_a'			2.361443			2.361552	2.361360				2.361131
r_a			2.374710			2.374688	2.374603				2.374526
r_c			2.010711			2.010724	2.010715				2.010740

[a]See Fig. 5.1 for definition. [b]See Figure 5.3 for an explanation of the labelling scheme.

Table A.10: Vibrationally averaged bond-lengths at 0K for the $^{35/37}$Cl isotopologues and isotopomers of $[PtCl_5(^{18}OH)]^{2-}$ calculated at the PBE0/SDD/6-31G* level [in Å].

Bond[a]	Isotopologue/Isotopomer[b]										
	A	B	C	D	E	F	G	H	I	J	K
r_b	2.412017	2.411975	2.411938	2.412048	2.412096	2.412083	2.412113	2.411824	2.411956	2.411929	2.412031
r_a	2.385870	2.385808	2.385897	2.385839	2.385781	2.385787	2.385892	2.385885	2.385778	2.385858	2.385704
r_a''	2.374710	2.374673	2.374605	2.374452	2.374692	2.374725	2.374450	2.374916	2.374599	2.374629	2.374684
r_a'	2.361490	2.361508	2.361439	2.361402	2.361419	2.361450	2.361262	2.361444	2.361436	2.361397	2.361369
r_a	2.374711	2.374674	2.374778	2.374775	2.374696	2.374511	2.374857	2.374433	2.374600	2.374630	2.374685
r_c	2.010504	2.010509	2.010523	2.010516	2.010502	2.010523	2.010532	2.010536	2.010506	2.010506	2.010500
r_b			2.412189	2.412135	2.411989	2.412100	2.412157	2.412084	2.411918		2.411891
r_a			2.385908	2.385900	2.385922	2.385875	2.385806	2.385844	2.385689		2.385672
r_a''			2.374833	2.374959	2.374590	2.374793	2.374681	2.374910	2.374682		2.374514
r_a'			2.361240	2.361143	2.361452	2.361309	2.361290	2.361079	2.361464		2.361485
r_a			2.374835	2.374526	2.374592	2.374790	2.374682	2.374399	2.374678		2.374515
r_c			2.010494	2.010534	2.010499	2.010497	2.010495	2.010544	2.010503		2.010517
r_b			2.412110			2.411856	2.411883				2.411877
r_a			2.385827			2.385812	2.385806				2.385791
r_a''			2.374607			2.374698	2.374592				2.374864
r_a'			2.361498			2.361530	2.361374				2.361261
r_a			2.374608			2.374700	2.374593				2.374317
r_c			2.010507			2.010509	2.010511				2.010552

[a]See Fig. 5.1 for definition. [b]See Figure 5.3 for an explanation of the labelling scheme.

Table A.11: Vibrationally averaged bond-lengths at 0K for the $^{35/37}$Cl isotopologues and isotopomers of *cis*-$[PtCl_4(^{16}OH)_2]^{2-}$ calculated at the PBE0/SDD/6-31G* level [in Å].

Bond[a]	Isotopologue/Isotopomer[b]								
	A	B	C	D	E	F	G	H	I
r_b	2.400599	2.400466	2.400210	2.400539	2.400343	2.400269	2.400386	2.400416	2.400446
r_a	2.388685	2.388435	2.388971	2.388622	2.388709	2.388678	2.388731	2.388574	2.388438
r_a’	2.362721	2.362781	2.362793	2.362668	2.362824	2.362685	2.362655	2.362751	2.36264
r_b’’	2.425963	2.425818	2.426039	2.425796	2.426035	2.426007	2.426055	2.425923	2.425718
r_c	2.014962	2.014979	2.015014	2.014978	2.015031	2.015009	2.015028	2.014954	2.014977
r_c’’	2.001176	2.001220	2.001162	2.001229	2.001183	2.001155	2.001177	2.001163	2.001197
r_b		2.400582	2.400502		2.400373		2.400535	2.400376	
r_a		2.388419	2.388427		2.388366		2.388569	2.38858	
r_a’		2.362625	2.362863		2.362928		2.36263	2.362643	
r_b’’		2.425731	2.425862		2.425678		2.425753	2.42591	
r_c		2.015033	2.015006		2.014964		2.01499	2.015019	
r_c’’		2.001210	2.001218		2.001231		2.001244	2.001178	
r_b					2.400307				
r_a					2.388886				
r_a’					2.362592				
r_b’’					2.426002				
r_c					2.015035				
r_c’’					2.001185				
r_b					2.400573				
r_a					2.388399				
r_a’					2.362677				
r_b’’					2.425885				
r_c					2.015032				
r_c’’					2.001243				

[a]See Fig. 5.1 for definition. [b]See Figure 5.5 for an explanation of the labelling scheme.

Table A.12: Vibrationally averaged bond-lengths at 0K for the $^{35/37}$Cl isotopologues and isotopomers of *cis*-$[PtCl_4(^{18}OH)_2]^{2-}$ calculated at the PBE0/SDD/6-31G* level [in Å].

Bond[a]	Isotopologue/Isotopomer[b]								
	A	B	C	D	E	F	G	H	I
r_b	2.400484	2.400286	2.400306	2.400441	2.400346	2.400244	2.400358	2.400198	2.400288
r_a	2.388439	2.388572	2.388529	2.388529	2.388683	2.388685	2.388801	2.388134	2.388332
r_a’	2.362762	2.362859	2.362802	2.362715	2.362560	2.362638	2.362548	2.362667	2.362521
r_b’’	2.425982	2.425675	2.425869	2.425753	2.425634	2.425704	2.425656	2.425952	2.425725
r_c	2.014749	2.014750	2.014785	2.014740	2.014760	2.014791	2.014748	2.014757	2.014738
r_c’’	2.000945	2.000989	2.000922	2.001037	2.000943	2.000895	2.000972	2.000963	2.000994
r_b		2.400451	2.400193		2.400175		2.400490	2.400177	
r_a		2.388552	2.388674		2.388296		2.388521	2.388754	
r_a’		2.362673	2.362826		2.362606		2.362697	2.362668	
r_b’’		2.425708	2.425752		2.425890		2.425686	2.425804	
r_c		2.014790	2.014812		2.014759		2.014781	2.014781	
r_c’’		2.001024	2.000956		2.001000		2.001024	2.000916	
r_b					2.400346				
r_a					2.388698				
r_a’					2.362639				
r_b’’					2.425857				
r_c					2.014795				
r_c’’					2.000942				
r_b					2.400550				
r_a					2.388702				
r_a’					2.362600				
r_b’’					2.425715				
r_c					2.014793				
r_c’’					2.000996				

[a]See Fig. 5.1 for definition. [b]See Figure 5.5 for an explanation of the labelling scheme.

Table A.13: Vibrationally averaged bond-lengths at 0K for the $^{35/37}$Cl isotopologues[b] and isotopomers of *fac*-$[PtCl_3(^{16}OH)_3]^{2-}$ and *fac*-$[PtCl_3(^{18}OH)_3]^{2-}$ calculated at the PBE0/SDD/6-31G* level [in Å].

Bond	*fac*-$[PtCl_3(^{16}OH)_3]^{2-}$				*fac*-$[PtCl_3(^{18}OH)_3]^{2-}$			
	A	B	C	D	A	B	C	D
r_a	1.998288	1.998218	1.998248	1.998252	1.998095	1.998000	1.998064	1.998090
r_a	1.998334	1.998342	1.998306	1.998279	1.998138	1.998213	1.998091	1.998124
r_a	1.998298	1.998253	1.998254	1.998264	1.998095	1.998128	1.998107	1.998096
r_b	2.439167	2.438820	2.439116	2.438824	2.439048	2.438923	2.439102	2.439009
r_b	2.438995	2.438812	2.438816	2.438958	2.438977	2.438862	2.438835	2.438960
r_b	2.439111	2.439322	2.438935	2.438988	2.439115	2.439206	2.438824	2.439062

Table A.14: Vibrationally averaged bond-lengths at 0K for the $^{35/37}$Cl isotopologues[b] and isotopomers of *cis*-$[PtCl_2(^{16}OH)_4]^{2-}$ and *cis*-$[PtCl_2(^{18}OH)_4]^{2-}$ calculated at the PBE0/SDD/6-31G* level [in Å].

Bond	*cis*-$[PtCl_2(^{16}OH)_4]^{2-}$			*cis*-$[PtCl_2(^{18}OH)_4]^{2-}$			
	A	B	C	A	B		C
r_a	2.436095	2.436111	2.436083	2.435707	2.436248	2.436390	2.436433	2.436123
r_b	1.996557	1.996537	1.996556	1.996558	1.996406	1.996378	1.996311	1.996423
r_c'	2.041830	2.041791	2.041758	2.041784	2.041417	2.041432	2.041531	2.041350
r_a'	2.420441	2.420191	2.420228	2.420105	2.420700	2.420665	2.420303	2.420744
r_c	2.035254	2.035187	2.035292	2.035197	2.035186	2.035161	2.035133	2.035197
r_b'	2.007651	2.007682	2.007604	2.007618	2.007415	2.007429	2.007409	2.007332

[a]See Fig. 5.1 for definition. [b]See Figure 5.6 and 5.7 for an explanation of the labelling scheme.

Table A.15: Vibrationally averaged bond-lengths at 0K for the $^{35/37}$Cl isotopologues[b] and isotopomers of $[PtCl(^{16}OH)_5]^{2-}$ and $[PtCl(^{18}OH)_5]^{2-}$ calculated at the PBE0/SDD/6-31G* level [in Å].

Bond[a]	$[PtCl(^{16}OH)_5]^{2-}$		$[PtCl(^{18}OH)_5]^{2-}$	
	A	B	A	B
r_b	2.029761	2.029797	2.029632	2.029698
r_b''	2.037566	2.037572	2.037064	2.037087
r_b'''	2.043522	2.043530	2.043076	2.043022
r_a	2.449742	2.449560	2.449668	2.448956
r_b'	2.050264	2.050173	2.049949	2.049878
r_c	1.996362	1.996416	1.996104	1.996138

[a]See Fig. 5.1 for definition. [b]See Figure 5.8 for an explanation of the labelling scheme.

Table A.16: Vibrationally averaged bond-lengths at 0K for the $^{35/37}$Cl isotopologues and isotopomers of $[RhCl_5(H_2{}^{16}O)]^{2-}$ calculated at the PBE0/SDD/6-31G* level [in Å].

Bond[a]	Isotopologue/Isotopomer[b]									
	A	B	C	D	E	F	G	H	I	J
r^o	2.36312	2.363112	2.36309	2.363244	2.362908	2.363049	2.362948	2.363083	2.362821	2.363072
r^b	2.36312	2.36317	2.36309	2.363243	2.36314	2.363194	2.363066	2.363083	2.363147	2.363072
r^a	2.442946	2.442745	2.442999	2.442612	2.442475	2.442778	2.443448	2.442502	2.44254	2.442778
r^b	2.321739	2.321713	2.32137	2.321764	2.321753	2.321418	2.321759	2.32142	2.321422	2.321757
r^a	2.442946	2.442969	2.442999	2.442612	2.44326	2.442377	2.442218	2.442502	2.443248	2.442778
r^c	2.205287	2.205338	2.205477	2.205267	2.205403	2.205311	2.205355	2.20513	2.205288	2.205343
r^o		2.363218		2.363118		2.363123	2.363112	2.363012		
r^b		2.363048		2.363118		2.36305	2.363251	2.363289		
r^a		2.44241		2.442523		2.442138	2.442748	2.44329		
r^b		2.321773		2.321805		2.321476	2.321778	2.321413		
r^a		2.443306		2.442523		2.443391	2.442783	2.442055		
r^c		2.205251		2.205231		2.20532	2.205283	2.20521		
r^o				2.363237				2.363124		
r^b				2.363068				2.363123		
r^a				2.442195				2.442781		
r^b				2.321763				2.321486		
r^a				2.443238				2.442781		
r^c				2.205276				2.205274		

[a]See Fig. 6.1 for definition. [b]See Figure 4.3 for an explanation of the labelling scheme.

Table A.17: Vibrationally averaged bond-lengths at 0K for the $^{35/37}$Cl isotopologues and isotopomers of *cis*-$[RhCl_4(H_2{}^{16}O)_2]^-$ calculated at the PBE0/SDD/6-31G* level [in Å].

Bond[a]	Isotopologue/Isotopomer[b]								
	A	B	C	D	E	F	G	H	I
r^{eq}	2.316639	2.316655	2.316373	2.316616	2.316303	2.316596	2.316378	2.316576	2.316613
r^{ax}	2.368404	2.36839	2.368403	2.36843	2.368709	2.368467	2.368402	2.368451	2.368424
r^{eq}	2.368443	2.368323	2.3685	2.368467	2.368123	2.36851	2.368469	2.368396	2.368463
r^{ax}	2.316689	2.31668	2.316866	2.316666	2.316894	2.316644	2.316831	2.316653	2.316662
r^{o}	2.153552	2.153564	2.15351	2.153613	2.153558	2.153563	2.153511	2.153551	2.153578
r^{o}	2.15342	2.153437	2.153526	2.153483	2.153458	2.153425	2.153493	2.153446	2.153442

Table A.18: Vibrationally averaged bond-lengths at 0K for the $^{35/37}$Cl isotopologues and isotopomers of *fac*-$[RhCl_3(H_2{}^{16}O)_3]^{2-}$ calculated at the PBE0/SDD/6-31G* level [in Å].

Bond	Isotopologue[b]			
	A	B	C	D
Pt-Cl	2.137732	2.137644	2.137700	2.137692
Pt-Cl	2.137631	2.137680	2.137724	2.137658
Pt-Cl	2.137634	2.137680	2.137700	2.137657
Pt-O	2.301039	2.301108	2.301015	2.300837
Pt-O	2.301191	2.301138	2.301023	2.301149
Pt-O	2.301191	2.301138	2.301158	2.301149

[a]See Fig. 6.1 for definition. [b]See Figure 4.3 for an explanation of the labelling scheme.

The Cartesian coordinates used to generate the data in Tables A.1 - A.18 are collected in an Appendix B supplied to the electronic version of this thesis.